TBMCE 2020

3rd International Conference on

TECHNOLOGIES & BUSINESS MODELS FOR CIRCULAR ECONOMY

CONFERENCE PROCEEDINGS

EDITORS
SANJA POTRČ
MILOŠ BOGATAJ
ZDRAVKO KRAVANJA
ZORKA NOVAK PINTARIČ

University of Maribor Press

Faculty of Chemistry and
Chemical Engineering

3rd International Conference on Technologies & Business Models for Circular Economy

Conference Proceedings

Editors
Sanja Potrč
Miloš Bogataj
Zdravko Kravanja
Zorka Novak Pintarič

May 2022

Title
Naslov
3rd International Conference on Technologies & Business Models for Circular Economy

Subtitle
Podnaslov
Conference Proceedings

Editors
Uredniki
Sanja Potrč
(University of Maribor, Faculty of Chemistry and Chemical Engineering)

Miloš Bogataj
(University of Maribor, Faculty of Chemistry and Chemical Engineering)

Zdravko Kravanja
(University of Maribor, Faculty of Chemistry and Chemical Engineering)

Zorka Novak Pintarič
(University of Maribor, Faculty of Chemistry and Chemical Engineering)

Technical editor
Tehnični urednik
Jan Perša
(University of Maribor, University Press)

Cover designer
Oblikovanje ovitka
Jan Perša
(University of Maribor, University Press)

Graphic material
Grafične priloge
Authors of proceedings & editors

Conference
Konferenca
TBMCE, International Conference on Technologies & Business Models for Circular Economy

Date and location
Datum in kraj
December 15th, 2020, on-line, Slovenia

United States of America), Timothy G. Walmsley, (Waikato University, New Zeeland), Tomaž Katrašnik (University of Ljubljana, Slovenia), Blaž Likozar (National Institute of Chemistry, Slovenia), Primož Oven (University of Ljubljana, Slovenia), Dragica Marinič (Chamber of Commerce and Industry of Štajerska, Slovenia) & Vilma Ducman (Slovenian national building and civil engineering institute, Slovenia).

Published by / *Založnik*
University of Maribor
University Press
Slomškov trg 15, 2000 Maribor, Slovenija
https://press.um.si, zalozba@um.si

Issued by / *Izdajatelj*
University of Maribor
Faculty of Chemistry and Chemical Engineering
Smetanova ulica 17, 2000 Maribor, Slovenija
https://www.fkkt.um.si/, fkkt@um.si

Publication type / *Vrsta publikacije*
E-book

Edition / *Izdaja*
1st

Available at / *Dostopno na*
http://press.um.si/index.php/ump/catalog/book/677

Published at / *Izdano*
Maribor, May 2022

This investment is co-financed by the Republic of Slovenia and the European Union Fund for Regional Development"

CIP - Kataložni zapis o publikaciji
Univerzitetna knjižnica Maribor

330:502.131.1(082)(0.034.2)

INTERNATIONAL Conference on Technologies & Business Models for Circular Economy (3 ; 2021 ; Portorož)
3rd International Conference on Technologies & Business Models for Circular Economy, [September 13th to September 15th 2021, Portorož, Slovenia] [Elektronski vir] : conference proceedings / [editors Sanja Potrč ... [et al.]. - E-zbornik. - Maribor : University of Maribor, University Press, 2022

Način dostopa (URL): https://press.um.si/index.php/ump/catalog/book/677
ISBN 978-961-286-598-6 (pdf)
doi: 10.18690/um.fkkt.2.2022
COBISS.SI-ID 109396739

ISBN 978-961-286-598-6 (pdf)

DOI https://doi.org/10.18690/um.fkkt.2.2022

Price
Cena Free copie

For publisher
Odgovorna oseba založnika prof. dr. Zdravko Kačič,
Rector of University of Maribor

Attribution
Citiranje Potrč, S., Bogataj, M., Kravanja, Z., Novak Pintarič, Z., (eds.). (2022). 3rd *International Conference on Technologies & Business Models for Circular Economy* Maribor: University Press. doi: 10.18690/um.fkkt.2.2022

Table of Contents

THE DEVELOPMENT AND ASSESSMENT OF ALKALI ACTIVATED PAVING BLOCKS

ANA FRANKOVIČ,[1] VILMA DUCMAN,[1]
LUBICA KRISKOVA,[2] EFTHYMIOS TATSIS,[2]
PETRICA PETRICA,[2] YIANNIS PONTIKES[2]

[1] Slovenian National Building and Civil Engineering Institute, Ljubljana, Slovenia
ana.frankovic@zag.si, vilma.ducman@zag.si
[2] KU Leuven, Department of Materials Engineering, Leuven, Belgium
lubica.kriskova@kuleuven.be, efthymios.tatsis@kuleuven.be, petricapetrica1@gmail.com
yiannis.pontikes@kuleuven.be

Abstract In recent years great attention has been placed by the building sector on alkali-activated technology based on metakaolin, fly ash and ground granulated blast furnace slag (GGBFS), but also on emerging precursors such as by-products from non-ferrous metallurgy. The present work focuses on the development of alkali-activated binders from two slags, one from primary and one from secondary copper production, which were finely milled, blended with GGBFS, and activated with K-based alkali silicate solution with a 1.7 SiO2/K2O molar ratio. The aggregate to paste mass ratio was 2. The mixtures were cast, and cured for a designated time at room temperature and 60% RH. The so-obtained paving blocks were then tested in accordance with European standard for concrete paving blocks. The following properties were measured: splitting tensile strength, abrasion resistance, slip and skid resistance, resistance to freeze-thaw and resistance to freeze-thaw in the presence of de-icing salts. Their properties were compared to those of commercially available concrete paving blocks, and it was found that the performance of the alkali-activated pavers was generally comparable with the concrete pavers, while certain properties (e.g., abrasion resistance, freeze-thaw resistance and freeze-thaw resistance in presence of de-icing salts) were considerably better.

Keywords:
Cu slag,
alkali activation process,
pavers,
properties,
durability

University of Maribor Press

DOI https://doi.org/10.18690/um.fkkt.2.2022.1
ISBN 978-961-286-598-6

1 Introduction

One of the main objectives of the circular economy is to reduce the overuse of the available raw materials in order to restore ecological balance. This can be achieved by replacing raw materials with industrial waste or by-products. The greatest potential is seen in construction sector which consumes 35-45 % of natural resources [1].

Alkali-activation technology has been recognized as a promising method for the utilization of wastes and industrial by-products which are rich in silica and aluminium. The type of waste and by-products mentioned can therefore be used as a precursor in alkali-activated technology and converted into valuable building and construction materials such as binders, concrete, mortar, paving blocks, and bricks, thereby reducing demand for, and the subsequent environmental impact of, the production of Ordinary Portland Cement (OPC) [2]. In order to produce high quality building products, the composition of the alkali-activated mixture must be properly adjusted. Van De Sande et al. show that the chemical and mineralogical composition of non-ferrous slags used as precursors for alkali-activation play an important role in the mechanical and physical properties of the final product, and that the type of activator affects the kinetics and strength at an early age of the final product [3]. Furthermore, it was shown that using a proper rate of cooling when solidifying the non-ferrous slags led to the formation of a higher content of amorphous phase, and consequently to the formation of a solid alkali-activated binder [4].

One promising final uses for alkali-activated binders with a high residue content is the production of paving blocks. When processing new products, the aim is to develop products which have better, or at least comparable properties, to products already established on the market. The literature shows some cases where alternative materials, such as paving blocks, have been successfully made using alkali-activated technology. For example, Tatarannni et. al. successfully used waste basalt powder as a precursor in an alkali-activated binder for the production of alternative paving blocks [5]. Furthermore, Hossiney et. al. synthesized alkali-activated paving blocks using a high residues content in both the precursor (fly ash and ground granulated blast furnace slags) and the aggregate (recycled asphalt pavements) [6].

This paper presents an alternative alkali-activated binder developed from non-ferrous metallurgy slag, used in up-scale production of paving blocks, intended for implementation in sustainable urban areas. Since there are no standards available for newly developed alkali-activated products, the performance of the paving blocks developed was evaluated according to standard EN 1338: Concrete paving blocks - Requirements and test methods [7].

2 Experimental

2.1 Materials

Finely milled (approximately 4000 cm^2/g Blaine surface area) iron rich mineral formed during/ after secondary Cu production, i.e. Koranel® (Metallo Belgium N.V), was used in the present study. Its chemical composition is given in Table 1; its mineralogical evaluation confirmed the highly amorphous nature of the precursor, which contains 92 % amorphous phase and 8 % of the mineral Hercynite.

Table 1: Chemical composition of the materials, in wt%

Oxide	FeO	SiO_2	Al_2O_3	CaO	ZnO	MgO	SO_3	Na_2O	CuO	Others
Koranel®	51	25	8	3	6	1	<1	<1	<1	3

2.2 Production

The paving tiles were produced by blending Koranel® with GGBFS in a 6:1 mass:ratio and activated with a K- based alkali silicate solution (SiO_2/K_2O molar ratio of 1.7 and water content of 65 wt%), bringing the solution to a powder mass ratio of ~ 0.4. The aggregates and additives were gradually added into the activating solution and the final blend was mixed at high speed for approximately 2 min in a Hobart mixer. The fresh mortars were cast into moulds and cured for a designated time at RT and 60% RH.

Figure 1: The production process of the alkali activated paving blocks
Source: authors from KU Leuven

2.3 Methods

The paving blocks developed were tested with respect to their intended use, following the specifications outlined in standard EN 1338: Concrete paving blocks - Requirements and test methods [7]. The testing method for freeze-thaw resistance was adopted according to the standard ASTM C666 / C666M – 15: Standard Test Method for Resistance of Concrete to Rapid Freezing and Thawing [8].

The following parameters were simultaneously determined for both the Koranel®-rich paving blocks developed and for the reference material, a commercial product widely used in urban paving:

- slip and skid resistance,
- abrasion resistance,
- splitting tensile strength,
- freeze-thaw resistance,
- freeze-thaw resistance in the presence of de-icing salts.

Since the number of samples was limited, some adjustments were made when performing the splitting tensile strength test. As shown in Figure 2, the samples were oriented differently so that two halves could be obtained in order to implement further test methods.

Figure 2: Adjustment in the performance of the splitting tensile strength test.
Source: own.

3 Results and discussion

The test results are shown in Table 2. As can be seen from the results, the slip and skid resistance coefficient (Pendulum Test Value – PTV) is highly dependent on the nature of the surface; it is generally higher on the upper side, while it is very smooth with much lower values on the bottom side, where it had been in contact with the mould. On Rubber 57 under wet conditions, the PTV of the Koranel®-rich samples was 29 at the side which had been in contact with the mould, and 56 at the upper face within the mould. The reference material attained a value of 69. It should be noted that this characteristic could be significantly influenced simply by making a relief of the surface of the mould during the production phase.

When determining abrasion resistance, the length of the groove of the Koranel®-rich paving blocks was 17.6 mm, compared to 22.1 mm in the reference material (Figure 3). According to the standard, permissible values for the abrasion resistance of concrete paving blocks have not been specified. From the literature, however, it

can be seen that natural stone reaches values from 14.8 mm for granite to as high as 27.3 in limestone [9].

Table 2: The performance of alkali activated paving blocks compared to the commercial concrete paving blocks

Parameter	Unite/conditions	Koranel®-rich	Reference material
Slip and skid resistance (PTV) (Top/bottom)	Rubber 57 – Wet	29/56	69
Abrasion resistance	mm	17.6	22.1
Splitting tensile strength	MPa	9.5	4.0
Freeze-thaw resistance	After 300 cycles (-20°C/9°C)	Resistant	Not resistant
Freeze-thaw resistance in presence of de-icing salts	After 25 cycles (3% NaCl; -20°C/20°C)	Resistant	Not resistant

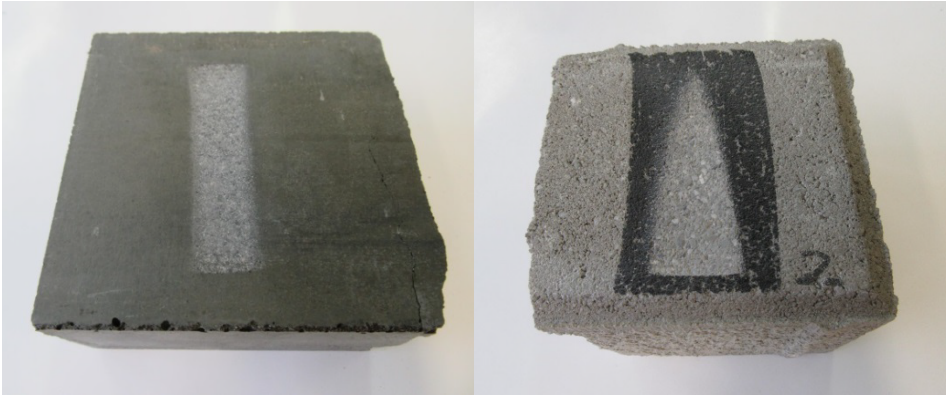

Figure 3: Abrasion resistance of the Koranel® sample (left) and the reference material sample (right)

Source: own.

As mentioned above, the splitting tensile strength test method was modified. The results obtained showed that the Koranel®-rich paving blocks exhibited a splitting tensile strength of 9.5 MPa, which is higher than that of the reference material, which reached 4 MPa.

Furthermore, freeze-thaw resistance was monitored by measuring the resonant frequency, as shown in Figure 4. The results show that breakage of the internal structure begins in the reference material after about 80 freeze-thaw cycles. After 300 freeze-thaw cycles there was visible deterioration in the reference material, while the Koranel®-rich paving blocks remained unchanged (Figure 5).

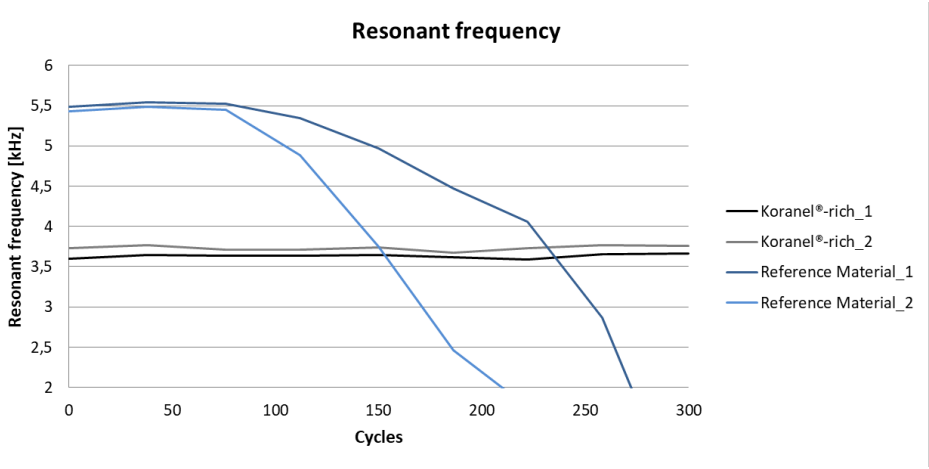

Figure 4: Resonant frequency after 300 freeze-thaw cycles

Source: own.

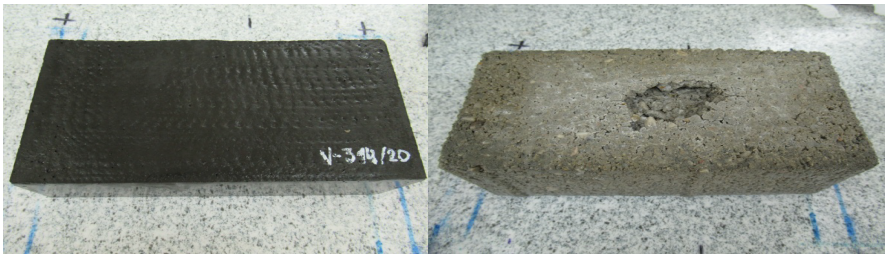

Figure 5: Freeze-thaw resistance after 300 cycles; Koranel®-rich sample (left) and the reference material (right)

Source: own.

A similar trend was seen when determining the freeze-thaw resistance of the materials in the presence of de-icing salt. The Koranel®-rich paving blocks showed no deterioration after 25 freeze-thaw cycles (freezing at – 20 °C and thawing at 20 °C), while cracks appeared on the surface of the reference material after 20 cycles (Figure 6).

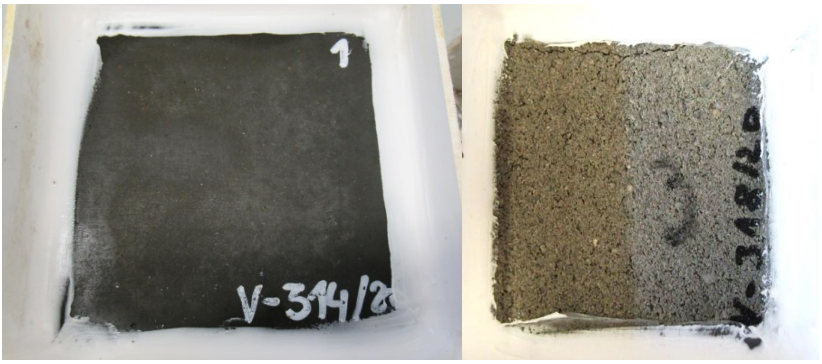

Figure 6: Results of freeze-thaw resistance tests in the presence of de-icing salts; Koranel®-rich sample after 28 freeze-thaw cycles (left), and the reference material after 20 cycles (right)
Source: own.

4 Conclusions

Slags generated from the production of various metals were successfully utilized for the production of paving blocks. The performance of blocks obtained in such a way was compared to commercially available concrete paving blocks, and it was confirmed that the performance of the alkali-activated pavers was on a par with the concrete pavers, with certain properties being notably better:

- Koranel®-rich samples were resistant to over 300 freeze-thaw cycles,
- Koranel®-rich samples also exhibited resistance to freezing and thawing in the presence of de-icing salts,
- the splitting tensile strength of the alkali-activated samples was twice as high as that of the concrete paving blocks,
- abrasion resistance was highest in the Koranel®-rich based paving blocks.

The technology developed could therefore be successfully implemented in the building sector, providing both the benefit of using waste instead of virgin materials, thus saving resources, and lowering the potential of global warming by replacing cement with alternative binders. Such a solution is completely in alignment with our present-day paradigm of promoting industrial symbiosis and a circular economy.

Acknowledgement

"This activity has received funding from EIT RawMaterials, a Knowledge and Innovation Community (KIC) of the European Institute of Innovation and Technology (EIT), a body of the European Union, under Horizon 2020, the EU Framework Programme for Research and Innovation. Project Agreement No. 16365 (RECOVER), project website: https://recover.technology."

References

[1] P. Mhatre, V. Gedam, S. Unnikrishnan, S. Verma, Circular Economy in Built Environment – Literature Review and Theory Development, Journal of Building Engineering, https://doi.org/10.1016/j.jobe.2020.101995.

[2] Singh, J., & Singh, S. P. (2019). Geopolymerization of solid waste of non-ferrous metallurgy – A review. Journal of Environmental Management, 251, 109571. doi:10.1016/j.jenvman.2019.109571

[3] Van De Sande, J., Peys, A., Hertel, T., Rahier, H., & Pontikes, Y. (2020). Upcycling of non-ferrous metallurgy slags: Identifying the most reactive slag for inorganic polymer construction materials. Resources, Conservation and Recycling, 154, 104627. doi:10.1016/j.resconrec.2019.104627

[4] Pontikes, Y., Machiels, L., Onisei, S., Pandelaers, L., Geysen, D., Jones, P. T., & Blanpain, B. (2013). Slags with a high Al and Fe content as precursors for inorganic polymers. Applied Clay Science, 73, 93–102. doi:10.1016/j.clay.2012.09.020

[5] Tataranni. (2019). Recycled Waste Powders for Alkali-Activated Paving Blocks for Urban Pavements: A Full Laboratory Characterization. Infrastructures, 4(4), 73. doi:10.3390/infrastructures4040073

[6] Hossiney, N., Sepuri, H. K., Krishna Mohan, M., R, A. H., Govindaraju, S., & Chyne, J. (2019). Alkali-activated concrete paver blocks made with recycled asphalt pavement (RAP) aggregates. Case Studies in Construction Materials, e00322. doi:10.1016/j.cscm.2019.e00322

[7] EN 1338: Concrete paving blocks - Requirements and test methods.

[8] ASTM C666 / C666M – 15: Standard Test Method for Resistance of Concrete to Rapid Freezing and Thawing.

[9] Karaca, Z., Günes Yılmaz, N. & Goktan, R.M. (2012). Considerations on the European Standard EN 14157 Test Methods: Abrasion Resistance of Natural Stones Used for Flooring in Buildings. Rock Mech Rock Eng 45, 103–111. https://doi.org/10.1007/s00603-011-0190-1

Influence of Homogenization of Alkali-Activated Slurry on Mechanical Strength

Barbara Horvat, Mark Češnovar, Katja Traven, Majda Pavlin, Katja König, Vilma Ducman

Slovenian National Building and Civil Engineering Institute, Ljubljana, Slovenia
barbara.horvat@zag.si, mark.cesnovar@zag.si, katja.traven@zag.si, majda.pavlin@zag.si, ketsi.koenig@gmail.com, vilma.ducman@zag.si

Abstract Alkali-activated materials are promising materials for the construction industry due to the accessibility of the precursors, which are mainly secondary industrial by-products, and their cost-effective and energy-efficient production. Although these materials are not new, some of the parameters in the technological process are not yet fully understood and tested. Therefore, in this paper in the means of mechanical strength, the preparation of alkali-activated pastes by using a three-roll mill homogenization method is discussed. The influence of homogenization of alkali-activated slurry has been evaluated on different waste materials (fly ash, fly ash with metakaolin, slag mixture (electric arc furnace slag and ladle slag), glass wool, waste green ceramics), which are treated with different alkali activators (NaOH, commercial sodium silicate solution, laboratory-produced alkali activators based on waste cathode- ray tube glass) with different curing regimes (60 °C and 70 °C) and different drying methods (drying at room temperature, drying at 105 °C). The viscosity of the slurry before homogenization was higher than after homogenization, the distribution of elements was more uniform and the compressive strength higher in all homogenized alkali activated materials, regardless of other parameters.

Keywords:
secondary raw material, alkali activated material, foaming, homogenization, mechanical strength

University of Maribor Press

DOI https://doi.org/10.18690/um.fkkt.2.2022.2
ISBN 978-961-286-598-6

1 Introduction

Alkali activation is a chemically driven process in which aluminosilicate-rich precursors react with alkali media to form a solid binder, making these materials one of the promising alternatives to ordinary Portland cement (Juenger et al., 2011). As aluminosilicates are one of the most common minerals in the earth's crust (Schlesinger, 1991), they are contained in clays, in industrial by-products such as biomass and coal fly ashes, metallurgical slags, red mud and mineral wool waste, which offers the possibility to produce sustainable non-structural materials. The alkali-activated materials produced from these precursors have high mechanical strength, high thermal and chemical resistance and are refractory (Bernal and Provis, 2014). One of the possibilities, due to their thermal stability, are prefabricated lightweight insulation boards (foams). The chemical reaction of the so-called alkali activation begins with the dissolution of the aluminosilicates and ends with solidification. Nowadays, it is more often used in the laboratory than on the construction site, because the process is not well understood and the technology is not set up in the same way as for ordinary cement concrete mixtures. Nevertheless, some projects, such as E-crete™, have already shown some of the advantages of using alkali activated materials based on fly ash and slag for pavements: along the freeway in Port Melbourne, precast slabs for VicRoads, which have a much higher strength (55 MPa) than required by governmental legislation (Van Deventer et al., 2012). Therefore, low carbon awareness, a source of precursors and activators with developed technology, and the durable end product for larger-scale production are crucial for production on a larger scale.

Numerous articles are published each year, where alkali activation focuses on the phase composition associated with the type of Ca-containing precursor and a sufficient amount of reactive amorphous Al and Si, computer modelling of the Al:Si ratio, the type and amount of activator, knowing that this is the most important factor in producing a material with the desired microstructure and mechanical properties (Vlček et al., 2014). Although some authors also study in detail the precursor preparations (drying, grinding and sieving) (Traven et al., 2019) and curing regimes (Češnovar et al., 2019) there is no real research in the technology of mixing and homogenizing with alkali activation. Size distribution, shape and packing of the precursor particles during mixing play an important role in the rheology of the alkali-activated slurry (Hunger and Brouwers, 2009). The surface tension of the particle-

fluid interface and the ionic strength of the solution (Provis et al., 2010) is also related to the processability of the slurry. One of the possibilities to solve this problem is the use of chemical admixtures or so-called superplasticisers as used for Portland cement pastes but the results are not yet promising (Criado et al., 2009).

Another possibility to achieve better processability of alkali activated slurries is the correct homogenization. This technique offers the possibility of wetting solid particles while the liquid to dry content is not changed, which is important when the activator to precursor ratio is fixed at a calculated value. In most cases, homogenization is done after addition of an activator to the precursor (or vice versa), by manual mixing for 1 to 5 min by hand (with palate knife) (Rajamma et al., 2012), or mechanically with a laboratory mixer (Korat and Ducman, 2017), with an ordinary mixer for cement pastes such as Automix (Samson et al., 2017), Hobart mixer (Nematollahi et al., 2017) or a combination of mixing by hand and with a mixer (Hajimohammadi et al., 2017). However, when homogenization technology is used, there is still no known relationship with the final mechanical properties of alkali-activated materials. When producing alkali-activated materials on a large scale, preparation of mixtures by manual mixing is impossible due to the longer time required for this process, and manual mixing itself does not provide good and efficient homogenization. This paper tries to clarify how different precursors behave when slurries are mixed manually and/or with laboratory mixers and when a three-roll homogenizer homogenizes them. The homogenization of alkali activated foams based on electric arc furnace slag and fly ash, which are foamed with Na-perborate or H_2O_2, is also investigated. In the production of alkali-activated foams, surface agents such as triton, sodium oleate, sodium dodecyl sulfate or others are added to the slurry to stabilize air voids which are formed by a chemical reaction from the foaming agent (Korat and Ducman, 2017). While foaming and surface agents appear in a solid or liquid state, this also affects the viscosity and workability of the slurry. For foams produced by manual or machine homogenization, different combinations of foaming agent (solid, liquid) and surface agent (solid, liquid) are therefore used.

2 Materials and Methods

2.1 Analysis of precursors and their alkali-activated counterparts

Fly-ash (FA) (Traven et al., 2020), labelled 10 01 01, from Šoštanj power thermoplant, slag mixture (SM) (Češnovar et al., 2019), labelled 10 09 031, electric arc furnace slag from SIJ Acroni and ladle slag from SIJ Ravne, while glass wool waste (GW) (Horvat et al., 2018), labelled 17 09 041, and green waste ceramics (GWC) (Horvat and Ducman, 2019), labelled 10 12 011, were collected from Termit. The samples of all waste materials were collected in a way that is representative for landfills.

The metakaolin used in experiments (MK; Argeco) (Kramar et al., 2016; Provis et al., 2019) was used in the RILEM project and is not waste material.

X-ray fluorescence was performed on melted discs (XRF; Thermo Scientific ARL Perform'X Sequential XRF) prepared with $Fluxana_{(s)}$ (FX-X50-2, lithium tetraborate 50% / lithium metaborate 50%) to lower melting point and with the addition of $LiBr_{(l)}$ (prepared from 50 ml H_2O and 7.5 g of $LiBr_{(s)}$ from Acros Organics) to avoid sticking of the melt to the platinum vessel. The measured data were characterized by the UniQuant 5 software.

The X-ray powder diffraction (XRD; Empyrean PANalytical X-ray Diffractometer, Cu X-ray source) was solved with the software X'Pert Highscore plus 4.1. The Rietveld refinement was performed using an external standard (a pure Al_2O_3 crystal) to estimate the amount of amorphous phase and minerals in waste materials.

All samples used for XRF and XRD were dried at 70 °C for 24 h (WTB binder), ground with the vibrating disk mill (Siebtechnik) and sieved below 63 μm (SM), 90 μm (FA, GW and WGC).

The viscosity of alkali-activated slurries (a mixture of precursor, alkali activator and potential foam stabilizing additives) was measured with the viscometer Haake VT 500 with the detector PK2-1° (measurable viscosity range for this detector is from 0.04 Pa·s to 400 Pa·s) at 25 °C.

Fourier transform infrared spectroscopy (FTIR; PerkinElmer Spectrum Two) was performed on non-homogenized and homogenized alkali activated fly ash.

Scanning electron microscopy (SEM; Jeol JSM-IT500) to investigate surface, shape and microstructure was performed under high vacuum conditions on dried precursors and alkali-activated samples, both sputtered with Au. Energy-dispersive X-ray spectroscopy (EDXS; Oxford Instruments, Link Pentafet) mapping was performed on polished, non-sputtered, alkali-activated samples in low vacuum conditions. All alkali-activated samples for the analysis of SEM were dried in vacuum at 40 °C for 24 h (Kambič, VS 50 S).

The surface of a cross-section of polished vacuumed alkali-activated samples was also examined with a digital microscope (Tagarno FHD Trend) and software (Tagarno measuring software). Due to the sensitivity during polishing, especially of foam, the polishing was performed gently by hand.

Measurements of bending and compressive strength of alkali activated materials and foam were carried out with compression and bending strength testing machine (ToniTechnik ToniNORM) 1 day after demoulding unless otherwise stated.

The geometric density of alkali-activated samples was determined by weighting the sample and dividing its mass by its volume.

2.2 Preparation of precursors, activator and alkali-activated samples

All precursors used for alkali activation shown in Fig. 1 were prepared as shown:

- FA: used as received;
- FA*: FA and MK were used as received. Both precursors were mixed in mass ratio 3:1 respectively;
- SM: crushed in the gyratory crusher (Retsch BB50), ground in vibrating disk mill (Siebtechnik), sieved below 63 μm. Afterwards, both slags were mixed in mass ratio 1:1;
- GW: drying at 70 °C for 24 h, ground in cement mixer using iron balls and sieved below 63 μm;

– WGC: drying at 70 °C for 24 h, ground with a pestle and mortar and sieved below 1 mm.

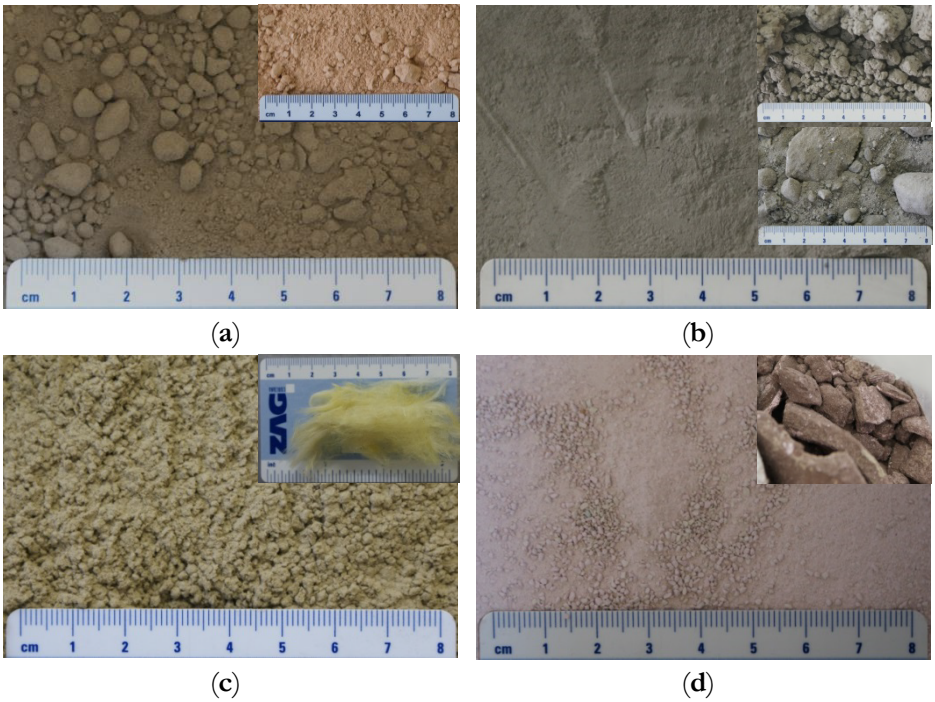

Figure 1: Photograph of precursors' state used in alkali activation: (a) FA, on the inset, is MK (larger particles fall apart when touched), (b) SM, (c) GW and (d) WGC. On the insets are photographs of the virgin material: (b-up) electric arc slag, (b-down) ladle slag, (c) GW, (d) WGC.

Surce: own.

For the alkali reaction versatile alkali activators were produced and/or used:

– FA: Alkali activator has been produced using ground glass powder (cathode ray tube waste glass) with an average particle size below 90 μm. After boiling for 6 h to 45 h, the prepared suspensions were filtered and the filtrates were analysed for silicon and aluminium content with an inductively coupled plasma optical emission spectrometer (ICP-OES, Varian, Model 715-ES): mass percentage of Na_2O 0.02%, the mass percentage of SiO_2 2.32%, and mass percentage of Al_2O_3 0.073%);

- FA*: Na-water glass "Crystal" (Crystal, 0112, Tennants distribution, with the mass percentage of Na_2O 18.8%, and mass percentage of SiO_2 37.0%) and $NaOH_{(s)}$ (Donau Chemie Ätznatron Schuppen, EINECS 215-785-5);
- SM: Na-water glass "Crystal" (Crystal, 0112, Tennants distribution, with a mass percentage of Na_2O 18.8%, and the mass percentage of SiO_2 37.0%);
- GW: Na-water glass "Termit" (Silvez, mining company Termit, with the mass percentage of Na_2O 12.8%, and mass percentage of SiO_2 29.2%) and $NaOH_{(s)}$ (Donau Chemie Ätznatron Schuppen, EINECS 215-785-5);
- WGC: Na-water glass "Geosil" (Geosil, 344/7, Woelner, with the mass percentage of Na_2O 16.9%, and the mass percentage of SiO_2 27.5%.

Preparation of alkali slurry:

- FA: precursor was manually mixed for 1 min with manually premixed alkali activator in mass ratio 3.37:1 respectively;
- FA*: precursor was manually mixed for 1 min with manually premixed alkali activators (Na-water glass "Crystal" and $NaOH_{(s)}$), foaming agent (H_2O_2, Carlo Erba reagents) and stabilizing agent (Na-dodecyl sulphate, Acros Organics) in mass ratio 2.66:1:0.05:0.04:0.04 respectively. The time of the start of the foaming reaction was estimated from the observation of bubble formation on the surface and volume growth;
- SM: precursor was manually mixed with manually premixed alkali activator (Na-water glass "Crystal"), foaming agent (Na-perborate monohydrate$_{(s)}$; Belinka Perkemija d.o.o.) and stabilizing agent (triton$_{(l)}$; X-100 Electrophoresis, Dow Chemical Company) in mass ratio 1.89:1:0.06:0.03 respectively. The time of the start of the foam reaction was estimated from the observation of bubble formation on the surface and volume growth;
- GW: precursor was mixed (up to 1000 rpm for 1 min with mixer Tehtnica Železniki, UM-405) with manually premixed alkali activators (Na-water glass "Termit" and $NaOH_{(s)}$) in the mass ratio 1.28:1:0.05 respectively;
- WGC: precursor was mixed (up to 1000 rpm for 1 min with mixer Tehtnica Železniki, UM-405) with alkali activator (Na-water glass "Geosil") in mass ratio 1.35:1 respectively.

Half of each slurry was homogenized in a three-roll mill (Exakt 80S) until the slurries did not change their visual texture.

All slurries were put into rubber-silicon moulds of size (80x20x20) mm^3 and cured (WTB Binder):

- FA: at 70 °C for 72 h;
- FA*: at 70 °C for 72 h;
- SM: at 60 °C for 24 h;
- GW: at 60 °C for 24 h;
- WGC: at 70 °C for 24 h.

Demoulding and drying process before measuring the mechanical strength:

- FA: the prisms were demoulded after cooling to room temperature and left at room temperature for an additional 24 h;
- FA*: the prisms were demoulded after cooling to room temperature and left at room temperature for an additional 24 h;
- SM: the prisms were demoulded after cooling to room temperature and right after the mechanical properties were measured;
- GW: the prisms were demoulded after cooling to room temperature and right after the mechanical properties were measured;
- WGC: the prisms were demoulded 3 weeks after curing at 70 °C and heat-treated at 105 °C for the additional 24 h (WTB Binder) because they were still not fully solidified.

3 Results and discussion

3.1 Analysis of precursor

SEM micrographs of all precursors prepared for alkali activation are shown in Fig. 2 under lower and higher magnification. FA consists of typical spheres (Fig. 2 (a) and (b)) (Kutchko and Kim, 2006), FA* from FA and large aggregates from MK (Fig. 2 (c) and (d)), GW from elongated cylindrical structures (Fig. 2 (g) and (h)), which are also longer than 63 μm (size of the mesh used), while both SM (Fig. 2 (e)

and (f)) and WGC (Fig. 2 (i) and (j)) come from randomly shaped particles with sharp edges by grinding.

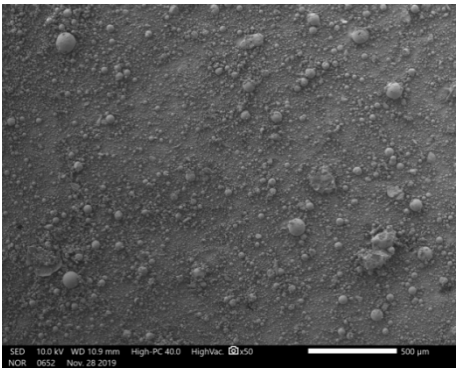

(**a**)

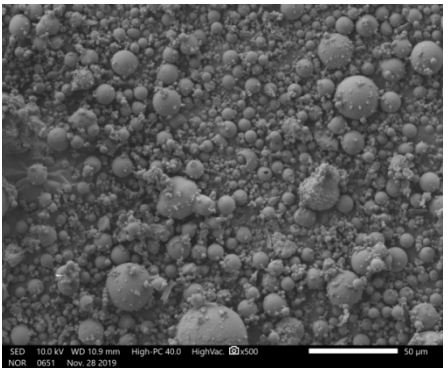

(**b**)

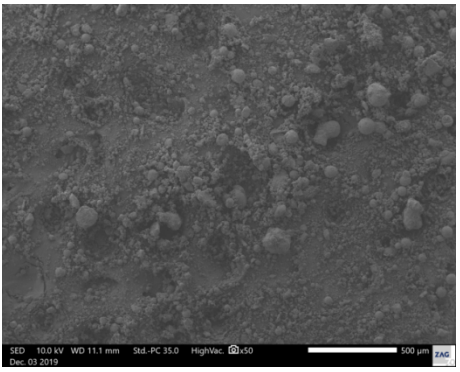

(**c**)

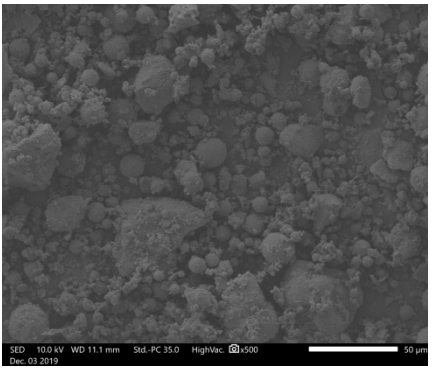

(**d**)

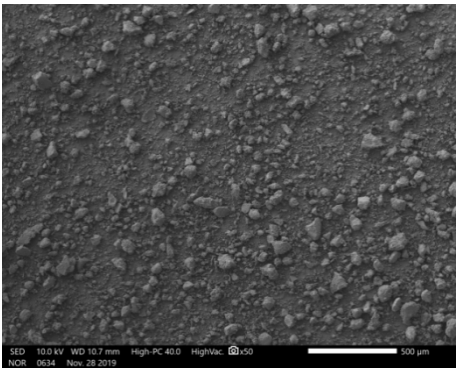

(**e**)

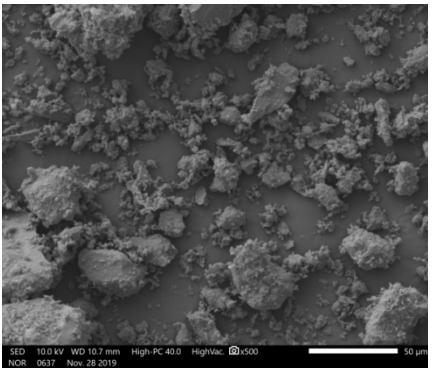

(**f**)

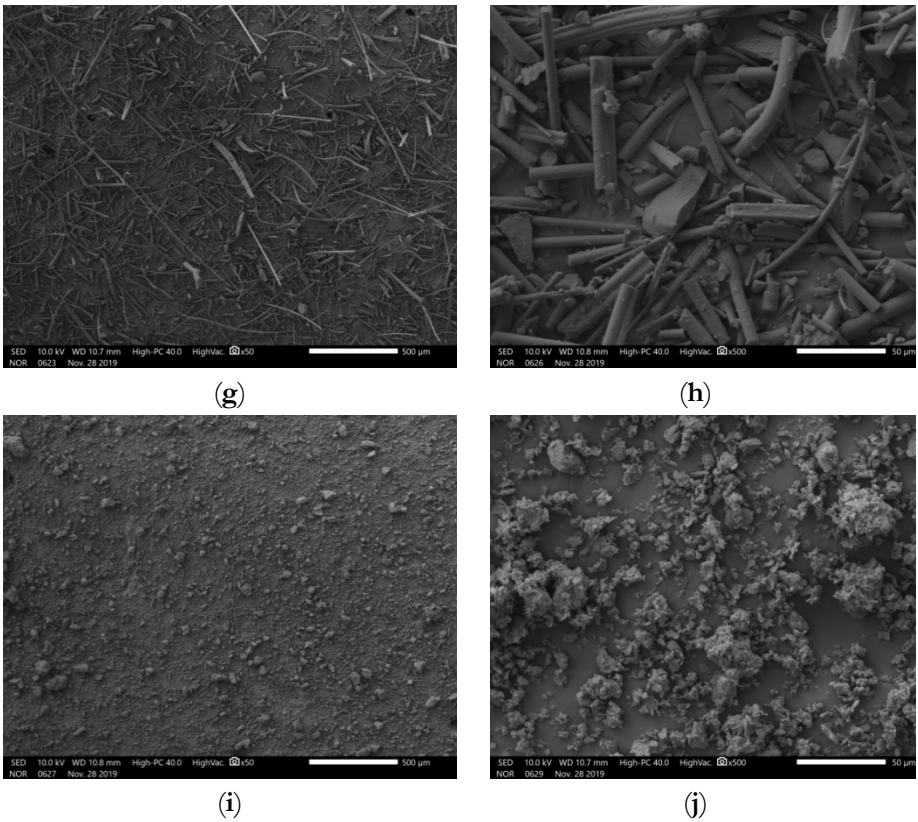

Figure 2: SEM micrographs of FA [(a) magnification 50x, (b) magnification 500x], FA* [(c) magnification 50x, (d) magnification 500x], SM [(e) magnification 50x, (f) magnification 500x], GW [(g) magnification 50x, (h) magnification 500x] and WGC [(i) magnification 50x, (j) magnification 500x].

Surce: own.

The chemical analysis of the precursor is presented in Table 1, with the first row of each precursor showing the mass percentages of elements detected by XRF, and the second row showing the mass percentages of elements in the crystalline phase determined by Rietveld refinement on XRD patterns, and in the third line, the mass percentages of the elements in the amorphous phase are shown, calculated as the difference between the amount of the mass percentage of an element determined using XRD and the mass percentage of an element in the crystalline phase.

Table 1: The first row of each precursor shows the mass percentage of elements measured by XRF, the second row shows the mass percentage of elements in a crystalline phase determined by Rietveld refinement from XRD, and the third row shows the mass percentage of elements in the amorphous phase.

Precursor	Elements/m%	Na	K	Cs	Mg	Ca	Sr	Ba	Al	Si
FA	XRF	0.89	1.83	0	1.69	8.85	0.05	0.07	12.16	20.91
	XRD	0	0	0	0.38	1.64	0	0	1.74	4.32
	XRF-XRD	0.89	1.83	0	1.31	7.21	0.05	0.07	10.42	16.59
FA*	XRF	0.66	1.41	0	1.30	6.72	0.04	0.06	12.50	23.85
	XRD	0	0	0	0.39	1.33	0	0.01	1.56	7.12
	XRF-XRD	0.66	1.41	0	0.91	5.39	0.04	0.05	10.94	16.73
SM	XRF	0.23	0.17	0	14.28	21.58	0.04	0.03	4.47	9.87
	XRD	0	0	0	5.43	11.12	0	0.02	1.07	6.03
	XRF-XRD	0.23	0.17	0	8.85	10.46	0.04	0.01	3.40	3.84
GW	XRF	12.24	0.29	0	2.22	5.10	0	0.06	1.32	30.73
	XRD	0	0	0	0.18	0.54	0	0	0	2.61
	XRF-XRD	12.24	0.29	0	2.03	4.56	0	0.06	1.31	28.12
WGC	XRF	0.25	3.66	0	0.87	2.41	0.02	0.36	12.24	28.76
	XRD	0	0	0	0.72	2.41	0	0	4.02	14.81
	XRF-XRD	0.25	3.66	0	0.15	0	0.02	0.36	8.22	13.95

The optimum ratio of the amount of substance in the alkaline activated final sample is $n_{Na+K}:n_{Al}:n_{Si}=1:1:1.9$ (Duxson et al., 2005), which was experimentally proven in our investigations at the WGC, where we only considered elements in the amorphous phase (Horvat and Ducman, 2019). An increased ratio (normalized to the amount of substance Al), where the whole first and second group of the periodic system are taken into account ($n_{1st}:n_{2nd}:n_{Al}:n_{Si}$), is for precursors:

- FA: 0.22:0.61:1:1.53;
- FA*: 0.16:0.43:1:1.47;
- SM: 0.11:4.97:1:1.09;
- GW: 11.05:4.05:1:20.57;
- WGC: 0.34:0:1:1.64.

If only elements from the first group of the periodic system are considered, for FA, FA* (addition of MK to FA lowered amounts of elements from the first and second group, and lowered ratio Si:Al), SM and GWC addition of Na (element of the first group) and Si is required, which can be both added with Na-water glass and a potentially insufficient amount of Na with NaOH, while in GW too much Na (to avoid efflorescence) is present even without alkali activator, i.e. GW can only be used as an additive to other precursors.

If elements from the second group are also considered, it is noticeable that FA, FA* and SM contain more amorphous elements from the second group than from the first group. When considering that 1 element from the second group can compensate "wrong" Al charge in the matrix for 2 Al, the normalized amount of substance of Al that can be compensated from both cationic groups present in the precursor is:

- FA: 1.44;
- FA*: 1.02;
- SM: 10.05;
- GW: 19.15;
- WGC: 0.68.

From the above list, it can be concluded that the addition of cations from alkali activators to the precursors FA, FA*, SM and GW lead to efflorescence because the final normalized (normalization to the amount of substance for Al) amount of substance of the cations should have the value 1 (this value is already higher for the precursor without alkali additives alone). The only precursor with a lower substance quantity of the first and second group before the addition of alkali activators is the WGC, which is the only precursor among the selected precursors, with which efflorescence can be avoided if the alkali activators are selected correctly if minerals found in precursors with XRD (Fig. 3) do not dissolve in alkali.

- Fig. 3 shows the XRD measurements of all precursors and their Rietveld refinement results (the GOF value of all analyzed samples was below 10 - the value is higher because the precursors are (mostly) waste products and several peaks on the XRD samples could not be determined and are contained in the amount of the amorphous phase). The highest amount of amorphous phase is GW (90%), followed by FA (80%), FA* (70%), WGC (50%) and SM (40%). The higher amount of amorphous phase can lead to a higher amount of aluminosilicate network in the final alkaline activated material. Minerals that are detected with XRD when they do not react with alkali or become unstable at the curing temperature represent aggregates of different Mohs hardness in the final product, i.e. when they have a higher hardness than the alkaline activated sample has higher compressive strength

(Horvat and Ducman, 2019). The only mineral present in all precursors is quartz, which accounts for a higher mass percentage in all precursors used (Fig. 3).

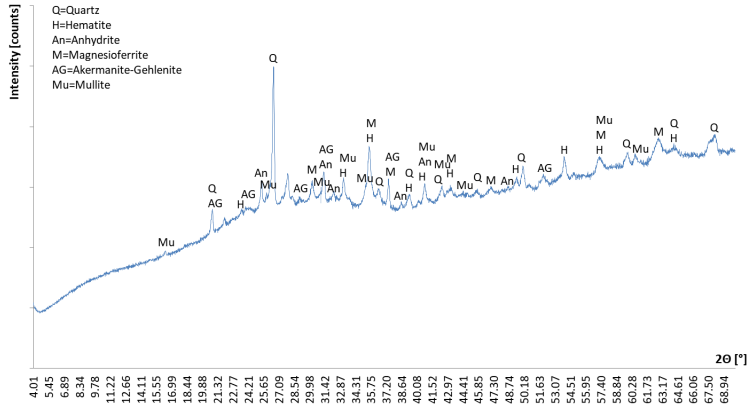
Q=Quartz
H=Hematite
An=Anhydrite
M=Magnesioferrite
AG=Akermanite-Gehlenite
Mu=Mullite
Intensity [counts]
2Θ [°]

(a)

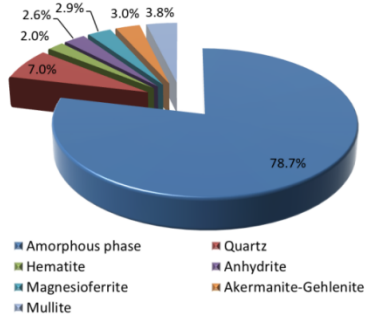
2.6%
2.9%
3.0%
3.8%
2.0%
7.0%
78.7%
Amorphous phase
Quartz
Hematite
Anhydrite
Magnesioferrite
Akermanite-Gehlenite
Mullite

(b)

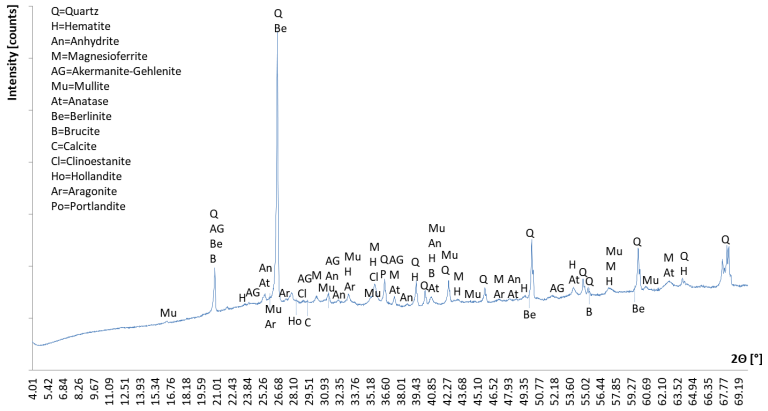
Q=Quartz
H=Hematite
An=Anhydrite
M=Magnesioferrite
AG=Akermanite-Gehlenite
Mu=Mullite
At=Anatase
Be=Berlinite
B=Brucite
C=Calcite
Cl=Clinoestanite
Ho=Hollandite
Ar=Aragonite
Po=Portlandite
Intensity [counts]
2Θ [°]

(c)

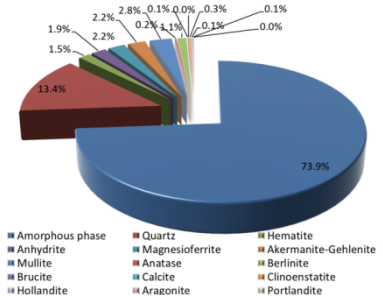
1.9%
2.2%
2.8%
0.1%
0.0%
0.3%
0.1%
1.5%
2.2%
0.2%
1.1%
0.1%
0.0%
13.4%
73.9%
Amorphous phase
Quartz
Hematite
Anhydrite
Magnesioferrite
Akermanite-Gehlenite
Mullite
Anatase
Berlinite
Brucite
Calcite
Clinoenstatite
Hollandite
Aragonite
Portlandite

(d)

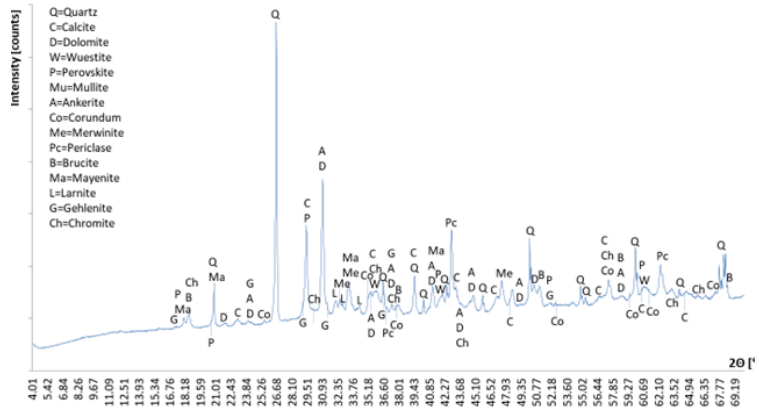
Q=Quartz
C=Calcite
D=Dolomite
W=Wuestite
P=Perovskite
Mu=Mullite
A=Ankerite
Co=Corundum
Me=Merwinite
Pc=Periclase
B=Brucite
Ma=Mayenite
L=Larnite
G=Gehlenite
Ch=Chromite
Intensity [counts]
2θ [°]

(e)

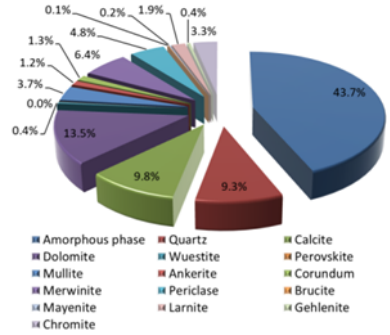
43.7%
13.5%
9.8%
9.3%
6.4%
4.8%
3.3%
1.9%
1.3%
1.2%
3.7%
0.2%
0.1%
0.0%
0.4%
0.4%
Amorphous phase
Quartz
Calcite
Dolomite
Wuestite
Perovskite
Mullite
Ankerite
Corundum
Merwinite
Periclase
Brucite
Mayenite
Larnite
Gehlenite
Chromite

(f)

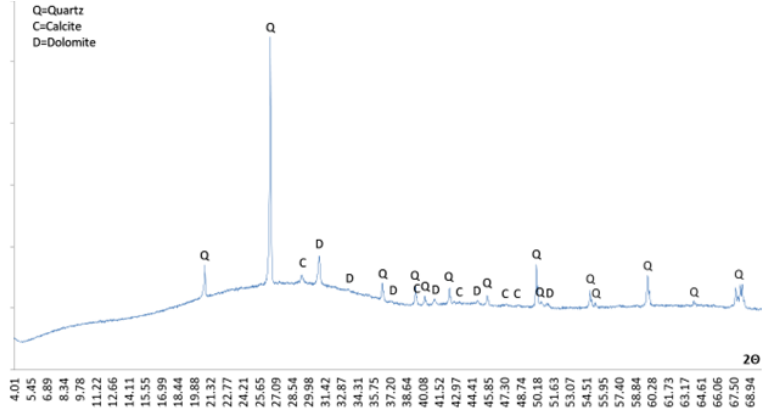
Q=Quartz
C=Calcite
D=Dolomite
2θ

(g)

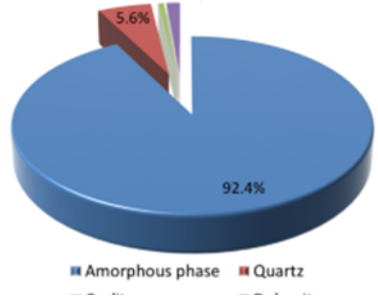
92.4%
5.6%
Amorphous phase
Quartz

(h)

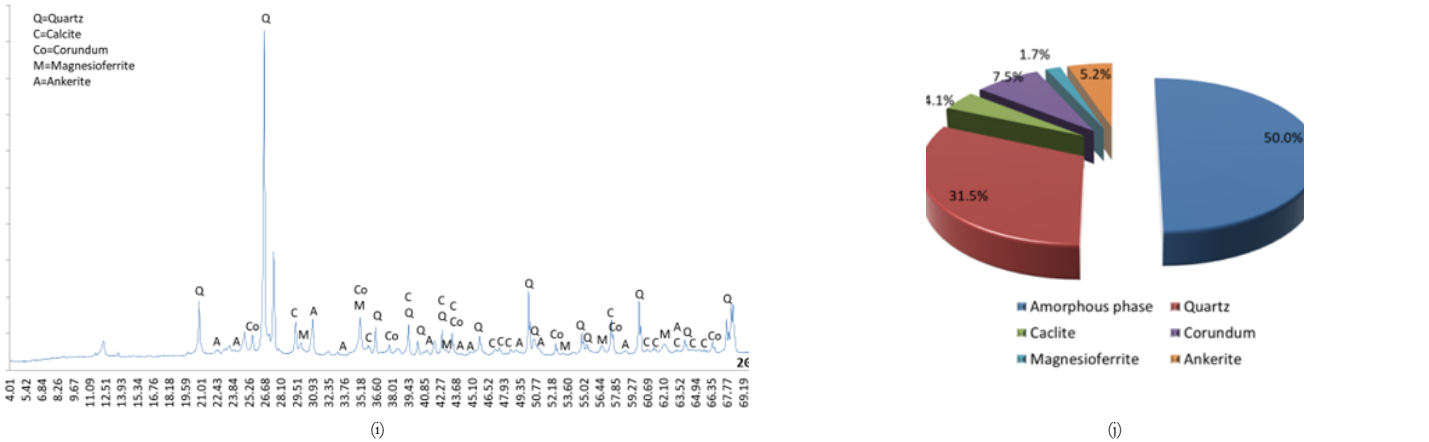

(i) (j)

Figure 3: XRD pattern of (a) FA, (c) FA*, (e) SM, (g) GW and (i) GWC. Rietveld refinement of (b) FA, (d) FA*, (f) SM, (h) GW and (j) GWC.
Source: own.

3.2 Analysis of alkali-activated samples

During homogenization of FA slurry gas (white-grey smoke) was produced, while during homogenization of other mixtures slurries became visually just smoother and easier to handle.

The compressive and flexural strength of all alkaline activated samples produced from homogenized and non-homogenized slurries are shown in Table 2 together with the viscosity of the slurries and the density of the final products. The viscosity decreases with homogenization from high to measurable high for alkaline activated material from GW, for alkaline activated materials from FA for 55% and from WGC for 60%, for alkaline activated foams from FA* for 15% and from SM for 30%. The compressive strength was increased for all tested samples, i.e. for alkaline activated materials from GW by 25%, from FA by 55% and from WGC by 70%, for alkaline activated foams from FA* by 75% and SM by 50%. The flexural strength was also increased for all samples tested, i.e. for alkaline activated materials from GW by 10%, from FA by 30% and from WGC by 80%, for alkaline activated foams from FA* by 100% and from SM from non-existent to 10% of the value of the flexural strength of alkaline activated material from GW.

Table 2: The density of alkali-activated samples, their compressive and bending strengths in the dependence of preparation of alkali slurry, with and without (intact) homogenization.

Precursor	Preparation of the slurry	Viscosity of the slurry/ Pa·s	Compressive strength/ MPa	Bending strength/ MPa	Density/ kg/l
FA	Intact	5.03	30.25	7.20	1.71
	Homogenization	2.23	46.76	9.46	1.77
FA*	Intact	0.90	3.23	2.11	0.70
	Homogenization	0.75	5.67	4.27	0.84
SM	Intact	1.08	0.92	0	0.64
	Homogenization	0.76	1.38	1.71	0.64
GW	Intact	torque overload	54.91	14.00	1.75
	Homogenization	41.13	69.87	15.86	1.79
WGC	Intact	6.43	11.03	9.05	1.87
	Homogenization	2.55	19.00	16.13	1.35

Mechanical strength of alkali-activated foams increased less if foaming did not start too early because the homogenization did not influence the foaming of the slurry, i.e. final density of alkali-activated foam did not change, the material was just homogenized in its pre-foaming time (SM was foamed with Na-perborate which started to foam approximately 5 min after precursor was mixed with foaming and stabilizing agent, i.e. after 1 min of mixing there were still approximately 4 min for homogenization and moulding), i.e. under the digital microscope, there was no obvious difference in pore size and distribution with and without homogenization (Fig. 4 (e) and (f) respectively).

If foaming started during homogenization, gas bubbles were removed from the slurry mechanically and final density of the alkali-activated foam was higher due to homogenization and gas bubble-removal (FA* was foamed with H_2O_2 which started to react during 1 min time of mixing of the precursor with foaming and stabilizing agent, i.e. homogenization and moulding do influence final properties of the foam). Homogenization during foaming also affected bubble distribution and size, i.e. homogenized sample has smaller, more uniformly sized and more uniformly distributed pores, as it is presented on Fig. 4 (c) and (d), i.e. sample without and with homogenization respectively.

Bloating of WGC occurred during drying at 110 °C and was more pronounced when the material was homogenized (Fig. 4 (j)), due to the alkali activation of the whole material, while non-reacted precursors were observed with intact alkali-activated material (light pink and white-yellow particles in Fig. 4 (i); the alkali did not reach the inner volume of the particles of the precursor, which were additionally crushed and dispersed with homogenization). One consequence of the bloating was a decrease in density of almost 30%, which has a negative effect on mechanical strength, i.e. an increase in bending and mechanical strength of homogenized material dried by methods that avoid bloating would result in an even greater increase in mechanical strength. Figure 4: Microphotographs of vacuumed polished alkali-activated samples' cross-sections performed with a digital microscope at magnification 25 for FA [(a) intact, (b) homogenized], FA* [(c) intact, (d) homogenized], SM [(e) intact, (f) homogenized], GW [(g) intact, (h) homogenized] and WGC [(i) intact, (j) homogenized].

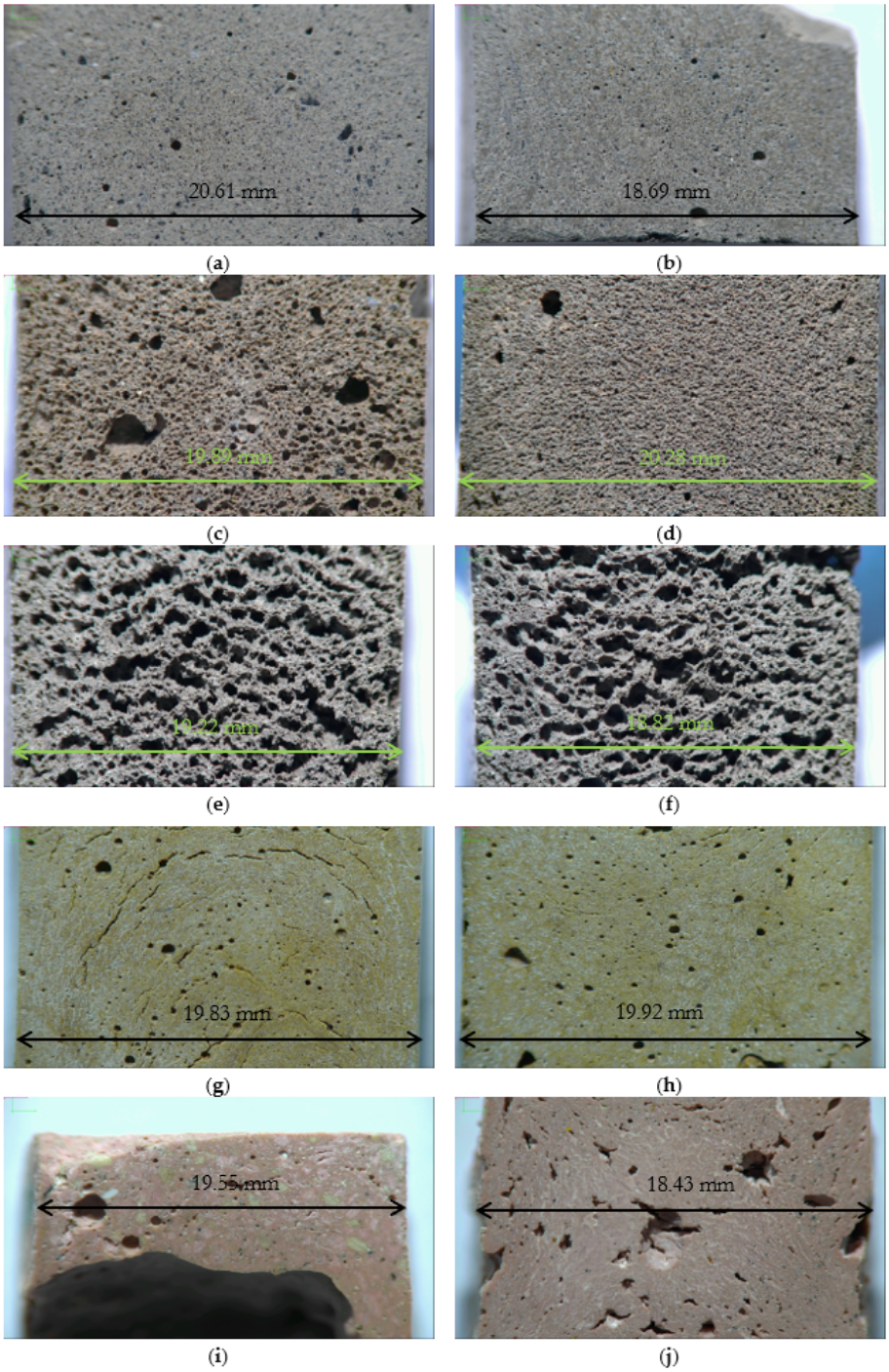
20.61 mm
(a)
18.69 mm
(b)
19.59 mm
(c)
20.28 mm
(d)
19.42 mm
(e)
18.82 mm
(f)
19.83 mm
(g)
19.92 mm
(h)
19.55 mm
(i)
18.43 mm
(j)

Figure 4: Microphotographs of vacuumed polished alkali-activated samples' cross-sections performed with a digital microscope at magnification 25 for FA [(a) intact, (b) homogenized], FA* [(c) intact, (d) homogenized], SM [(e) intact, (f) homogenized], GW [(g) intact, (h) homogenized] and WGC [(i) intact, (j) homogenized]

Alkali-activated GW without homogenization showed circular longitudinal pores (Fig. 4 (g)), which are a consequence of manual moulding of slurry that is too viscous (almost as bulk material), whereas these pores are not observed in homogenized alkali-activated GW (Fig. 4 (h)), therefore, the higher mechanical strength of the homogenized sample. FA Alkali-activated without homogenization contains larger black, non-spherical particles that are not present in the homogenized sample (Fig. 4 (a) and (b) respectively).

Fig. 5 shows intact alkali-activated FA and Fig. 6 shows homogenized alkali-activated FA.

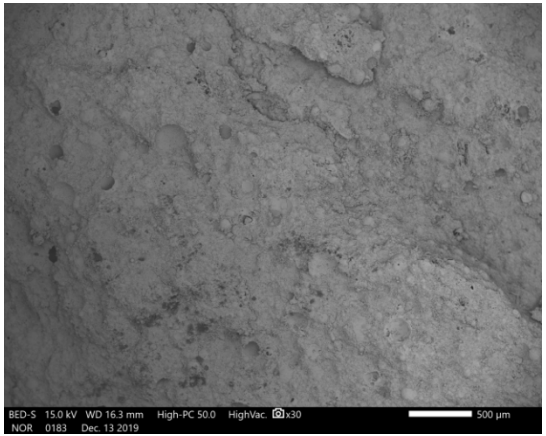

(**a**)

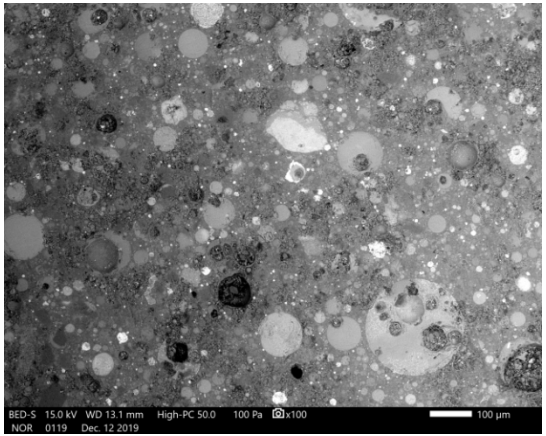

(**b**)

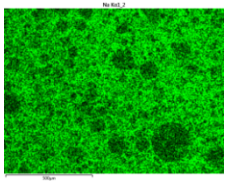

(b-Na)

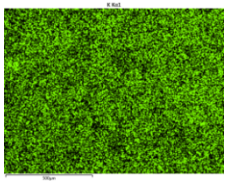

(b-K)

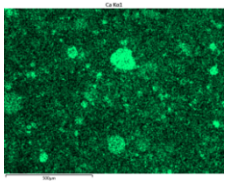

(b-Ca)

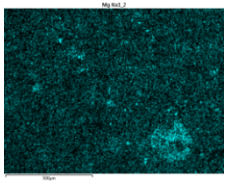

(b-Mg)

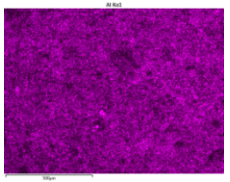

(b-Al)

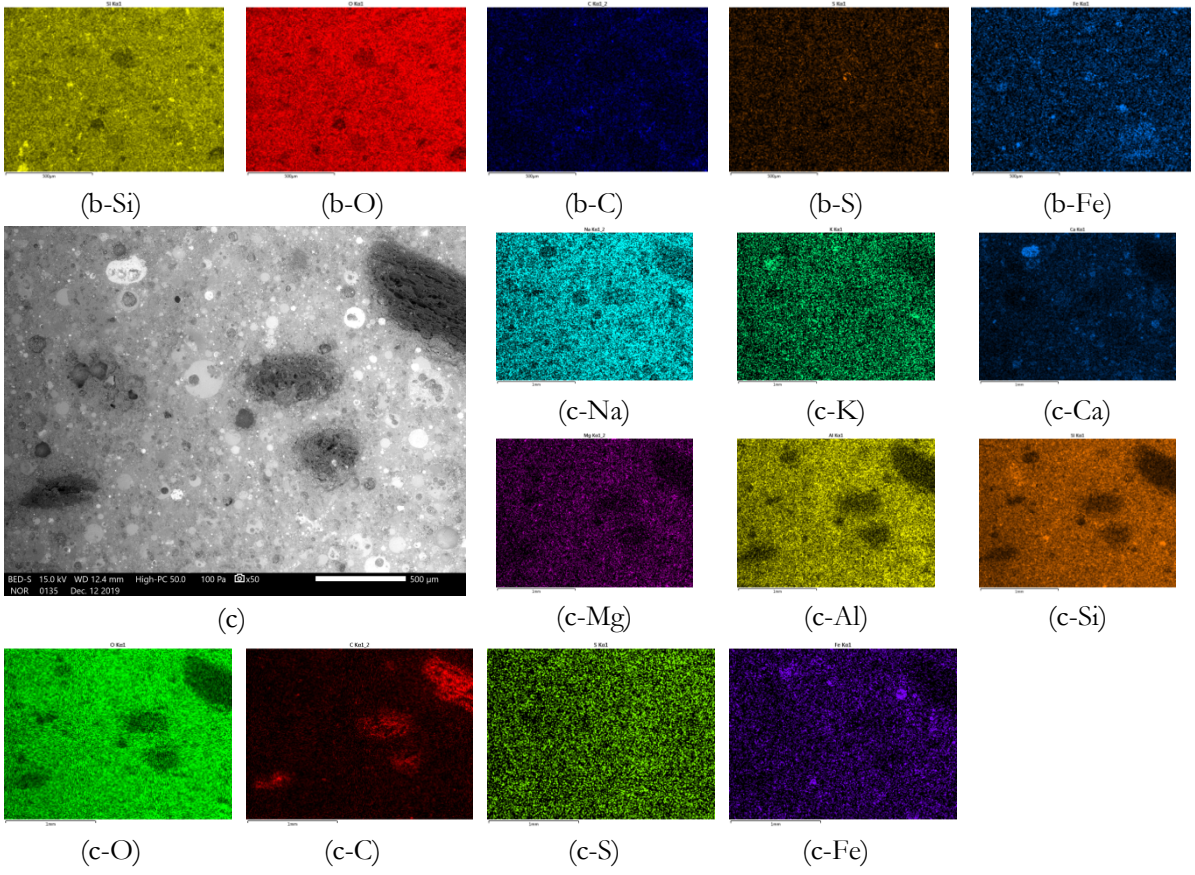

Figure 5: SEM micrograph of intact alkali-activated FA with magnification (a) 30 (intact cross-section after compressive strength test, vacuumed and sputtered with Au, observed at HV), (b) 100 and (c) 50 (cut and polished cross-section, observed at LV). The EDXS mapping of micrograph (b), (c) is presented on (b-chemical element), (c-chemical element) respectively.
Source: own.

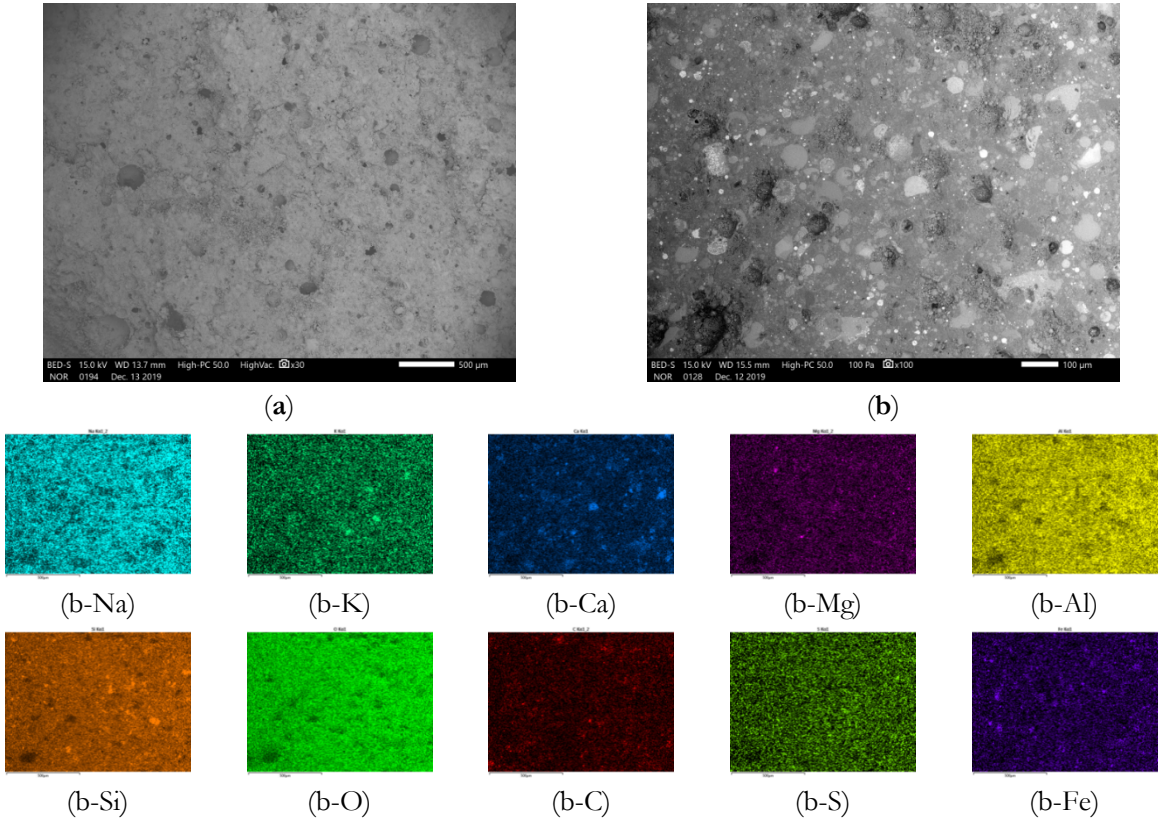

Figure 6: SEM micrograph of homogenized alkali-activated FA with magnification (a) 30 (intact cross-section after compressive strength test, vacuumed and sputtered with Au, observed at HV) and (b) 100 (cut and polished cross-section, observed at LV). The EDXS mapping of micrograph (b) is presented on (b-chemical element). Source: own.

Fig. 5 (a) and Fig. 6 (a) show that there is no difference in the aluminosilicate network, its polished counterparts in Fig. 5 (b) and Fig. 6 (b) show that homogenization led to the grinding of large fly ash spheres that consist from elements of the second group, which were not reacted according to the EDXS analysis, which is beneficial to the product since this improved the ratio of the first and second group to Al, which means that efflorescence could be avoided or at least minimized.

In an intact alkali-activated FA network, incompletely burned organic parts of coal and wood were trapped (Fig. 5 (c)), which were not visible in the homogenized sample. These parts look black to the naked eye under an optical microscope (Fig. 4 (a)) and also under SEM (Fig. 5 (c)), made of C according to EDXS analysis (Fig. 5 (c-C)).

From all EDXS mappings of intact and homogenized alkali-activated FA (Fig. 5 and Fig. 6), it can be concluded that the homogenization also led to a better uniformity of all elements in the alkali-activated sample.

Fig. 7 shows the FTIR analysis of intact and homogenized alkali-activated FA. C-C bonds are present in the intact sample (bands around 1450 cm^{-1} and 890 cm^{-1} belong to the stretching and bending of C-C bonds (Ahmed et al., 2013)), while they have disappeared in the homogenized sample, which proves that the emission of smoke from the slurry during homogenization was the result of the combustion of cellulose (observed under SEM only in intact alkali-activated FA samples, shown in Fig. 5(c)) from the incomplete combustion of coal and wood.

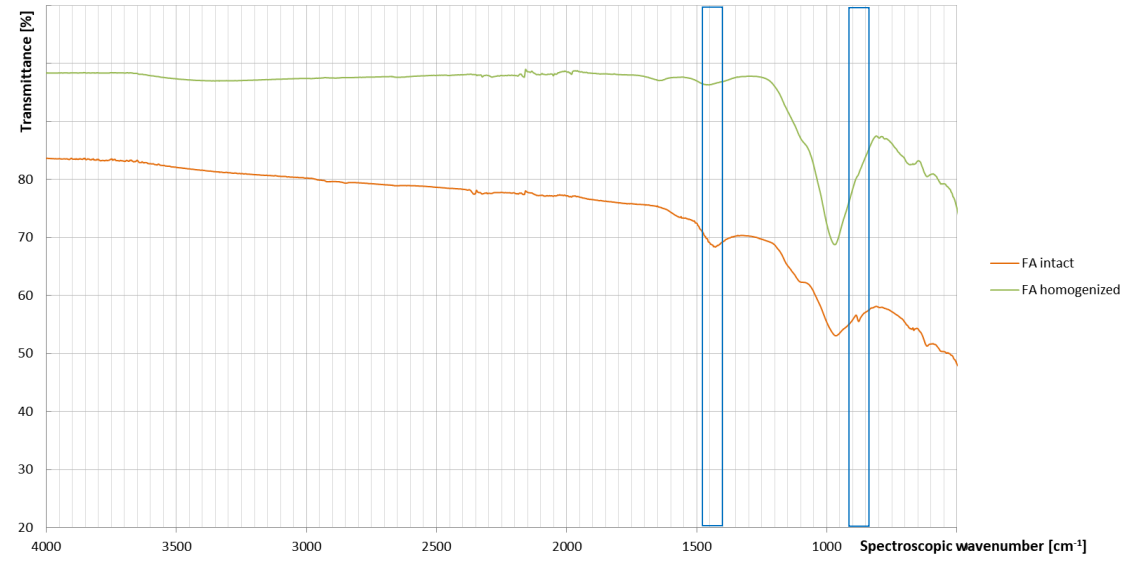

Figure 7: Photo FTIR spectra of intact (orange line) and homogenized (green line) FA.
Source: own.

Fig. 8 shows intact alkali-activated FA* and Fig. 9 shows homogenized alkali-activated FA*:

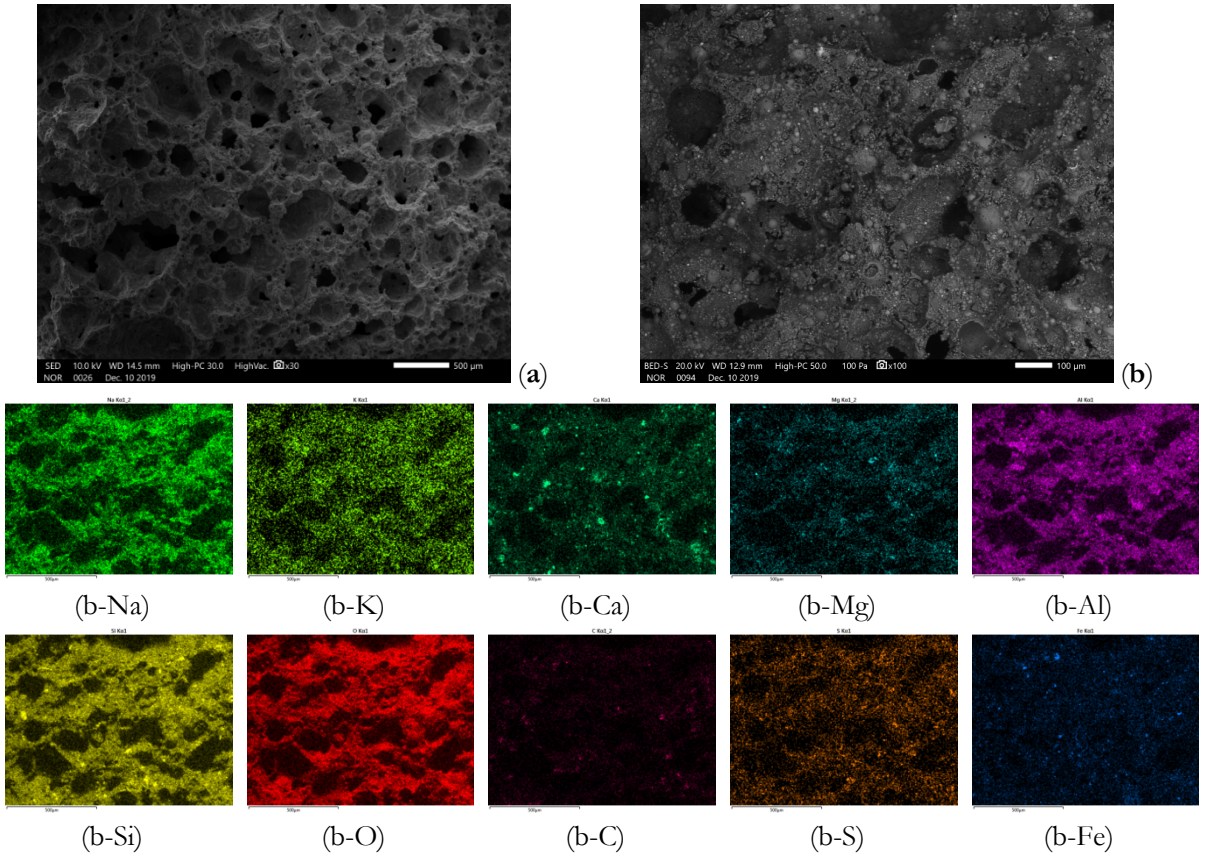

Figure 8: SEM micrograph of intact alkali-activated FA* with magnification (a) 30 (intact cross-section after compressive strength test, vacuumed and sputtered with Au, observed at HV) and (b) 100 (cut and gently polished cross-section, observed at LV). The EDXS mapping of micrograph (b) is presented on (b-chemical element). Source: own.

When comparing Fig. 8 (a) and Fig. 9 (a), it becomes clear that the aluminosilicate network shows no visible change, while the pores are more uniform in size and more uniformly distributed after homogenization. The mean value of pore size from SEM micrographs of intact alkali-activated FA* is 240.4 μm (standard deviation 173.7 μm), while the mean value for homogenized alkali-activated FA* is 98.9 (standard deviation 40.4 μm). The value decreased by 60% and the pores are more homogeneously distributed according to the decrease of the standard deviation (4-times) compared to the mean value of the pore diameter (2-times).

From the EDXS analysis of alkali-activated FA* polished counterparts (shown in Fig. 8 (b) and Fig. 9 (b)), it is the same as for the alkali-activation of FA (Fig. 5 and Fig. 6), i.e. spheres from elements from the second group did not react and are simply ground after homogenization, which leads to a better element distribution over the entire alkali-activated FA* (Fig. 8 (b-element) and Fig. 9 (b-element)).

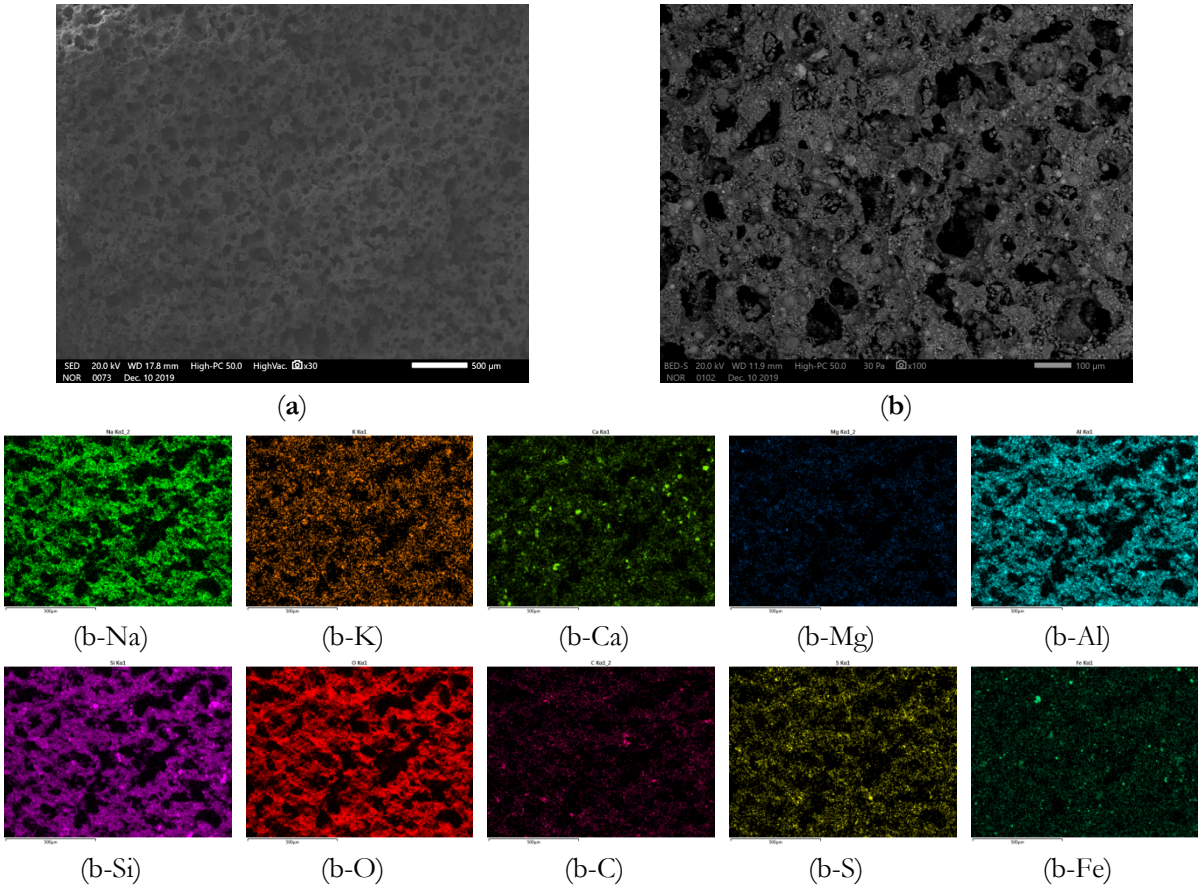

Figure 9: SEM micrograph of homogenized, alkali-activated FA* with magnification (a) 30 (intact cross-section after compressive strength test, vacuumed and sputtered with Au, observed under HV) and (b) 100 (cut and gently polished cross-section, observed under LV). The EDXS mapping of the micrograph (b) is presented under (b-chemical element). Source: own.

Fig. 10 shows intact alkali-activated SM and Fig. 11 shows homogenized alkali-activated SM. The aluminosilicate network before and after homogenization of SM presented in Fig. 10 (a) and Fig. 11 (a) shows no change. The statistics of the measured pores on SEM micrographs show that the mean value of the pore size of intact, alkali-activated SM is 533.8 μm (standard deviation 275.1 μm), while the mean value for homogenized, alkali-activated SM is 444.7 μm (standard deviation 178.4 μm). The value decreased by 15%, and the pores are more homogeneously distributed according to the decrease in standard deviation (1.5 times) compared to the mean value of the pore diameter (1.2 times). When comparing the EDXS results for intact and homogenized SM (Fig. 10 (b-element) and Fig. 11 (b-element) it can be concluded that after homogenization the distribution of the elements in the aluminosilicate network is somewhat more uniform.

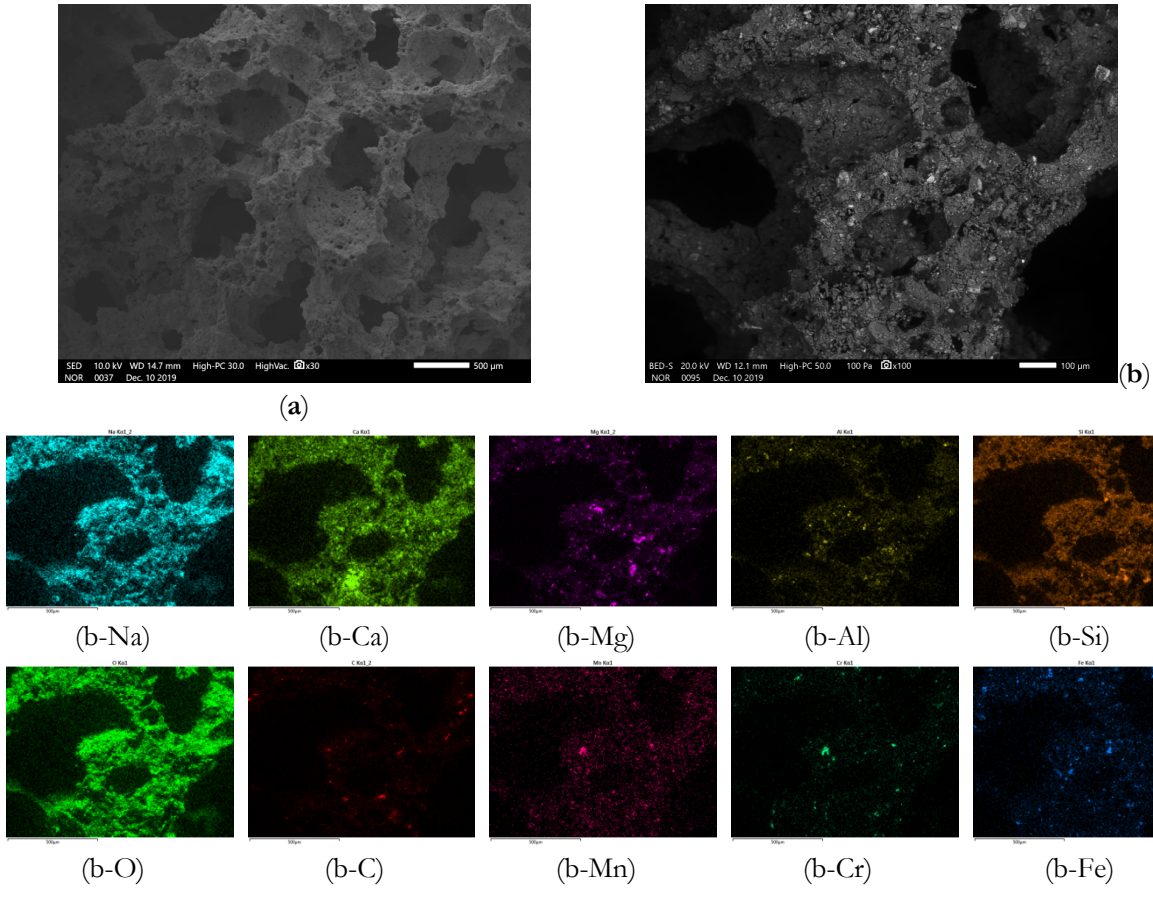

Figure 10: SEM micrograph of intact alkali-activated SM with magnification (a) 30 (intact cross-section after compressive strength test, vacuumed and sputtered with Au, observed at HV) and (b) 100 (cut and gently polished cross-section, observed at LV). The EDXS mapping of the micrograph (b) is presented on (b-chemical element). Source: own.

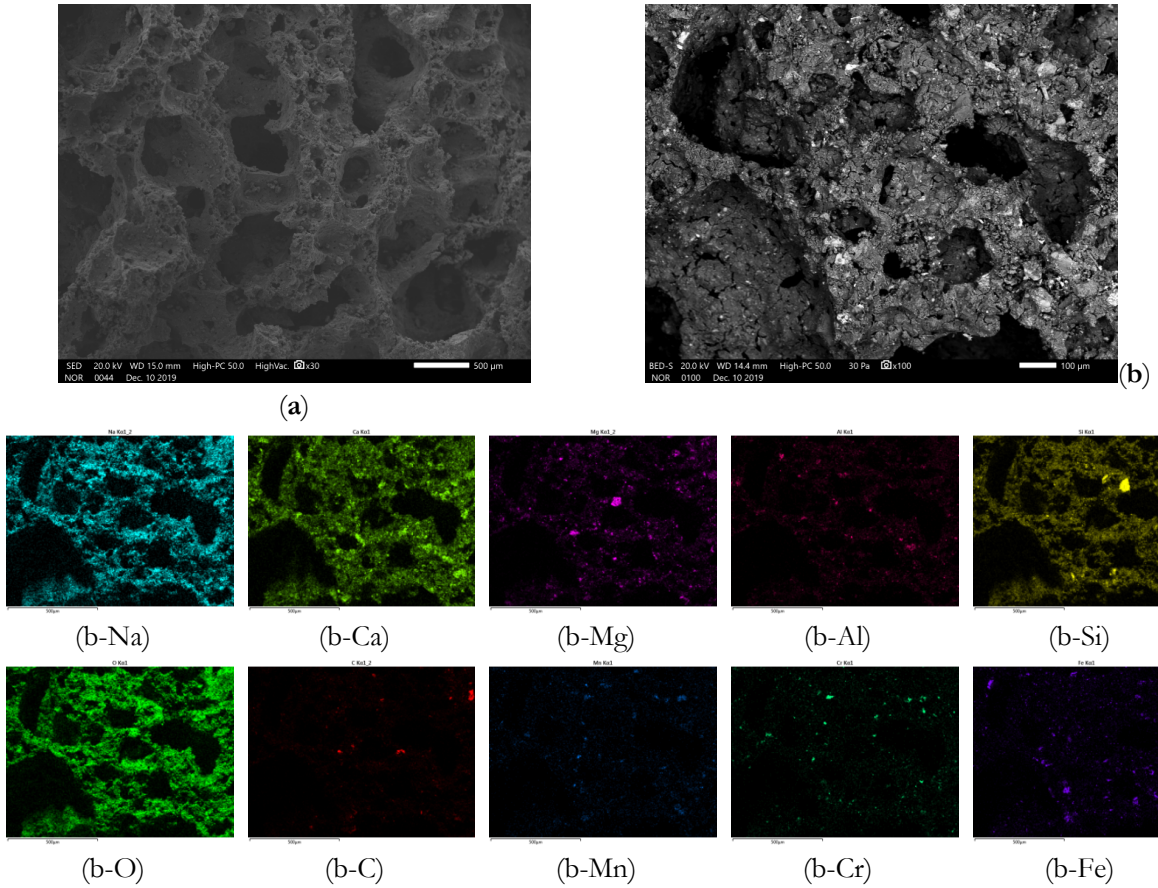

Figure 11: SEM micrograph of homogenized alkali-activated SM with magnification (a) 30 (intact cross-section after compressive strength test, vacuumed and sputtered with Au, observed at HV) and (b) 100 (cut and gently polished cross-section, observed at LV). The EDXS mapping of the micrograph (b) is presented on (b-chemical element. Source: own.

Fig. 12 shows intact alkali-activated GW and Fig. 13 shows homogenized alkali-activated GW.

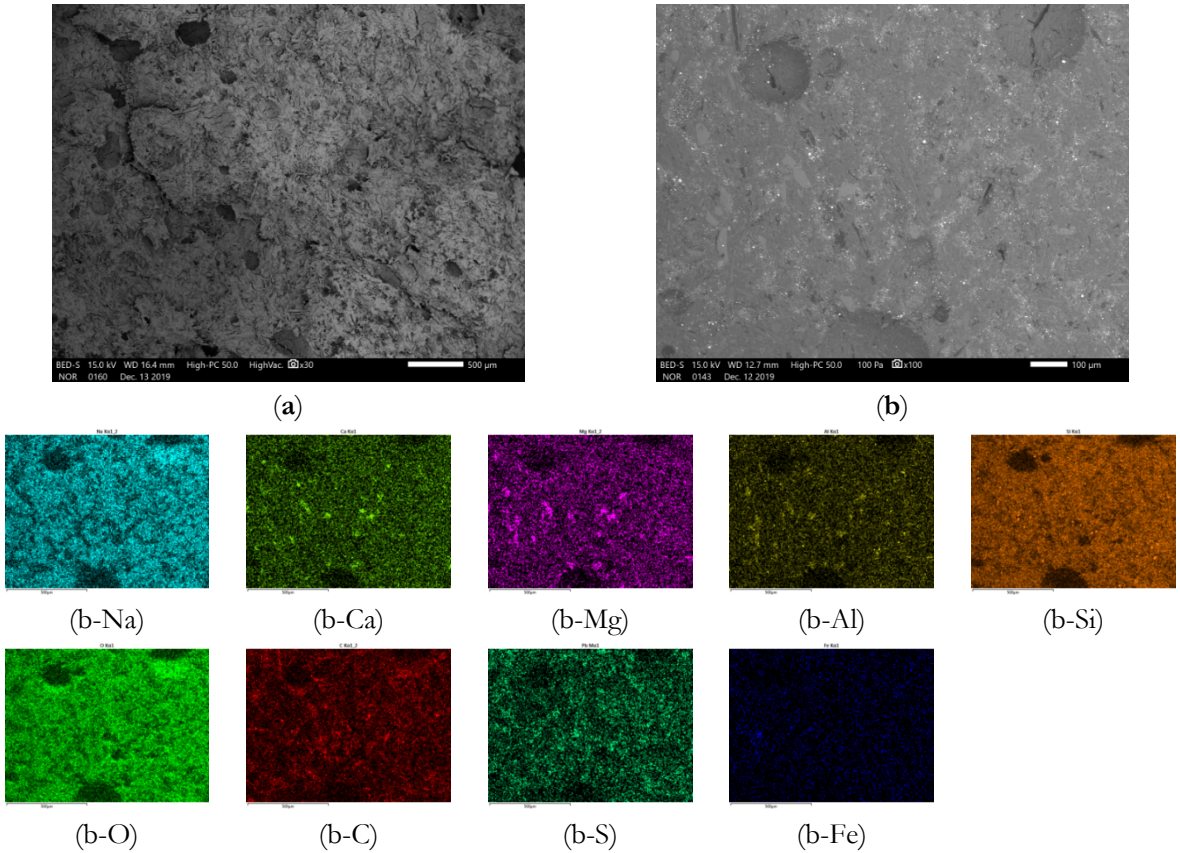

Figure 12: SEM micrograph of intact alkali-activated GW with magnification (a) 30 (intact cross-section after compressive strength test, vacuumed and sputtered with Au, observed at HV) and (b) 100 (cut and polished cross-section, observed at LV). The EDXS mapping of micrograph (b) is shown under (b-chemical element). Source: own.

The aluminosilicate network of GW with and without homogenization shows no visual difference (Fig. 12 (a) and Fig. 13 (a)), while from the EDXS analysis on the polished samples (Fig. 12 (b-element) and Fig. 13 (b-element)) it can be concluded that homogenization has a great influence on the distribution of the elements, which are somewhat more uniform in the homogenized sample.

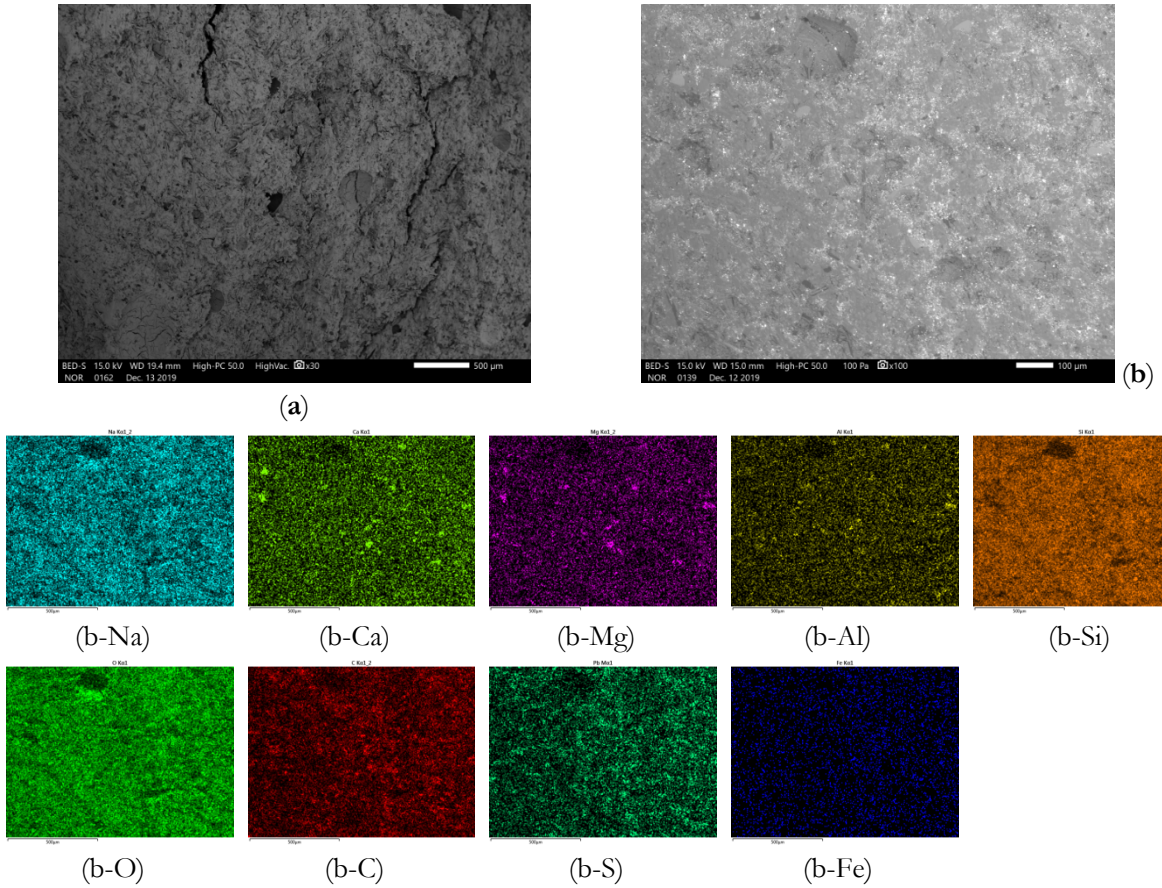

Figure 13: SEM micrograph of homogenized alkali-activated GW with magnification (a) 30 (intact cross-section after compressive strength test, vacuumed and sputtered with Au, observed at HV) and (b) 100 (cut and polished cross-section, observed at LV). The EDXS mapping of micrograph (b) is shown under (b-chemical element). Source: own.

Fig. 14 shows intact alkali-activated WGC and Fig. 15 homogenized alkali-activated WGC. There is no visual difference in the aluminosilicate network (Fig. 14 (a) and Fig. 15 (a)), while there is a difference in the distribution of the network due to bloating (non-thermally stable chemicals that change to gas when exposed to higher/high temperatures) after exposure to 105 °C for 24 h. In the intact sample bloating is less pronounced, random and with spherical bubbles, whereas in the homogenized sample is layered and perpendicular to the direction of moulding. From the EDXS analysis (Fig. 14 (b-element) and Fig. 15 (b-element), which was performed on polished samples and is shown in Fig. 14 (b) and Fig. 15 (b) respectively, it can be seen that the precursor itself was well homogenized, i.e. the distribution of the elements in the entire volume of the alkali-activated material is uniform with and without homogenization (EDXS sees no difference between unreacted and reacted parts of the alkali-activated WGC visible to the naked eye and shown in Fig. 4 (i) and (j)).

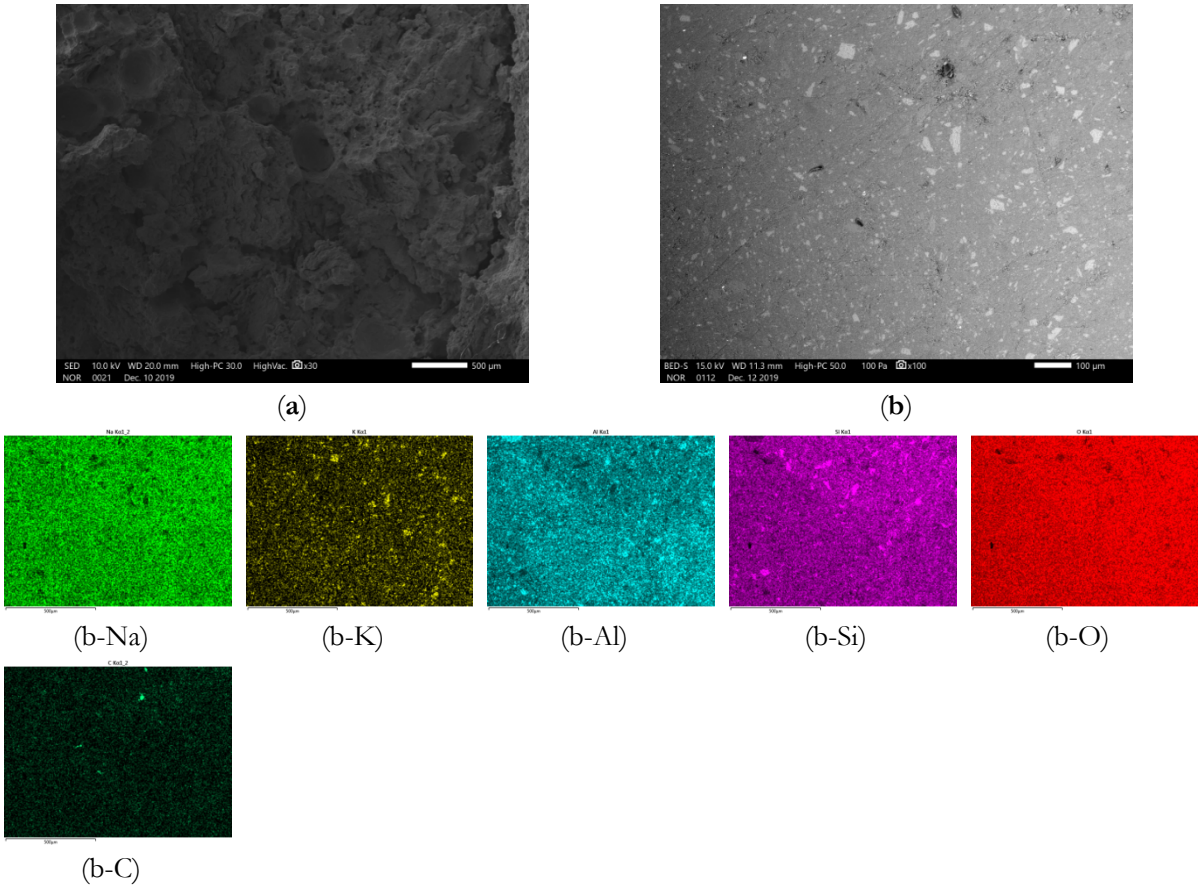

Figure 14: SEM micrograph of intact alkali-activated WGC with magnification (a) 30 (intact cross-section after compressive strength test, vacuumed and sputtered with Au, observed at HV) and (b) 100 (cut and polished cross-section, observed at LV). The EDXS mapping of the micrograph (b) is presented on (b-chemical element). Source: own.

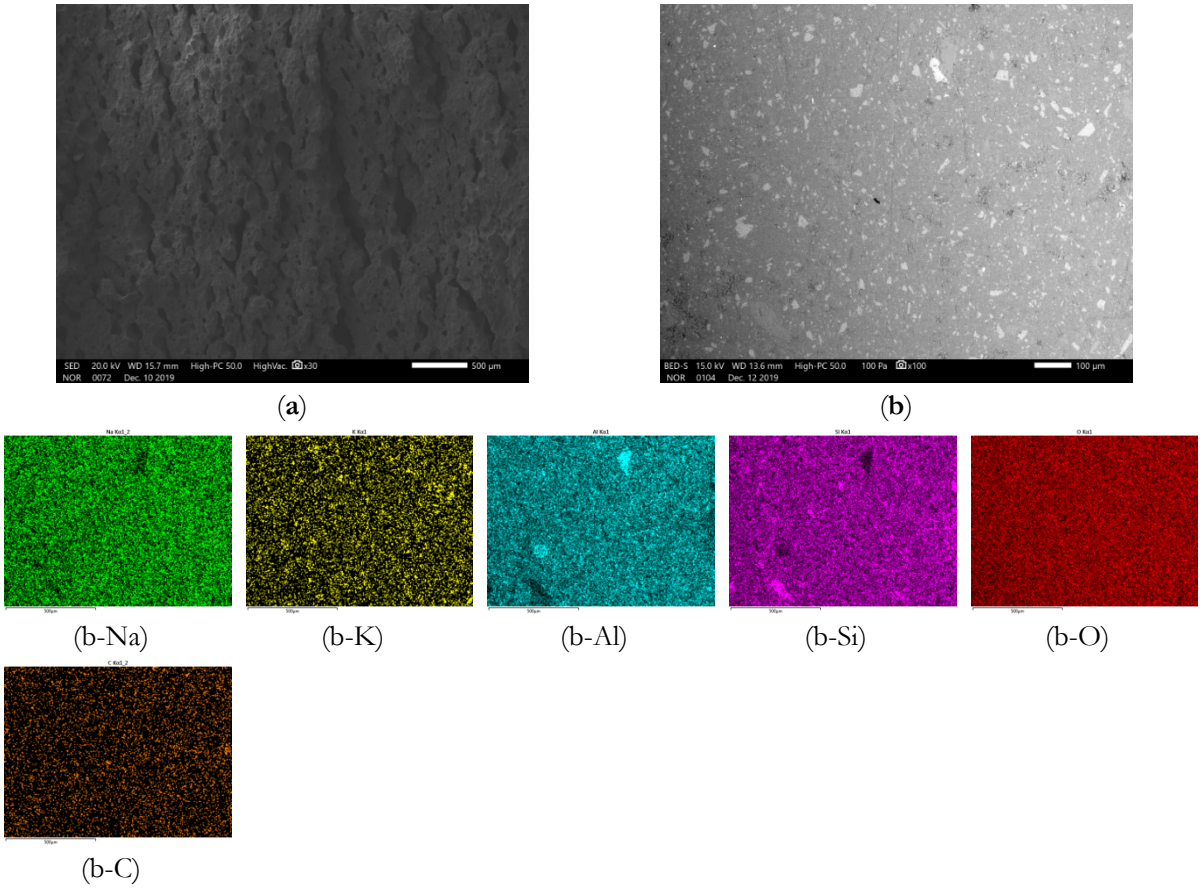

Figure 15: SEM micrograph of homogenized alkali-activated WGC with magnification (a) 30 (intact cross-section after compressive strength test, vacuumed and sputtered with Au, observed under HV; the direction of moulding is horizontal on the SEM micrograph) and (b) 100 (cut and polished cross-section observed under LV). The EDXS mapping of micrograph (b) is presented on (b-chemical element). Source: own.

4 Conclusions

The compressive and bending strength of alkali-activated material and alkali-activated foam were higher when the slurry was homogenized in its initial stage of reaction, regardless of other parameters influencing alkali activation, i.e. precursors, alkali activators, the ratio of ingredients, curing regimes and drying procedures. The increase in compressive strength was from 30% to 75%, the increase of bending strength from 10% to more than 100%. However, the homogenization of alkali-activated foam is only possible if the foaming agent has a delayed reaction with the reagents, i.e. when we are dealing with alkali-activated delayed foam, to avoid the increase in density of the foamed product due to the loss of gasses, which should be trapped in the alkali-activated precursor when the mixture is optimally designed.

The viscosity of the slurry was lower after homogenization, or at least it became measurable. The decrease was more than 50% for alkali-activated materials, whereas for alkali-activated foams the decrease in viscosity was just noticeable on an absolute scale. The density of alkali-activated materials did not change when alkali-activated material did not bloat after exposure to high temperatures (which has a negative effect on mechanical strength, as almost solid alkali-activated material turns into solid alkali-activated "foam"), or when alkali-activated foam had a delayed start of foaming.

In summary, it can be said that homogenization itself does not affect the alkali-activated reaction, it only affects the distribution of the elements and additionally grinds larger particles, resulting in a more reactive surface and a smaller volume of reagents that must dissolve before the liquid alkali can diffuse. In this way, homogenization helps to ensure that more precursor can react with alkali, which does not have to reach reagents only with "superficial" mixing of the reagents and later by time-limited diffusion in the slurry.

Acknowledgements

Project No. C3330-17-529032 "Raziskovalci-2.0-ZAG-529032" was granted by Ministry of Education, Science and Sport of the Republic of Slovenia. The investment is co-financed by the Republic of Slovenia, Ministry of Education, Science and Sport and the European Regional Development Fund. The involvement of V. Ducman was supported by the Slovenian Research Agency Programme Group P2-0273. The involvement of K. Traven and K. König was supported by Slovenian Research Agency

with Project Grant J2 9197. The involvement of M. Češnovar is part of the ERA-MIN FLOW project which has received funding from the Ministry of education, science and sport (acronym: MIZS) under grant agreement No. C 3330-18-252010. M. Pavlin is involved by the support of WOOL2LOOP project that received funding from the European Union's Horizon 2020 research and innovation programme under grant agreement No 821000.

The Metrology Institute of the Republic of Slovenia is acknowledged for the use of XRF.

Cooperation with Termit d.d. and Mrs Alenka Sešek Pavlin from Termit d.d.is highly appreciated.

References

Ahmed, M.H., Byrne, J.A., McLaughlin, J., Ahmed, W., 2013. Study of Human Serum Albumin Adsorption and Conformational Change on DLC and Silicon Doped DLC Using XPS and FTIR Spectroscopy. Journal of Biomaterials and Nanobiotechnology 04, 194–203. https://doi.org/10.4236/jbnb.2013.42024

Bernal, S.A., Provis, J.L., 2014. Durability of Alkali-Activated Materials: Progress and Perspectives. Journal of the American Ceramic Society 97, 997–1008. https://doi.org/10.1111/jace.12831

Češnovar, Traven, Horvat, Ducman, 2019. The Potential of Ladle Slag and Electric Arc Furnace Slag use in Synthesizing Alkali Activated Materials; the Influence of Curing on Mechanical Properties. Materials 12, 1173. https://doi.org/10.3390/ma12071173

Criado, M., Palomo, A., Fernández-Jiménez, A., Banfill, P.F.G., 2009. Alkali activated fly ash: effect of admixtures on paste rheology. Rheologica Acta 48, 447–455. https://doi.org/10.1007/s00397-008-0345-5

Duxson, P., Provis, J.L., Lukey, G.C., Mallicoat, S.W., Kriven, W.M., van Deventer, J.S.J., 2005. Understanding the relationship between geopolymer composition, microstructure and mechanical properties. Colloids and Surfaces A: Physicochemical and Engineering Aspects 269, 47–58. https://doi.org/10.1016/j.colsurfa.2005.06.060

Hajimohammadi, A., Ngo, T., Mendis, P., Sanjayan, J., 2017. Regulating the chemical foaming reaction to control the porosity of geopolymer foams. Materials & Design 120, 255–265. https://doi.org/10.1016/j.matdes.2017.02.026

Horvat, B., Češnovar, M., Pavlin, A., Ducman, V., 2018. Upcycling with alkali activation technology, in: Technologies & Business Models for Circular Economy. Presented at the 1st International Conference on Technologies & Business Models for Circular Economy, Univerzitetna založba Univerze v Mariboru / University of Maribor Press, pp. 261–272. https://doi.org/10.18690/978-961-286-211-4.22

Horvat, B., Ducman, V., 2019. Potential of Green Ceramics Waste for Alkali Activated Foams 30.

Hunger, M., Brouwers, H.J.H., 2009. Flow analysis of water–powder mixtures: Application to specific surface area and shape factor. Cement and Concrete Composites 31, 39–59. https://doi.org/10.1016/j.cemconcomp.2008.09.010

Juenger, M.C.G., Winnefeld, F., Provis, J.L., Ideker, J.H., 2011. Advances in alternative cementitious binders. Cement and Concrete Research 41, 1232–1243. https://doi.org/10.1016/j.cemconres.2010.11.012

Korat, L., Ducman, V., 2017. The influence of the stabilizing agent SDS on porosity development in alkali-activated fly-ash based foams. Cement and Concrete Composites 80, 168–174. https://doi.org/10.1016/j.cemconcomp.2017.03.010

Kramar, S., Šajna, A., Ducman, V., 2016. Assessment of alkali activated mortars based on different precursors with regard to their suitability for concrete repair. Construction and Building Materials 124, 937–944. https://doi.org/10.1016/j.conbuildmat.2016.08.018

Kutchko, B., Kim, A., 2006. Fly ash characterization by SEM–EDS. Fuel 85, 2537–2544. https://doi.org/10.1016/j.fuel.2006.05.016

Nematollahi, B., Ranade, R., Sanjayan, J., Ramakrishnan, S., 2017. Thermal and mechanical properties of sustainable lightweight strain hardening geopolymer composites. Archives of Civil and Mechanical Engineering 17, 55–64. https://doi.org/10.1016/j.acme.2016.08.002

Provis, J.L., Arbi, K., Bernal, S.A., Bondar, D., Buchwald, A., Castel, A., Chithiraputhiran, S., Cyr, M., Dehghan, A., Dombrowski-Daube, K., Dubey, A., Ducman, V., Gluth, G.J.G., Nanukuttan, S., Peterson, K., Puertas, F., van Riessen, A., Torres-Carrasco, M., Ye, G., Zuo, Y., 2019. RILEM TC 247-DTA round robin test: mix design and reproducibility of compressive strength of alkali-activated concretes. Materials and Structures 52. https://doi.org/10.1617/s11527-019-1396-z

Provis, J.L., Duxson, P., van Deventer, J.S.J., 2010. The role of particle technology in developing sustainable construction materials. Advanced Powder Technology 21, 2–7. https://doi.org/10.1016/j.apt.2009.10.006

Rajamma, R., Labrincha, J.A., Ferreira, V.M., 2012. Alkali activation of biomass fly ash–metakaolin blends. Fuel 98, 265–271. https://doi.org/10.1016/j.fuel.2012.04.006

Samson, G., Cyr, M., Gao, X.X., 2017. Thermomechanical performance of blended metakaolin-GGBS alkali-activated foam concrete. Construction and Building Materials 157, 982–993. https://doi.org/10.1016/j.conbuildmat.2017.09.146

Schlesinger, W.H., 1991. Biogeochemistry: an analysis of global change. Academic Press, San Diego.

Traven, K., Češnovar, M., Ducman, V., 2019. Particle size manipulation as an influential parameter in the development of mechanical properties in electric arc furnace slag-based AAM. Ceramics International. https://doi.org/10.1016/j.ceramint.2019.07.296

Traven, K., Črešnovar, M., Škapin, S., Ducman, V., 2020. Evaluation of Fly Ash-based Alkali Activated Foams at Room and Elevated Temperatures, in: 2nd International Conference on : Technologies & Business Models for Circular Economy: Conference Proceedings. Presented at the International Conference on Technologies & Business Models for Circular Economy, University of Maribor, University Press, pp. 23–34. https://doi.org/10.18690/978-961-286-353-1.2

Van Deventer, J.S.J., Provis, J.L., Duxson, P., 2012. Technical and commercial progress in the adoption of geopolymer cement. Minerals Engineering 29, 89–104. https://doi.org/10.1016/j.mineng.2011.09.009

Vlček, J., Drongová, L., Topinková, M., Matějka, V., Kukutschová, J., Vavro, M., Tomková, V., 2014. Identification of phase composition of binders from alkali-activated mixtures of granulated blast furnace slag and fly ash 10.

DESIGN OF GEOTHERMAL ENERGY PILE

PRIMOŽ JELUŠIČ, STOJAN KRAVANJA, TOMAŽ ŽULA

University of Maribor, Faculty of Civil Engineering, Transportation Engineering and Architecture, Maribor, Slovenia
primoz.jelusic@um.si, stojan.kravanja@um.si, tomaz.zula@um.si

Abstract Sustainable buildings should include energy foundations that exchanges heat energy with the ground. High-rise buildings are often founded on piles because of the large mass of the high-rise building. The article presents the design of an economically efficient geothermal energy pile. Geothermal energy piles are typical geostructures used for heating/cooling buildings. Geothermal energy piles are exposed to cyclical thermal loads and not only to structural loads like conventional piles. These cyclical loads could increase the settlement of piles, especially if they are installed in fine-grained soil. Today, it is necessary to design geotechnical structures in such a way that they are economically efficient and have a low probability of failure. The proposed optimization method is illustrated by applying it to a multi-story building supported by geothermal energy piles. The example presented shows that the load-bearing capacity is fully exploited in the optimal design solution.

Keywords: geothermal energy piles, energy foundations, optimal design, fine-grained soils, high-rise buildings

University of Maribor Press

DOI https://doi.org/10.18690/um.fkkt.2.2022.3
ISBN 978-961-286-598-6

1 Introduction

Sustainable buildings should also include energy foundations that exchanges heat energy with the ground. High-rise buildings are often founded on piles because of the large mass of the building. Piles are also used when the magnitude of the load under different parts of the building is uneven, when the construction of a shallow foundation could damage existing, adjacent buildings, and when the building is not rigid enough and large settlement differences could occur. However, load-bearing piles can also be used to exchange heat energy with the ground. Such piles are called geothermal energy piles or thermal piles. Geothermal energy piles consist of sealed pipe loops that are inserted into the pile and filled with thermal transfer fluid. The thermal fluid, which circulates through a closed loop system, generally contains antifreeze and biocide. When designing geothermal piles, it must be ensured that the soil conditions are suitable to withstand the structural pile loads and that the thermal effect is taken into account. Therefore, the thermal properties of the soil, the average undisturbed soil temperature, the average ambient air temperatures and the geothermal heat flux must be estimated. The most important additional considerations for the design of geothermal piles are the reduction of soil strength properties, radial and axial expansion, thermally induced axial stresses and the cyclical effect of thermal stresses. This paper presents the design of economically efficient geothermal energy piles, which are built in fine-grained soils such as clay and silt. Coarse-grained soils such as gravel and sand are less prone to soil shear strength reduction than fine-grained soils. In order to obtain an economically efficient design of geothermal energy piles, the optimization method was applied (Žula & Kravanja, 2018; Žula & Kravanja, 2020).

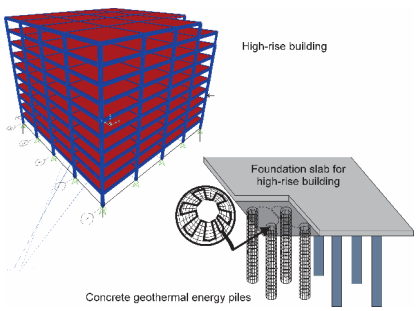

Figure 1: Geothermal energy piles for high-rise building.
Source:

2 Geothermal energy pile design model

2.1 Costs based objective function

The most suitable technology for the construction of geothermal piles is the bored pile technology. The objective function COST (EUR) is based on the self-production costs of the geothermal pile produced with the drilling technology (see Eq. (1)):

$$\text{min: } COST = C_{drill} + C_{conc} + C_{rein,main} + C_{rein,shear} + C_{thermal} \tag{1}$$

where C_{drill} stands for the cost of ground drilling, C_{conc} for the cost of the concrete used for the pile, $C_{rein,main}$ for the main reinforcing steel embedded in the concrete pile, $C_{rein,shear}$ for the shear reinforcing steel and the $C_{thermal}$ for the cost of the closed pipe loop embedded in the pile.

2.2 Geotechnical constrains

Piles for geothermal energy must be able to bear the applied structural load (Jelušič and Žlender, 2020). This load transfer of the structural load to the ground takes place through friction between the ground and the surface of the pile and by end bearing. Five boundary conditions (see Eqs. (2) - (6)) according to the Eurocode standards and recommendations GSHP (GSHP, 2012) ensure the appropriate dimensions of the geothermal piles. The constraints are defined by Eqs. (2) – (6)):

$$F_d \leq R_{c,d} \tag{2}$$

$$u_{load} + u_{thermal} \leq u_{lim} \tag{3}$$

$$A_{main,req} \leq A_{main,prov} \tag{4}$$

$$A_{main,prov} \geq A_{main,min} \tag{5}$$

$$s_{shear} \leq s_{shear,max} \tag{6}$$

where F_d (kN) is the design's vertical-load, $R_{c,d}$ (kN) is the calculated pile design resistance of the bored reinforced concrete pile, u_{load} (mm) is the settlement caused by the structural load, $u_{thermal}$ (mm) is the settlement caused by thermal effects, u_{lim} (mm) is the allowable settlement of the pile, $A_{main,req}$ (mm^2) is the required main

reinforcement steel area in the pile, $A_{main,prov}$ (mm²) is the provided main reinforcement steel area in the critical cross section of the pile, $A_{main,min}$ (mm²) is the required minimum steel area, s_{shear} (mm) is the link-spacing of shear reinforcement and the $s_{shear,max}$ (mm) is maximum spacing of the shear reinforcement. In order to fulfil all the boundary conditions defined above simultaneously and to achieve the minimum self-production costs of the geothermal energy pile, the optimization method was applied (Kravanja & Grossmann, 1994). In the optimization model, the diameter of the pile D (mm), the length of the pile L (m), the diameter of the main reinforcement bars $\emptyset_{main}$ (mm), the number of main reinforcement bars n_{main} (-), the diameter of the links $\emptyset_{shear}$ (mm) and the distance between the links s_{shear} (mm) were defined as variables. Assuming that the pile head is free, cooling of the pile leads to additional settlement, while heating causes the pile head to move upwards. Repeated cycles of the thermal effects lead to a deterioration of the shaft friction along the pile with an accumulation of settlements. The additional settlement from the thermal effects $u_{thermal}$ (mm) has been calculated based on the diagram contained in GSHP [16], see Figure 2. The discrete alternatives for each variable are shown in Table 1.

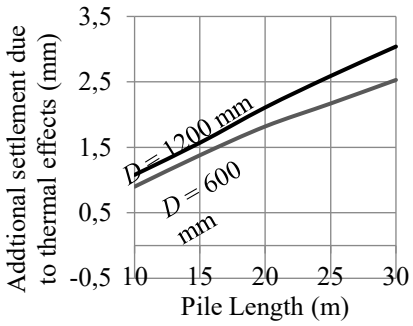

Figure 2: Additional settlement due to the repeated cycling of the thermal effects.
Source:

Table 1: Discrete alternatives of the variables.

Variable	Discrete alternatives
D (m)	0.60, 0.70, 0.80, 0.90, 1.00, 1.10, 1.20, 1.30, 1.40, 1.50
L (m)	10, 11, 12, 13, 14, 15, 16, 17, 18, 19, 20, 21, 22, 23, 24, 25, 26, 27, 28, 29, 30
$\emptyset_{main}$ (mm)	10, 12, 14, 16, 18, 20, 25, 28, 30
n_{main} (-)	6, 8, 10, 12, 14, 16, 18, 20, 22, 24, 26, 28, 30, 32, 34, 36, 38, 40
$\emptyset_{shear}$ (mm)	8, 10, 12, 14
s_{shear} (mm)	100, 125, 150, 175, 200, 225, 250

3 Results

The optimization model presented in this article is used to determine the cheapest possible geothermal energy pile and to find an optimal design with the given design parameters. The ground consists of low plasticity clay (CL) at a depth of 0 m to 30 m below ground level. The pile is loaded with a vertical design load F_d = 1481.8 kN. The design data are composed of the undrained shear strength (c_u = 60+5.5·z, z is the depth below the top of the pile), the drained modulus of elasticity (E_{so} = 300·cu kPa) and the adhesion factor (α_{sk} = 0.5 and α_{bk} = 1.0). The linear increase of the undrained shear strength cu with depth is shown in Figure 3. The geometry and all necessary input data for the optimal pile design are shown in Table 2. The results show that the optimal geothermal energy pile for the given design parameters leads to production costs of about 1952 €.

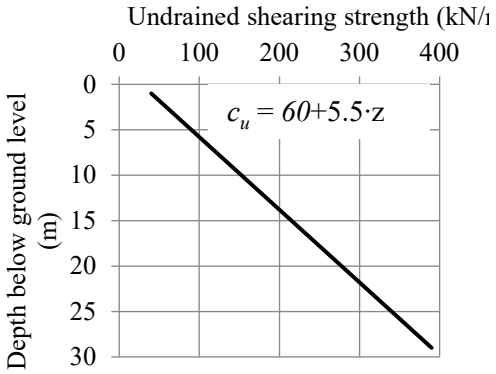

Figure 3: Undrained shearing strength of low plasticity clay (CL).
Source:

Table 2: Optimal design of geothermal energy pile.

Parameter	Value of parameter
D (mm)	800
L (m)	13
$Ø_{main}$ (mm)	14
n_{main} (-)	14
$Ø_{shear}$ (mm)	8
s_{shear} (mm)	150
$F_d < R_{cd}$ (kN)	1481.8 < 1514.4 (98%)
$u < u_{lim}$ (mm)	7.5 < 10 (75%)

Parameter	Value of parameter
$A_{main,req} < A_{main,prov}$ (mm²)	0 < 2155
$A_{main,min} < A_{main,prov}$ (mm²)	2011 < 2155 (93%)
$s_{shear} < s_{shear,max}$ (mm)	150 < 168 (89%)
COST (€)	1952

4 Conclusion

The article presents the cost optimization of a geothermal energy pile. The optimization model integrates the cost objective function of the drilled geothermal energy concrete pile and the geotechnical constraints that ensured the requirements of the Eurocode specifications and GSHP recommendations. The bearing capacity of the pile and its settlement under the applied load are the most important factors in verifying the pile design. The choice of the design method for pile foundations depends on the type of pile and the installation method. A pile design based on structural optimization is much more efficient than a design based on classical structural analysis, because the optimization allows to fully utilize the materials and geometries without resistance reserves. The example presented shows that the load-bearing capacity of the pile is fully exploited.

Acknowledgments

This work was supported by the National Research Programmes of Slovenia P2-0268 and P2-0129.

References

GSHP Association (2012). Thermal pile design, installation and materials standards, Gr. Source Heat Pump Assoc. Milt. Keynes. 82.

Jelušič, P., Žlender, B. (2020). Determining optimal designs for conventional and geothermal energy piles. *Renew. Energy*, *147*, 2633–2642, doi:10.1016/j.renene.2018.08.016.

Kravanja, Z., Grossmann, I. E.(1994). New developments and capabilities in prosyn—An automated topology and parameter process synthesizer. *Comput. Chem. Eng.* 1*8*, 1097–1114, doi:10.1016/S0098-1354(94)85027-5.

Žula, T., Kravanja, S. (2018). Optimization of the sustainability profit generated by the production of beams. In Proceedings of the Technologies & Business Models for Circular Economy; Univerzitetna založba Univerze v Mariboru / University of Maribor Press, pp. 159–165.

Žula, T., Kravanja, S. (2020). Sustainability Profit Generated by the Optimization of Continuous Beams. In Proceedings of the 2nd International Conference on : Technologies & Business Models for Circular Economy: Conference Proceedings; University of Maribor, University Press, pp. 133–140.

USE OF RECYCLED PLASTIC WASTE IN CONCRETE

GREGOR KRAVANJA[1, 2]

[1] University of Maribor, Faculty of Civil Engineering, Transportation Engineering and Architecture, Maribor, Slovenia
gregor.kravanja@um.si
[2] University of Maribor, Faculty of Chemistry and Chemical Engineering, Maribor, Slovenia
gregor.kravanja@um.si

Abstract Substantial growth in plastics consumption over the last decades has contributed to an increasing amount of plastic waste being deposited in landfills and in natural environments such as the oceans. The production of new materials from recycled plastics appears to be one of the best solutions for the management of plastic waste. The aim of this paper is to investigate the adequacy of using various recycled plastic waste in concrete. The effects of waste plastic aggregates or fibers on the physical, mechanical, thermal and durability properties of concrete have been investigated. In addition, several recommendations for future studies are provided.

Keywords: recycling plastic, concrete, physical properties, mechanical properties, durability

University of Maribor Press

DOI https://doi.org/10.18690/um.fkkt.2.2022.4
ISBN 978-961-286-598-6

1 Introduction

The world is on the edge of a global plastic calamity and our collective action over the next decade will determine the future of our planet. If current trends in production and waste management continue, around 12,000 million tonnes of plastic waste will end up in landfills or in natural environments such as the oceans by 2050 (Geyer et al., 2017). The UN Environment Programme estimated that for every square mile of ocean, there are 46,000 pieces of floating plastic (Silverman, 2007). The production of new materials by recycling plastic waste seems to be one of the best solutions for the disposal of plastic waste.

Concrete is the most widely used material and is available at low cost. The main raw materials consist of cement, water, and aggregates. Approximately 65-80% of the concrete volume is taken up by aggregates, which strongly influence the general workability, durability, permeability, and strength of concrete. The use of recycled plastics as fine aggregates can eliminate large amounts of waste material while solving problems associated with aggregate mining, waste disposal and lack of aggregates on construction sites (Almeshal et al., 2020). The use of a lightweight plastic aggregate as an alternative to natural aggregates usually reduces the weight of concrete and offers many advantages, such as lower costs, enhanced thermal insulation performance and better handling. Overall, the use of waste material in concrete production is considered to be environmentally and economically beneficial (Faraj et al., 2020).

The aim of this paper is to investigate the appropriateness of using recycled plastics in concrete mixes. The influence of the commonly used recycled plastic aggregates or fibers on the physical, mechanical, thermal and durability properties of concrete has been extensively investigated. Furthermore, several recommendations for future studies are provided.

2 Different types of waste polymers in concrete

Generally, plastic is incorporated into concrete in the form of plastic aggregates as an alternative to natural aggregates or as a fiber that is intended to reinforce the concrete. The most commonly used recycled plastics in concrete are (PP) plastic particles (Faraj et al., 2019), PP fibers (Madhavi et al., 2014), high-density

polyethylene (HDPE) particles (Badache et al., 2018), polyvinyl chloride (PVC) pipe (Gupta, 2013), polyethylene terephthalate (PET) plastics fibers, particles and bags PET (Sulyman et al., 2016), expanded polystyrene (EPS) foams (Dissanayake et al., 2017), high impact polystyrene (PHIS) granules (Olofinnade et al., 2020), high toughness poly-propylene (PPHT) fibers (Ikai et al., 2010), polyethylene (PE) granules (Chen et al., 2019), and shredded recycled plastic waste (Jain et al., 2020). The properties of the most commonly used plastic waste polymers in concrete, such as tensile strength (σ), modulus of elasticity (E) and thermal conductivity (λ), are shown in Table 1. All types of plastic waste have much lower young moduli and thermal conductivities than those of concrete mixes.

Table 1: Properties of commonly used waste plastic polymers in concrete materials (Jacob-Vaillancourt and Sorelli, 2018).

Material	σ/MPa	E/GPa	λ /(W/m.K)
PET	55–80	2.1–3.1	0.15
PVC	50–60	2.7–3.0	0.17–0.21
PS	30–55	3.1–3.3	0.105
PP	25–40	1.3–1.8	0.12
PE	18–30	0.6–1.4	0.33–0.52
Natural aggregate	/	70	2.29–2.78
Cement*	/	36–40	1

*cement paste with w/c = 0.5

3 Properties of concrete containing plastic waste

The effects of the addition of plastics on the properties of concrete in the green state, the mechanical properties in the cured state, durability and thermal properties are discussed in this section.

3.1 Physical properties

Workability, which determines the concrete homogeneity, is the most important property of concrete in the green state. The slump test is normally applied to the measured workability. The addition of waste material can greatly influence workability. (Guendouz et al., 2016). Increasing the substitution level of fine plastic aggregates decreases slump and consequently the workability of concrete (Batayneh et al., 2007). In order to prevent poor mixture consistency and to increase workability, the use of superplasticizers is therefore recommended (Faroug et al.,

1999). The incorporation of plastic waste reduces the density of the concrete. The use of lightweight plastic paving concrete has many advantages. For example, the risk of earthquakes is greatly reduced because the force of earthquake depends linearly on dead building weight (Akçaözoğlu et al., 2010).

3.2 Mechanical properties

Compressive and flexural strength are the most important properties that verify the behavior of concrete (Fig. 1) Among them, splitting tensile strength, pulse velocity, triaxial strength and elastic modules are frequently investigated.

The quality of concrete depends on the compressive strength. The results of the 28-day compressive strength of concrete with plastic waste are shown in Fig. 2. An increase in the volume fraction of plastics by up to 40% reduced the compressive strength (Fig. 2a). However, the addition of a limited amount of plastic to the concrete can lead to small improvements in mechanical properties (Fig. 2b). Similarly, the flexural strength of concrete, which was evaluated by the three-point loading of the four-point loading test, decreased with increasing the volume fraction of plastics. The addition of a small percentage of plastics can improve the ability to resist failure in bending (Fig. 3b).

The factors that can negatively affect the compressive and flexural strength of concrete containing plastic waste are: hydrophobic nature of the plastics, which can cause a cement hydration reaction, low strength between the cement paste and the surface of plastic waste aggregates, high porosity, reduced modulus of elasticity and deterioration of the plastic aggregates (Gu and Ozbakkaloglu, 2016).

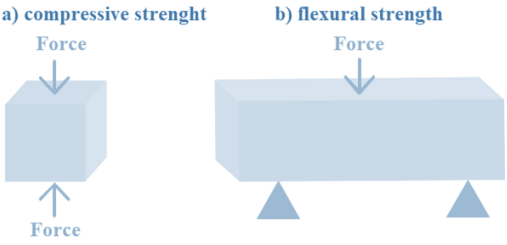

Figure 1: Compressive and flexural strength are influenced to a great extent by the addition/replacement of various forms of plastics.

Source: own.

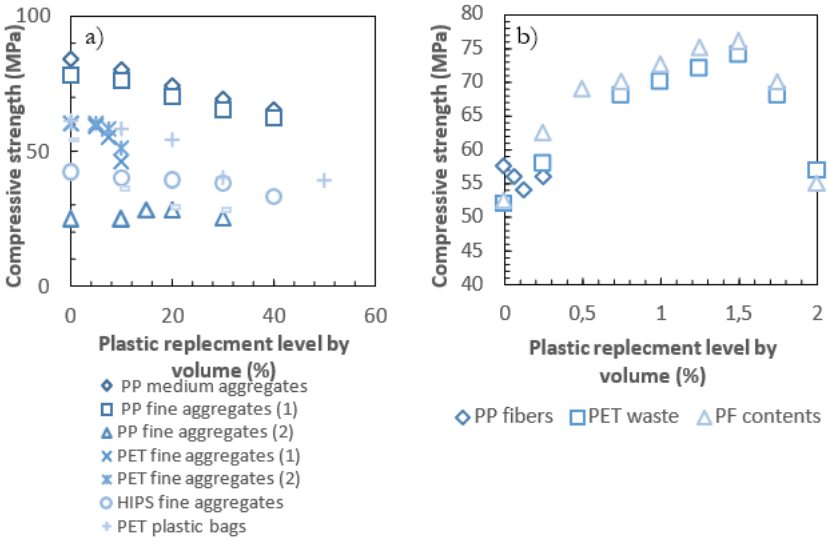

Figure 2: Variation of compressive strength of concrete with varying plastic content: PP medium aggregates (Faraj et al., 2019), PP fine aggregates 1 and 2 (Yang et al., 2015), PET fine aggregates 1 end 2 (Hama and Hilal, 2017), HIPS fine aggregates(Chunchu and Putta, 2019), PET plastic bags (Safi et al., 2013), PP fibers (Aslani et al., 2019), PET waste and PF contents (Al-Hadithi and Hilal, 2016).

Source: own.

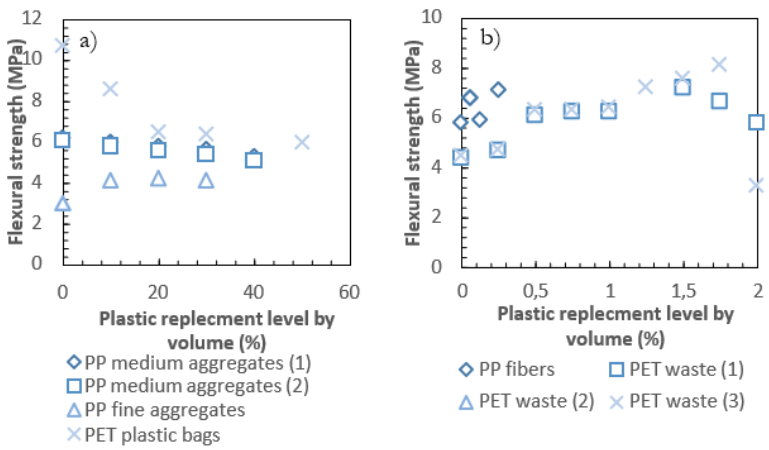

Figure 3: Variation of flexural strength of concrete with different plastic content:: PP medium aggregates 1 and 2 (Faraj et al., 2019), PP fine aggregates (Yang et al., 2015), PET plastic bags (Safi et al., 2013), PP fibers (Aslani et al., 2019), PET waste 1, 2, 3 (Gesoglu et al., 2017).

Source: own.

3.3 Durability

The durability performance of concrete is usually assessed on the basis of water absorption properties, air and water permeability, chloride migration, carbonization, shrinkage, and freezing/thawing resistance.

Water absorption increases as the exchange ratio of sand to plastic waste aggregates increases (Coppola et al., 2018). This indicates that mixing natural aggregates and plastics leads to more porous concrete. The water and air permeability increases with the content of plastic waste in the concrete. More voids in the concrete matrix lead to greater chloride ion penetration and higher carbonation of the cement-like composite (Silva et al., 2013). During the carbonization process, calcium hydroxide $Ca(OH)_2$ reacts with carbon dioxide (CO_2) from the atmosphere and has a negative effect on the mechanics of concrete.

In case of shrinkage, plastic waste has a higher drying shrinkage compared to conventional concrete. In general, the shrinkage stress of plastic-containing cement paste decreases (Bendimerad et al., 2016). The freeze and thawing resistance of concrete containing waste plastics meets all the standards for safe usage. In some cases, increasing plastic waste content in concrete even enhance frost resistance and durability (Kan and Demirboğa, 2009).

3.4 Fire resistance and thermal properties

Fire resistance is an important property of concrete that ensures general building safety. The fire resistance of concrete is characterized by the cement paste and the aggregate. When exposed to fire, concrete heats up 50 times slower than steel. However, replacing natural aggregates with waste plastic aggregates can create holes in the concrete at 400 °C to 600 °C, which reduce its flexural strength and produce toxic smoke (Sayadi et al., 2016). The thermal conductivity of concrete containing plastic waste decreased considerably. The recycling of plastics in concrete leads to improved thermal insulation properties and higher energy efficiency of buildings (Dweik et al., 2008).

4 Conclusions

Plastics can easily be used in concrete in certain proportions. The following conclusions are:

- the workability of concrete containing recycled plastic is reduced. To increase the workability of concrete in the green phase, superplasticizers should be used,
- the inclusion of plastic in concrete does not effectively improve the mechanical properties of concrete. The strength of concrete should be balanced with reactive materials such as silica fume, metakaolin and iron slag to create an additional pozzolanic reaction,
- the durability of concrete containing plastic waste is severely impaired. Water absorption increases as the exchange ratio of sand to plastic waste aggregates increases,
- More voids in the concrete matrix leads to more chloride ion penetration and higher carbonation,
- replacing natural aggregates with plastic waste aggregates can create holes in concrete at 400 °C to 600 °C, which impairs the bending strength,
- freeze and thawing resistance of concrete containing waste plastics meets all the standards for safe usage.

In order to make concrete containing recycled waste more attractive and better accepted by the construction industry, future studies should focus on economic efficiency, social acceptance, material properties such as adhesion, triaxial failure, abrasion and impact resistance, rheological properties, thixotropy, durability properties such as sulfate resistance and general long-term resistance to environmental exposure. The outcomes of this paper show that the use of recyclable plastics in concrete leads to more sustainable building materials in the construction industry.

Acknowledgments

I would like to acknowledge the Slovenian Research Agency (ARRS) for financing research in the frame of Programme P2-0046 (Separation processes and production design).

References

Akçaözoğlu, S., Atiş, C.D., Akçaözoğlu, K., 2010. An investigation on the use of shredded waste PET bottles as aggregate in lightweight concrete. Waste management 30(2), 285-290.

Al-Hadithi, A.I., Hilal, N.N., 2016. The possibility of enhancing some properties of self-compacting concrete by adding waste plastic fibers. Journal of Building Engineering 8, 20-28.

Almeshal, I., Tayeh, B.A., Alyousef, R., Alabduljabbar, H., Mohamed, A.M., Alaskar, A., 2020. Use of recycled plastic as fine aggregate in cementitious composites: A review. Construction and Building Materials 253, 119146.

Aslani, F., Liu, Y., Wang, Y., 2019. The effect of NiTi shape memory alloy, polypropylene and steel fibres on the fresh and mechanical properties of self-compacting concrete. Construction and Building Materials 215, 644-659.

Badache, A., Benosman, A.S., Senhadji, Y., Mouli, M., 2018. Thermo-physical and mechanical characteristics of sand-based lightweight composite mortars with recycled high-density polyethylene (HDPE). Construction and Building Materials 163, 40-52.

Batayneh, M., Marie, I., Asi, I., 2007. Use of selected waste materials in concrete mixes. Waste management 27(12), 1870-1876.

Bendimerad, A.Z., Rozière, E., Loukili, A., 2016. Plastic shrinkage and cracking risk of recycled aggregates concrete. Construction and Building Materials 121, 733-745.

Chen, Y., Xu, L., Xuan, W., Zhou, Z., 2019. Experimental study on four-point cyclic bending behaviours of concrete with high density polyethylene granules. Construction and Building Materials 201, 691-701.

Chunchu, B.R.K., Putta, J., 2019. Rheological and strength behavior of binary blended SCC replacing partial fine aggregate with plastic E-waste as high impact polystyrene. Buildings 9(2), 50.

Coppola, B., Courard, L., Michel, F., Incarnato, L., Scarfato, P., Di Maio, L., 2018. Hygro-thermal and durability properties of a lightweight mortar made with foamed plastic waste aggregates. Construction and Building Materials 170, 200-206.

Dissanayake, D., Jayasinghe, C., Jayasinghe, M., 2017. A comparative embodied energy analysis of a house with recycled expanded polystyrene (EPS) based foam concrete wall panels. Energy and Buildings 135, 85-94.

Dweik, H.S., Ziara, M.M., Hadidoun, M.S., 2008. Enhancing concrete strength and thermal insulation using thermoset plastic waste. International Journal of Polymeric Materials 57(7), 635-656.

Faraj, R.H., Ali, H.F.H., Sherwani, A.F.H., Hassan, B.R., Karim, H., 2020. Use of recycled plastic in self-compacting concrete: A comprehensive review on fresh and mechanical properties. Journal of Building Engineering, 101283.

Faraj, R.H., Sherwani, A.F.H., Daraei, A., 2019. Mechanical, fracture and durability properties of self-compacting high strength concrete containing recycled polypropylene plastic particles. Journal of Building Engineering 25, 100808.

Faroug, F., Szwabowski, J., Wild, S., 1999. Influence of superplasticizers on workability of concrete. Journal of materials in civil engineering 11(2), 151-157.

Gesoglu, M., Güneyisi, E., Hansu, O., Etli, S., Alhassan, M., 2017. Mechanical and fracture characteristics of self-compacting concretes containing different percentage of plastic waste powder. Construction and Building Materials 140, 562-569.

Geyer, R., Jambeck, J.R., Law, K.L., 2017. Production, use, and fate of all plastics ever made. Science advances 3(7), e1700782.

Gu, L., Ozbakkaloglu, T., 2016. Use of recycled plastics in concrete: A critical review. Waste Management 51, 19-42.

Guendouz, M., Debieb, F., Boukendakdji, O., Kadri, E., Bentchikou, M., Soualhi, H., 2016. Use of plastic waste in sand concrete. J. Mater. Environ. Sci 7(2), 382-389.

Gupta, P.K., 2013. Confinement of concrete columns with unplasticized Poly-vinyl chloride tubes. International Journal of Advanced Structural Engineering 5(1), 19.

Hama, S.M., Hilal, N.N., 2017. Fresh properties of self-compacting concrete with plastic waste as partial replacement of sand. International Journal of Sustainable Built Environment 6(2), 299-308.

Ikai, S., Reichert, J., Rodrigues, A., Zampieri, V., 2010. Asbestos-free technology with new high toughness polypropylene (PP) fibers in air-cured Hatschek process. Construction and building materials 24(2), 171-180.

Jain, A., Siddique, S., Gupta, T., Sharma, R.K., Chaudhary, S., 2020. Utilization of shredded waste plastic bags to improve impact and abrasion resistance of concrete. Environment, Development and Sustainability 22(1), 337-362.

Kan, A., Demirboğa, R., 2009. A new technique of processing for waste-expanded polystyrene foams as aggregates. Journal of materials processing technology 209(6), 2994-3000.

Madhavi, T.C., Raju, L.S., Mathur, D., 2014. Polypropylene fiber reinforced concrete-a review. International journal of emerging technology and advanced engineering 4(4), 114-119.

Olofinnade, O., Chandra, S., Chakraborty, P., 2020. Recycling of high impact polystyrene and low-density polyethylene plastic wastes in lightweight based concrete for sustainable construction. Materials Today: Proceedings.

Safi, B., Saidi, M., Aboutaleb, D., Maallem, M., 2013. The use of plastic waste as fine aggregate in the self-compacting mortars: Effect on physical and mechanical properties. Construction and Building Materials 43, 436-442.

Sayadi, A.A., Tapia, J.V., Neitzert, T.R., Clifton, G.C., 2016. Effects of expanded polystyrene (EPS) particles on fire resistance, thermal conductivity and compressive strength of foamed concrete. Construction and building materials 112, 716-724.

Silva, R.V., de Brito, J., Saikia, N., 2013. Influence of curing conditions on the durability-related performance of concrete made with selected plastic waste aggregates. Cement and Concrete Composites 35(1), 23-31.

Silverman, J., 2007. Why is the world's biggest landfill in the Pacific Ocean? Retrieved from Web site, How Stuff Works on September 19, 2007.

Sulyman, M., Haponiuk, J., Formela, K., 2016. Utilization of recycled polyethylene terephthalate (PET) in engineering materials: a review. International Journal of Environmental Science and Development 7(2), 100.

Yang, S., Yue, X., Liu, X., Tong, Y., 2015. Properties of self-compacting lightweight concrete containing recycled plastic particles. Construction and Building Materials 84, 444-453.

TOPOLOGY OPTIMIZATION OF STEEL-LINED ROCK CAVERNS FOR UNDERGROUND STORAGE OF CHEMICAL ENERGY

STOJAN KRAVANJA,[1] PRIMOŽ JELUŠIČ,[1] TOMAŽ ŽULA,[1]
ZDRAVKO KRAVANJA[2]

[1] University of Maribor, Faculty of Civil Engineering, Transportation Engineering and Architecture, Maribor, Slovenia
stojan.kravanja@um.si, primoz.jelusic@um.si, tomaz.zula@um.si
[2] University of Maribor, Faculty of Chemistry and Chemical Engineering, Maribor, Slovenia
zdravko.kravanja@um.si

Abstract The paper presents the topology optimization of lined rock caverns designed for underground storage of chemical energy. This type of storage can store a high amount of hydrogen, methane, natural gas, carbon dioxide or other substances. The caverns are made of concrete shells and lined with thin steel sheets to seal the content. Optimization is performed by the mixed-integer non-linear programming (MINLP) approach. The MINLP computer program GAMS/Dicopt is used. The model includes the cost objective function, which is subjected to geomechanical and design constraints. In this attempt, the topology calculation is included in the discrete optimization of the underground storage. A numerical example at the end of the paper shows the overall discrete MINLP optimization of an underground gas storage facility. The optimal discrete design with the optimal number of caverns of the storage is explicitly determined. Additional investment savings are achieved.

Keywords: underground storage, topology optimization, cost optimization, mixed-integer non-linear programming, MINLP

University of Maribor Press

DOI https://doi.org/10.18690/um.fkkt.2.2022.5
ISBN 978-961-286-598-6

1 Introduction

This paper deals with the topology optimization of lined rock caverns (LRC) designed for underground storage of chemical energy. This type of storage can store a high amount of hydrogen, methane, natural gas, carbon dioxide or other substances. The LRC caverns consist of 2 meters or more thick, cylindrically shaped concrete walls and are lined with 12-15 mm thin steel sheets. They are up to 100 m high, are built with diameters of up to 30 m or more and are bored to a depth of 300 m. Because the LRCs contain the gas under high pressure (between 3 and 30 MPa), they have to be bored into a rock with high strength (limestone, dolomite, granite, gneiss). The concrete walls of the caverns transfer the internal pressure onto the rock mass, while the steel lining seal the gas content. The surrounding rock mass carry the gas pressure, see (Sofregaz US Inc., 1999), (Brandshaug *et al.*, 2001), (Chung *et al.*, 2003) and (Glamheden & Curtis, 2006).

In the near past, some investigations have been carried out in the field of optimization of underground gas storages. For example, the optimization of a single gas cavern with non-linear programming (NLP) was introduced by (Kravanja & Žlender, 2010), the optimization of any number of caverns in the UGS was later presented by (Žlender & Kravanja, 2011), while the optimization in different rock environments was reported by (Kravanja & Žlender, 2012) and (Jelušič *et al.*, 2019). The latter reference introduced a prediction of the minimal investment costs using an adaptive network based fuzzy inference system (ANFIS) for the UGSs with capacities from 10 to 100 million m^3 of natural gas. The optimization of the discrete dimensions of the caverns was performed by (Kravanja & Žula, 2018) using mixed-integer non-linear programming (MINLP).

Underground gas storage facilities (UGS) are usually constructed from one to four LRCs. The correct determination of the number of LRCs built is very important as it has a strong impact on the investment costs. Therefore, we perform the topology optimization of the UGS with the calculation of the optimal number of LRCs. The topology logical constraints are inserted into the optimization model. In this way, the optimal discrete design of the storage facility with the optimal number of caverns is explicitly determined.

2 MINLP problem formulation

The optimization problem of the lined rock cavern is non-linear, continuous and discrete. Mixed-integer non-linear programming (MINLP) is thus applied. The general MINLP optimization problem is formulated as follows:

$$\begin{gathered}\min \; z=f(\mathbf{x},\mathbf{y}) \\ \text{subjected to: } \; g_k(\mathbf{x},\mathbf{y}) \le 0 \quad k \in K \\ \mathbf{x} \in X=\{\mathbf{x} \in R^n: \; \mathbf{x}^{LO} \le \mathbf{x} \le \mathbf{x}^{UP}\} \\ \mathbf{y} \in Y=\{0,1\}^m\end{gathered}$$

where **x** is a vector of continuous variables and **y** is a vector of discrete (binary 0-1) variables. The function $f(\mathbf{x}, \mathbf{y})$ is the objective function, which is subjected to the (in)equality constraints $g_k(\mathbf{x},\mathbf{y})$. At least one function must be non-linear. All functions must be continuous and differentiable.

3 MINLP optimization model

According to the above MINLP formulation, the MINLP optimization model of the UGS is being developed. The model comprises the cost objective function of the system, which is subjected to geomechanical, design and logical constraints. The model input data (constants) and variables are also defined.

While the geomechanical constraints assure sufficient strength of the surrounding rock, they also prevent the uplift of the rock above the cavern, they prevent rock collapse between caverns and they limit the large deformations of the concrete wall and steel lining. The design constraints define the relationships between the dimensions of the LRC, internal gas pressure and the rock. They also represent the upper and lower bounds of the variables. The logical constraints define the relationships between discrete (binary 0-1) variables and determine the system topology (number of caverns) and the discrete dimensions of the structure. Since the model is simple and contains only some main constraints, it is suitable for use in the preliminary design phase.

The design variables (**x**) represent the number of caverns *NOCAV*, the inner diameter of the cavern *DCAV* [m], the depth of the cavern *DEPTH* [m], the height of the cavern tube *HCAV* [m], the thickness of the concrete cavern wall *TWALL* [m] and the gas pressure *PGAS* [MPa], see Fig. 1. These variables are explicitly rounded on whole discrete values during the optimization process.

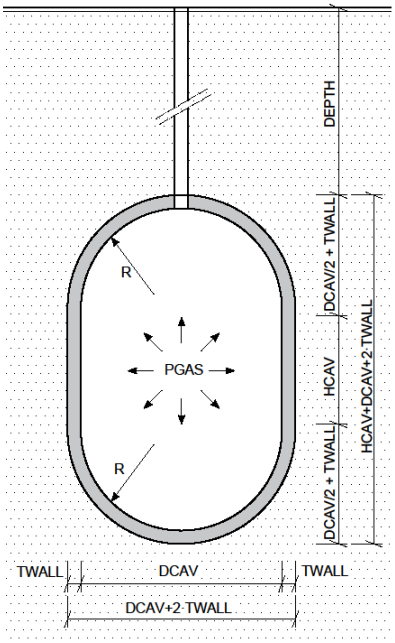

Figure 1: Vertical cross-section of lined rock cavern.
Sourece: own.

The objective function includes the investment costs of the UGS system *COSTS* [€]. It is defined by Eq. (1).

$$COSTS = FIX + f(\mathbf{x}) \cdot NOCAV \tag{1}$$

The equation defines the fixed costs *FIX* and the dimension-dependent costs $f(\mathbf{x})$ of a cavern, multiplied by the number of caverns *NOCAV*. While the fixed costs include the upper-ground and underground works, the dimension-dependent costs represent the excavation and protection of the cavern and its tunnel, as well as the costs for the drainage system, concrete, reinforcement and steel lining of the cavern.

Topology logical constraints define the objective variable *NOCAV* - the number of caverns built in a UGS facility, see Eqs. (2)-(4). The variable *NOCAV* is calculated as the sum of the binary variables y_{NOCAVi}, $i \in I$, see Eq. (3). Eq. (4) defines only one possible vector of binary variables, which is assigned for each topology (number of caverns). For example, the minimal topology with a single cavern is defined in this way by the vector of binary variables $\boldsymbol{y}_{NOCAV} = \{1,0,0,0,0,\ldots,0\}$ and not by $\boldsymbol{y}_{NOCAV} = \{0,1,0,0,0,\ldots,0\}$ or others.

$$NOCAV^{LO} \leq NOCAV \leq NOCAV^{UP} \tag{2}$$

$$NOCAV = \sum_i y_{NOCAVi} \tag{3}$$

$$y_{NOCAVi-1} \geq y_{NOCAVi} \tag{4}$$

Discrete dimensions are determined by Eqs. (5)-(7). For example, the height of the cavern tube *HCAV* is calculated as a scalar product between a vector of the discrete value alternatives $\boldsymbol{q}_{HCAV}$ and a vector of the binary variables $\boldsymbol{y}_{HCAV}$, see Eq. (6). Only one discrete value is then selected for the variable, since the sum of j, $j \in J$, binary variables is equal one, see Eq. (7). All design variables are determined in this way.

$$HCAV^{LO} \leq HCAV \leq HCAV^{UP} \tag{5}$$

$$HCAV = \sum_j q_{HCAVj} \cdot y_{HCAVj} \tag{6}$$

$$\sum_j q_{HCAVj} = 1 \tag{7}$$

4 Numerical example

The simultaneous topology, discrete dimension and cost optimization of the underground gas storage in Senovo, Slovenia, is presented. The UGS in Senovo is planned to store 22.24 million m^3 of natural gas.

Note that the primary project comprised four lined rock caverns, which were to be included in the UGS - to store 5.56 million m^3 of natural gas each. This design (with the specified number of four caverns) was optimized with MINLP by (Kravanja and Žula, 2018) and achieved the optimal result of 72.88 million EUR., see Fig. 2, which represented 47.7 % of the savings compared to the design obtained with the classical method (FEM).

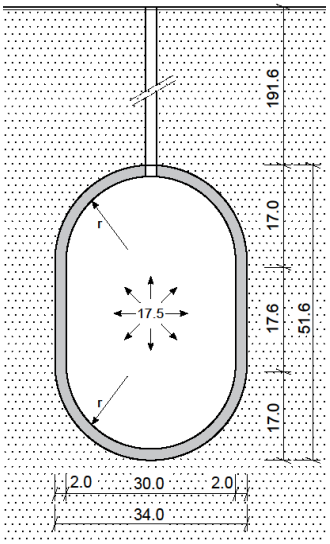

Figure 2: Optimized lined rock caverns of the UGS (Nocav = 4).
Sourece: own.

The topology, discrete dimension and cost optimization of the Senovo UGS is performed using a new MINLP optimization model, which includes topology logical constraints and some other modifications. The cost items and prices defined in the cost objective function are the same as those used in the project and in our previous optimizations, see Table 1. The model is written in GAMS, the General Algebraic Modelling System by (Brooke *et al.*, 1988). Four different topologies have been defined that determine 1, 2, 3 or 4 caverns. The LRC superstructure also includes 200 different rounded dimension alternatives for the inner diameter of the cavern, 2000 alternatives for the depth of the cavern, 2000 alternatives for the height of the cavern tube, 30 alternatives for the thickness of the concrete cavern wall and 200 discrete alternatives for the internal gas pressure. The overall combinatorics of the discrete problem is high: a total 4434 binary variables of the alternatives yield $1.92 \cdot 10^{13}$ different LRC structural alternatives. One of them is optimal.

This discrete MINLP optimization is performed with the program GAMS/DICOPT, which was developed by (Grossmann & Viswanathan, 2002). Note that comprehensive MINLP problems we usually optimize with the computer synthesizer MipSyn by (Kravanja, 2010). The optimal result represents the minimal total investment costs of the UGS of 57.62 million EUR. The optimal topology with

2 caverns is obtained. Fig. 3 shows the vertical cross-section of the optimized lined rock caverns. The figure shows the calculated "optimal" discrete variables (dimensions and the internal gas pressure). Note that this optimal result shows an additional 21 % of the net savings compared to the previous optimized design with fixed topology.

Table 1: Cost items and prices.

Cost item	Price
Upper ground works	2 982 500 EUR
Underground works	2 798 025 EUR
Price of the tunnel excavation	2 440 EUR/m[1]
Price of the tunnel protection	1 340 EUR/m[1]
Price of the cavern excavation	100 EUR/m[3]
Price of the cavern protection	90 EUR/m[2]
Price of the cavern drainage	60 EUR/m[2]
Price of the cavern wall concrete	190 EUR/m[3]
Price of the wall reinforcement	2 000 EUR/t
Price of the steel lining	920 EUR/m[2]

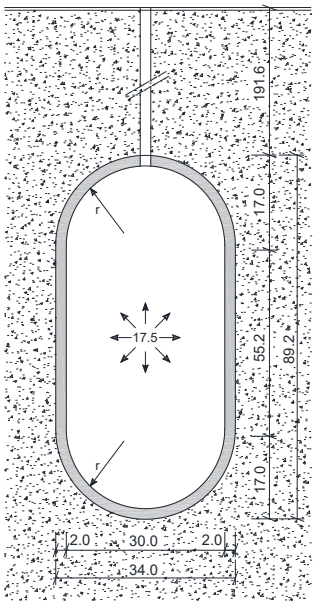

Figure 3: Optimized lined rock caverns of the UGS (Nocav = 2).
Sourece: own.

5 Conclusions

The paper discusses the simultaneous topology, discrete dimension and cost optimization of the lined rock caverns of underground storage of chemical energy. The optimization is performed by the mixed-integer non-linear programming, MINLP. The MINLP optimization model is developed into which the topology logical constraints are inserted. The numerical example at the end of the paper shows the advantages of the presented simultaneous optimization approach, tested on the case of the underground gas storage Senovo, Slovenia. A new optimal topology of two caverns is found. Significant additional investment savings are achieved. The result achieved represents the trade-off between the storage capacity and the investment costs of construction. In a future study, the operating costs of the underground storage facility, including filling and emptying of the storage, will be investigated. The proposed approach is also attractive for the optimization of underground storage facilities for hydrogen or methane.

Acknowledgments

The authors are grateful for the support of funds from the Slovenian Research Agency (research programes P2-0129, P2-0268 and P2-0032).

References

Brandshaug, T., Christianson, M., Damjanac, B. (2001).Technical review of the lined rock cavern (LRC) - concept and design methodology: mechanical response of rock mass. US Department of Energy.

Brooke, A., Kendrick, D., Meeraus, A. (1988). GAMS - A User's Guide. Scientific Press, Redwood City, CA.

Chung, I.M., Cho, W., Heo, J.H. (2003). Stochastic hydraulic safety factor for gas containment in underground storage caverns. *J Hydrol*, 284, 77-91.

Glamheden, R., Curtis, P. (2006). Excavation of a cavern for high-pressure storage of natural gas. *Tunnelling and Underground Space Technology*, 21(1), 56-67.

Grossmann, I.E., Viswanathan, J. (2002). DICOPT - Discrete and Continuous Optimizer. Engineering Design Research Center (EDRC) at Carnegie Mellon University, Pittsburgh, PA.

Jelušič, P., Kravanja, S., Žlender, B. (2019). Optimal cost and design of an underground gas storage by ANFIS, *Journal of natural gas science and engineering*, 61, 142-157. doi: 10.1016/j.jngse.2018.11.003

Kravanja, S., Žlender, B. (2010). Optimal design of underground gas storage. In: WIT Transactions on the Built Environment, 112, 389-399. doi.org/10.2495/HPSM100361

Kravanja, S., Žlender, B. (2012). Optimization of the underground gas storage in different rock environments. In: WIT Transactions on the Built Environment, 125, 15-26. doi.org/10.2495/OP120021

Kravanja, S., Žula, T. (2018). MINLP optimization of the underground lined rock. In: Conference proceedings, International Conference on Technologies & Business Models for Circular

Economy, 1, 2018, Portorož. 1st ed. Maribor: University of Maribor Press, 149-157. http://press.um.si/index.php/ump/catalog/view/367/345/590-2.

Kravanja, Z. (2010). Challenges in sustainable integrated process synthesis and the capabilities of an MINLP process synthesizer MipSyn. *Comput Chem Eng*, 34(11), 1831-1848. doi:10.1016/j.compchemeng.2010.04.017

Sofregaz US Inc. (1999). Commercial potential of natural gas storage in lined rock caverns (LRC). US Department of Energy, Federal Energy Technology Center.

Žlender, B., Kravanja, S. (2011). Cost optimization of the underground gas storage. *Eng Struct*, 33, 2554-2562. doi.org/10.1016/j.engstruct.2011.05.001

FIBRE REINFORCED ALKALI-ACTIVATED ROCK WOOL

MAJDA PAVLIN, BARBARA HORVAT, VILMA DUCMAN
Slovenian National Building and Civil Engineering Institute, Ljubljana, Slovenia
majda.pavlin@zag.si, barbara.horvat@zag.si, vilma.ducman@zag.si

Abstract Mineral wool, i.e. rock and glass wool, represents considerable challenge after its functional-time runs out due to its small density leading to large volume consumption during transport and in landfills where it usually ends. Because rock wool is mineralogically and chemically a promising precursor material for alkali-activation, it was milled from few centimetres-decimeters long fibres to micron-sized fibres. Since fibres in alkali-activated materials generally show an increase in mechanical strength, especially the bending strength, 1 m% of additional fibres (basalt, cellulose (2 types), glass, polypropylene, polyvinyl alcohol and steel fibres) was used in the alkali mixture, that was curred at 40 °C for 3 days. Time dependence of the mechanical strengths of alkali-activated materials with and without additional fibres was followed. Maximal increase of compressive and bending strength after 28 days was reached with polypropylene fibres, i.e. it was 20% and 30% higher than compressive and bending strength of alkali-activated material without additional fibres respectively.

Keywords:
waste mineral wool,
fibre,
alkali-activated material,
mechanical strength,
upcycling

University of Maribor Press

DOI https://doi.org/10.18690/um.fkkt.2.2022.6
ISBN 978-961-286-598-6

1 Introduction

Mineral wool (rock/stone, glass and slag wool) is a material consisting of fibres and shots, where shots did not fiberize before solidification. The less the shots mineral wool contains, the better it's quality (Brane Sirok et al., 2008). Newer production technologies add on fibres' surface different organic resins as the binder to modify mineral wool's compressive, bending and tensile strengths (Kowatsch, 2010). Yearly global production of the mineral wool is increasing with the average annual rate of 1.8% since 2013 and has reached 19M tonnes in 2019 ("The Global Mineral Wool Market Started to Slow Down - Global Trade Magazine," n.d.), while the yearly amount of mineral wool's waste in Austria is 20-30K tonnes (Sattler et al., 2020). When predicted that mineral wool waste is approximately linked to the number of inhabitants, mineral wool waste in all EU countries together is then 1M-1.5M tonnes yearly. Therefore it is crucial to solve the problem of waste mineral wool disposal due to its large volume consumption during transport and in landfills.

One way for use of the waste mineral wool is using it as a precursor in alkali activation, where milled mineral wool reacts with alkali and forms aluminosilicate matrix, in which not-reacted fibres get completely immobilized (Horvat et al., 2018). Alkali activation idea was 1st reported in a patent in 1895, whereas the precursor was proposed blast-furnace slag and as activator the caustic soda with slaked lime (Whiting, 1895). But only in last decade researchers started to test also some other precursors than metakaolin, slag and fly-ash, i.e. refractory materials, foundry sand and other foundry wastes (Horvat et al., 2019), waste green ceramics (Horvat and Ducman, 2019) and last years also waste mineral wools where glass wool had higher compressive strength than rock wool (Yliniemi et al., 2016). All these materials can be used in alkali activation because they contain big enough amount of amorphous Al and Si, which are present in the matrix in the tetrahedron formation with O-bridges. To compensate electric charge of Al in the tetrahedron, elements of the 1st and 2nd group are needed, i.e. the positive ions either come from the precursor if it contains them in the amorphous phase, or from the alkali activator (Horvat and Ducman, 2019).

In many materials, additional mechanical reinforcement is achieved with the addition of fibres made from different materials and of different sizes and shapes, i.e. in polymer composites (Navin Chand, 2008), metal and ceramic matrix composites (Eckold, 1994), civil engineering composites (Harris, 2005), syntactic foams (Sydney H. Goodman and Hanna Dodiuk-Kenig, 2014) etc.

The purpose of presented work is to evaluate the effect of several different fibres (basalt, cellulose, glass, polypropylene, polyvinyl alcohol and steel fibres) on mechanical strengths in alkali activated pulverized waste rock wool.

2 Materials and Methods

2.1 Analysis of precursor, additives and alkali-activated materials

Rock wool waste (RW) (Horvat et al., 2018), labelled 17 09 041, was collected from Termit. RW was 1st manually cleaned of all large impurities, cut into smaller pieces, and milled in a concrete mixer by using steel balls (27 pieces, 47.5 mm in diameter), every kilogram of RW for 2.5 hours (coarse RW). The milled sample was dried at 105 °C for 24 hours and sieved below 63 μm. The residue was ground in the homogenizer (powder mixer shaker, Turbola T2F) in 2 l plastic container with steel balls (50 pieces of diameter 9.8 mm) and sieved below 63 μm (fine RW).

The particle size of coarse and fine RW was measured by particle size and shape analyzer (Microtrac MRB, SYNC).

Fibres were used from previous projects: basalt (B), cellulose (fibres (CF) and fibres squeezed into thin cubes (CC)), glass (G), polypropylene (PP), polyvinyl alcohol (PVA) and steel fibres (S).

Chemical analysis of RW was performed using X-ray fluorescence (XRF; Thermo Scientific ARL Perform'X Sequential XRF) on melted discs of the mixture of ignited RW powder (sieved below 63 μm) and $Fluxana_{(s)}$ (FX-X50-2, lithium tetraborate 50% / lithium metaborate 50% is used to lower melting point) with the addition of a few drops of $LiBr_{(l)}$ (prepared from 50 ml H_2O and 7.5 g of $LiBr_{(s)}$ from Acros Organics, which is used to avoid sticking of the melt to the platinum vessel). Obtained data were characterized by software UniQuant 5.

Mineralogical characterization of RW powder (sieved below 63 μm) was performed with X-ray powder diffraction (XRD; Empyrean PANalytical X-ray Diffractometer, Cu X-ray source) and software X'Pert Highscore plus 4.1. Rietveld refinement with an external standard (a pure Al_2O_3 crystal) was used to estimate the amount of amorphous phase and minerals.

Scanning electron microscope (SEM; Jeol JSM-IT500) under low vacuum conditions was used to investigate surface, shape, size and microstructure of non-sputtered RW, fibres and/or alkali-activated materials.

Bending and compressive strength of alkali-activated fibreless and fibre reinforced samples were measured with compression and bending strength testing machine (ToniTechnik ToniNORM) at age 3 and 28 days.

Alkali-activated samples' geometric density was determined by weighting the sample and dividing its mass by its volume.

2.2 Preparation of alkali-activated samples

RW as precursor and fibres used as additional reinforcement in alkali-activated synthesis are shown in Fig. 1. RW that was used in alkali-activation was prepared in the same manner as for XRF and XRD analysis, i.e. milled and sieved below 63 μm, while dry fibres were used as received.

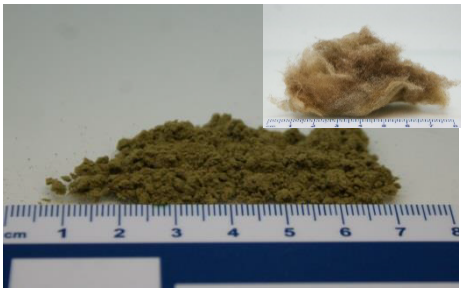

(**a**)

(**b**)

Figure 1: Photograph of (a) milled and sieved RW (on the inset is original RW), and fibres: (b) basalt, (c) cellulose fibres, (d) cellulose cubes, (e) glass fibres, (f) polypropylene fibres, (g) polyvinyl alcohol fibres, and (h) steel fibres.

Source: own.

As alkali-activator, only Na-water glass (Silvez, mining company Termit, with the mass percentage of Na_2O 12.8%, and mass percentage of SiO_2 29.2%) was used. Alkali slurry was prepared in mass ratio RW : Na-water glass : fibre = 100 : 95 : 0/1, moulded into rubber-silicon moulds measuring (80x20x20) mm^3 and cured in drying chamber (WTB Binder) at 40 °C for 3 days.

3 Results and discussion

3.1 Analysis of precursor

SEM micrographs of RW that was not milled (original RW), that was milled (coarse RW), and that was milled for so long that it could be sieved below 63 μm (fine RW) are presented in Fig. 2 (a, b, c respectively). Particle size analysis of coarse and fine RW is presented in Fig. 3.

(**a**)

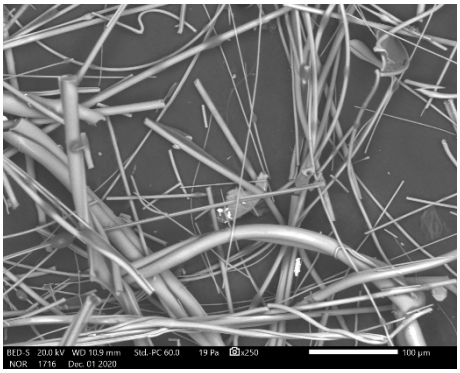

(**b**)

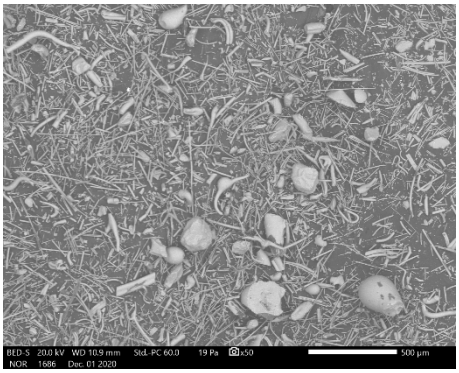

(**c**)

(**d**)

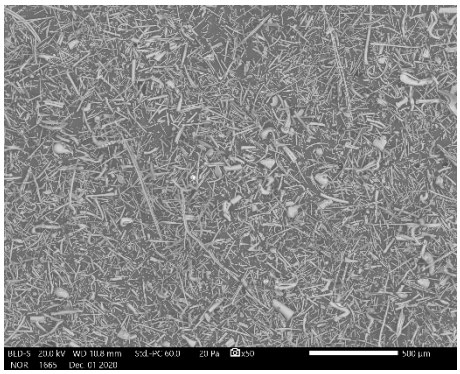

(**e**)

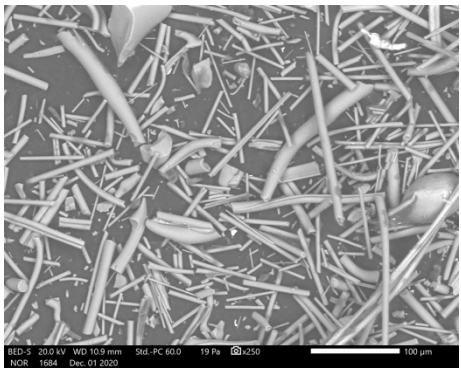

(**f**)

Figure 2: SEM micrographs of not milled RW [(a) magnification 50x, (b) magnification 250x], milled RW [(c) magnification 50x, (d) magnification 250x], milled and sieved below 63 µm RW [(e) magnification 50x, (f) magnification 250x].

Source: own.

RW, even if milled and sieved below 63 µm, keeps an elongated cylindrical shape (Fig. 2). With 1st step milling long thin fibres are broken into smaller pieces (Fig. 2 (a) to (c)), while "stones" stay intact until the sample is milled so long that it can be fully sieved below 63 µm (Fig. 2 (c) to (e)). The milling effect can be seen also in Fig. 3, where red line represents material after 1st step milling and the blue line represents material that was milled and sieved under 63 µm. Both prepared samples are fine-grained, i.e. more than 50% of all material is smaller from 75 µm: 50% of coarse RW grains are below or equal to 52 µm, while 50% of fine RW grains are smaller or equal to 31 µm. Coefficient of uniformity for coarse RW is 6.7, while for fine RW is 4.8. Coefficient of curvature on the other hand is for coarse RW 0.8, while for fine RW is a bit higher than 1.0. For the well-graded material coefficient of uniformity should be bigger from 1, and the coefficient of curvature between 1 and 3, meaning that only fine RW is well graded. Therefore in alkali-activation, only RW that was milled and sieved below 63 µm was used as a precursor.

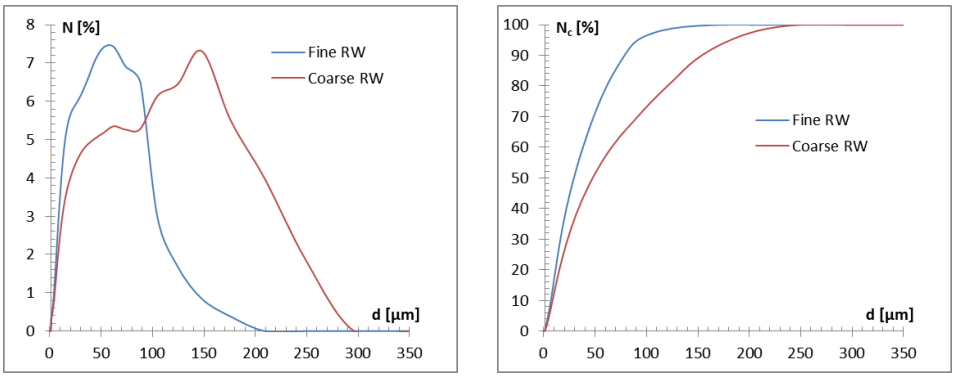

(**a**) (**b**)

Figure 3: (a) Particle size distribution, (b) cumulative particle size distribution of coarse RW (red line), and fine RW (blue line).

Source: own.

All fibres used in alkali-activation to gain higher bending and compressive strength are presented in Fig. 4. Natural fibres are from cellulose (Fig. 4 (c) to (f), CC and CF), while all the rest are completely artificial (B, G, PP, PVA and S). Several of them are found ordered in larger groups: B, G and PVA; without any specific order is CF, PP, and also S (which is present in alkali-activated synthesis just as few fibres due to its higher density); while CC is squeezed into thin cubes with random orientation of cellulose fibres.

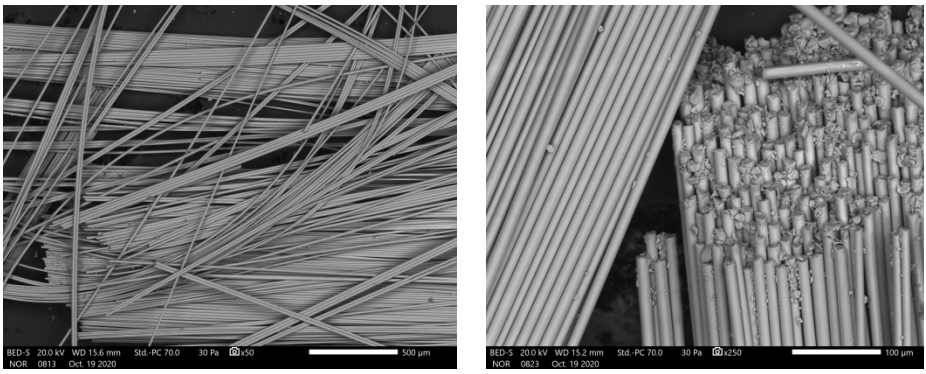

(**a**) (**b**)

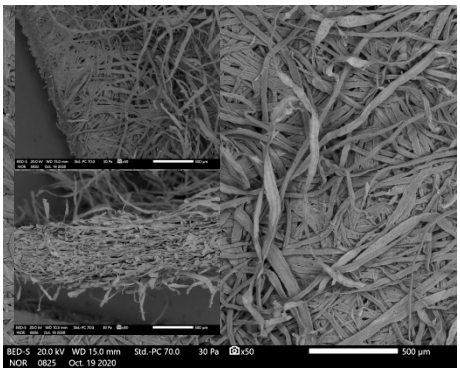
BED-S 20.0 kV WD 15.0 mm Std.-PC 70.0 30 Pa x50 500 µm
NOR 0825 Oct. 19 2020

(**c**)

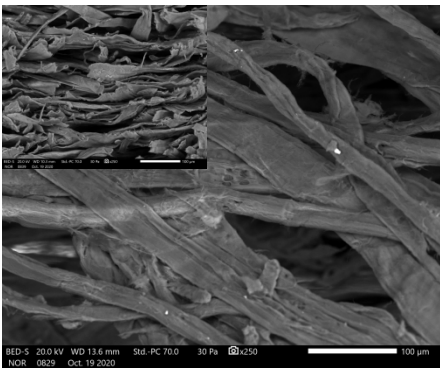
BED-S 20.0 kV WD 13.6 mm Std.-PC 70.0 30 Pa x250 100 µm
NOR 0829 Oct. 19 2020

(**d**)

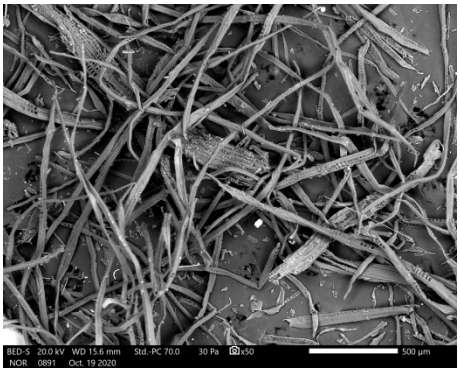
BED-S 20.0 kV WD 15.6 mm Std.-PC 70.0 30 Pa x50 500 µm
NOR 0891 Oct. 19 2020

(**e**)


BED-S 20.0 kV WD 15.5 mm Std.-PC 70.0 30 Pa x250 100 µm
NOR 0880 Oct. 19 2020

(**f**)

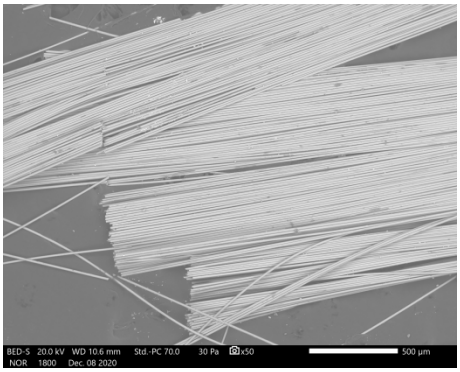
BED-S 20.0 kV WD 10.6 mm Std.-PC 70.0 30 Pa x50 500 µm
NOR 1800 Dec. 08 2020

(**g**)

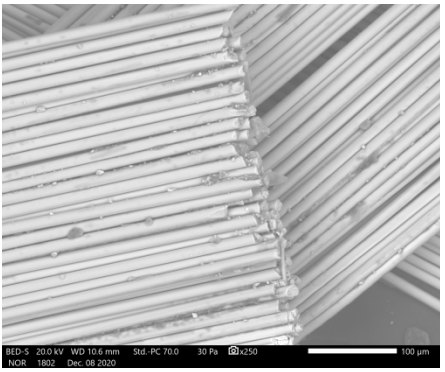
BED-S 20.0 kV WD 10.6 mm Std.-PC 70.0 30 Pa x250 100 µm
NOR 1802 Dec. 08 2020

(**h**)

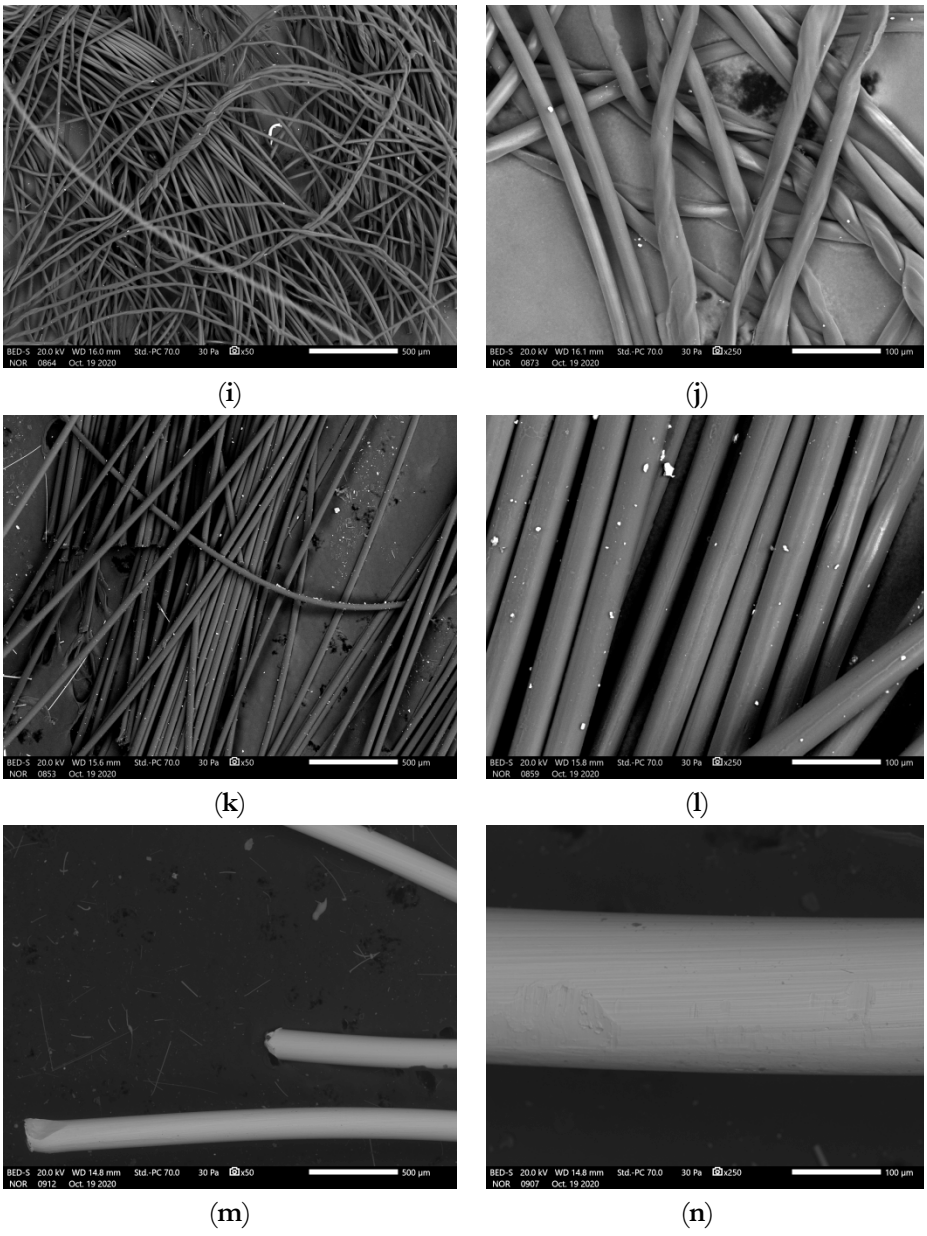

Figure 4: SEM micrographs of fibers at 50x (left) and 250x (right) magnification: B [(a), (b)], CC [(c, (d)], CF [(e), (f)], G [(g), (h)], PP [(i), (j)], PVA [(k), (l)], and S [(m), (n)].

Source: own.

XRF chemical analysis of RW is presented in 1st row in Table 1, XRD mineralogical analysis is in its 2nd row of Table 1, wherein crystalline phase only small amount of quartz was present (determined by Rietveld refinement), and in the 3rd line of Table 1 elements' mass percentages in the amorphous phase are calculated as the difference between the XRF and XRD results.

Table 1: Chemical (XRF) and mineralogical (XRD) analysis of RW.

Precursor	Elements/m%	Na	K	Cs	Mg	Ca	Sr	Ba	Al	Si
RW	XRF	1.5	0.2	0	6.3	11.6	0	0	8.6	18.9
	XRD	0	0	0	0	0	0	0	0	0.1
	XRF-XRD	1.5	0.2	0	6.3	11.6	0	0	8.6	18.8

According to the literature (Duxson et al., 2005) for reaching the highest compressive strength most promising ratio Na, Al and Si present in AAM is 1:1:1.9. In our previous work (Horvat and Ducman, 2019) this model was tested and upgraded to be able to compare the amorphous amount of whole 1st and 2nd group to Al and Si, to predict also potential future efflorescence. For used RW ratio of the amount of substance between (1st : 2nd : Al : Si) is (0.2: 1.7 : 1 : 2.1). If no element from the 2nd group participates in the reaction, efflorescence can be avoided by the addition of elements from 1st group with NaOH without changing the amount of Si, or with Na-water glass were the amount of Si rises and could compromise the final mechanical strength as a side effect.

3.2 Analysis of alkali-activated samples

The compressive and bending strength of 3 and 28 days old alkali-activated RW with and without fibres is presented in Table 2 and Fig. 5.

Mechanical strengths of all alkali-activated samples with and without fibres increase with time while their density decreases due to the evaporation of water, i.e. shrinking has a smaller effect than the mass loss. At the same time, chemical reactions (besides physical evaporation of water) are still going on and creating strong chemical bonds in the matrix. These bonds more than just compensate the negative effects of the evaporation that result in crack formation in the matrix (which can be seen on micrographs of alkali-activated materials presented on Fig. 6).

Table 2: Compressive and bending strengths of alkali-activated samples with their geometrical densities after 3 and 28 days (presented on one decimal).

Fibre	Compressive strength/ MPa		Bending strength/ MPa		Density/ kg/l	
	3 days	28 days	3 days	28 days	3 days	28 days
/	21.3	38.6	7.3	11.3	1.7	1.6
B	26.2	32.9	7.8	13.0	1.8	1.6
CC	21.1	30.0	7.7	12.0	1.7	1.6
CF	21.5	38.8	6.1	12.4	1.7	1.7
G	18.1	41.3	5.4	17.9	1.8	1.6
PP	27.4	40.1	9.5	12.2	1.8	1.6
PVA	25.5	43.8	9.1	14.5	1.7	1.6
S	24.6	39.9	7.9	12.7	1.7	1.7

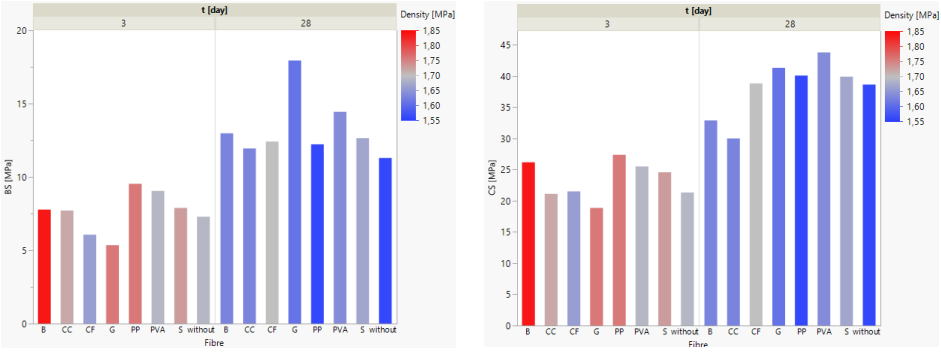

(**a**) (**b**)

Figure 5: (a) Bending and (b) compressive strength of alkali activated RW with and without fibres.

Source: own.

All fibres used in alkali-activation of RW increased the bending strengths of 28-days old material, while for compressive strengths this is true only for G, PP, PVA and S, while other fibres either decreased its value (B, CC) or had no influence (CF). Highest reached BS after 28 days had a sample with G fibres (17.9 MPa was BS, while CS reached 41.3 MPa), while highest CS after 28 days had sample with PVA fibres (43.8 MPa was CS, while BS reached 14.5 MPa), i.e. CS and BS for samples containing G fibres was 10% and 60% higher than values for reference respectively, while CS and BS for samples containing PVA fibres was 20% and 30% bigger from alkali-activated RW without additional fibres.

SEM micrographs of alkali-activated samples with and without fibres are presented on Fig. 6. Matrix of alkali-activated RW did not change with the addition of fibres, because none reacted with alkali and did not change the chemical reaction. All samples had spherical pores (organic resin present on RW reacts with alkali and releases gasses, which get trapped into the matrix when matrix gets too viscose for the bubble to be able to travel out from the slurry with the difference of densities; Fig. 6 (a)) and 1-dimensional cracks which are a consequence of physical evaporation of water while drying (Fig. 6 with magnification 250).

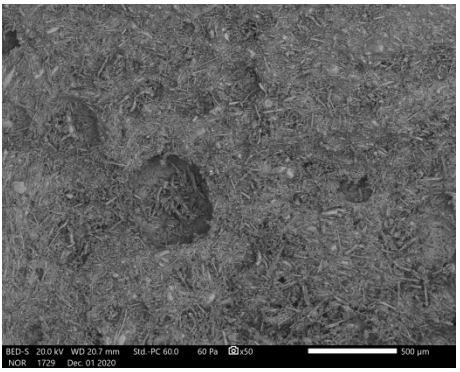

(**a**)

(**b**)

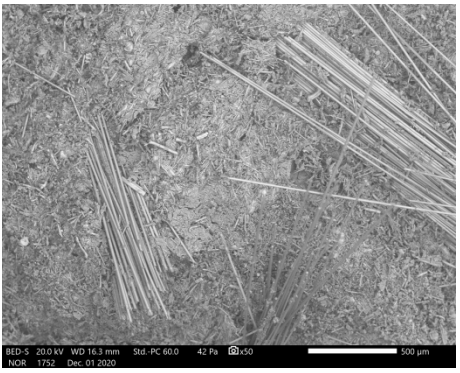

(**c**)

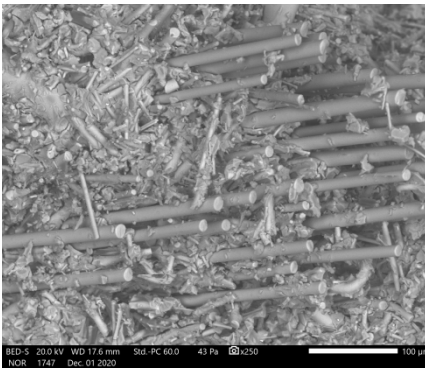

(**d**)


BED-S 20.0 kV WD 14.9 mm Std.-PC 60.0 41 Pa x50 500 µm
NOR 1755 Dec. 01 2020

(**e**)

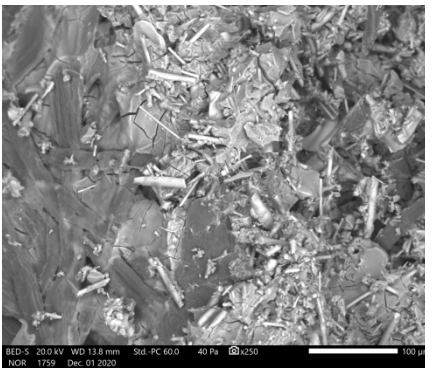
BED-S 20.0 kV WD 13.8 mm Std.-PC 60.0 40 Pa x250 100 µ
NOR 1759 Dec. 01 2020

(**f**)


BED-S 20.0 kV WD 13.0 mm Std.-PC 60.0 35 Pa x50 500 µm
NOR 1780 Dec. 01 2020

(**g**)

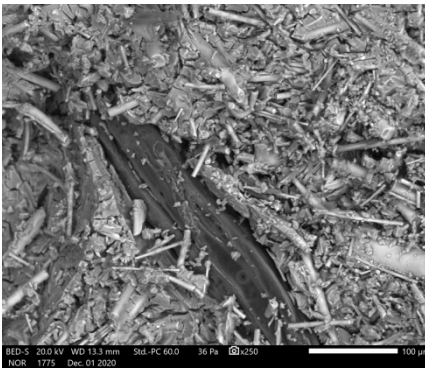
BED-S 20.0 kV WD 13.3 mm Std.-PC 60.0 36 Pa x250 100 µ
NOR 1775 Dec. 01 2020

(**h**)


BED-S 20.0 kV WD 19.3 mm Std.-PC 70.0 81 Pa x50 500 µm
NOR 1843 Dec. 11 2020

(**i**)


BED-S 20.0 kV WD 13.4 mm Std.-PC 70.0 76 Pa x250 100 µ
NOR 1849 Dec. 11 2020

(**j**)

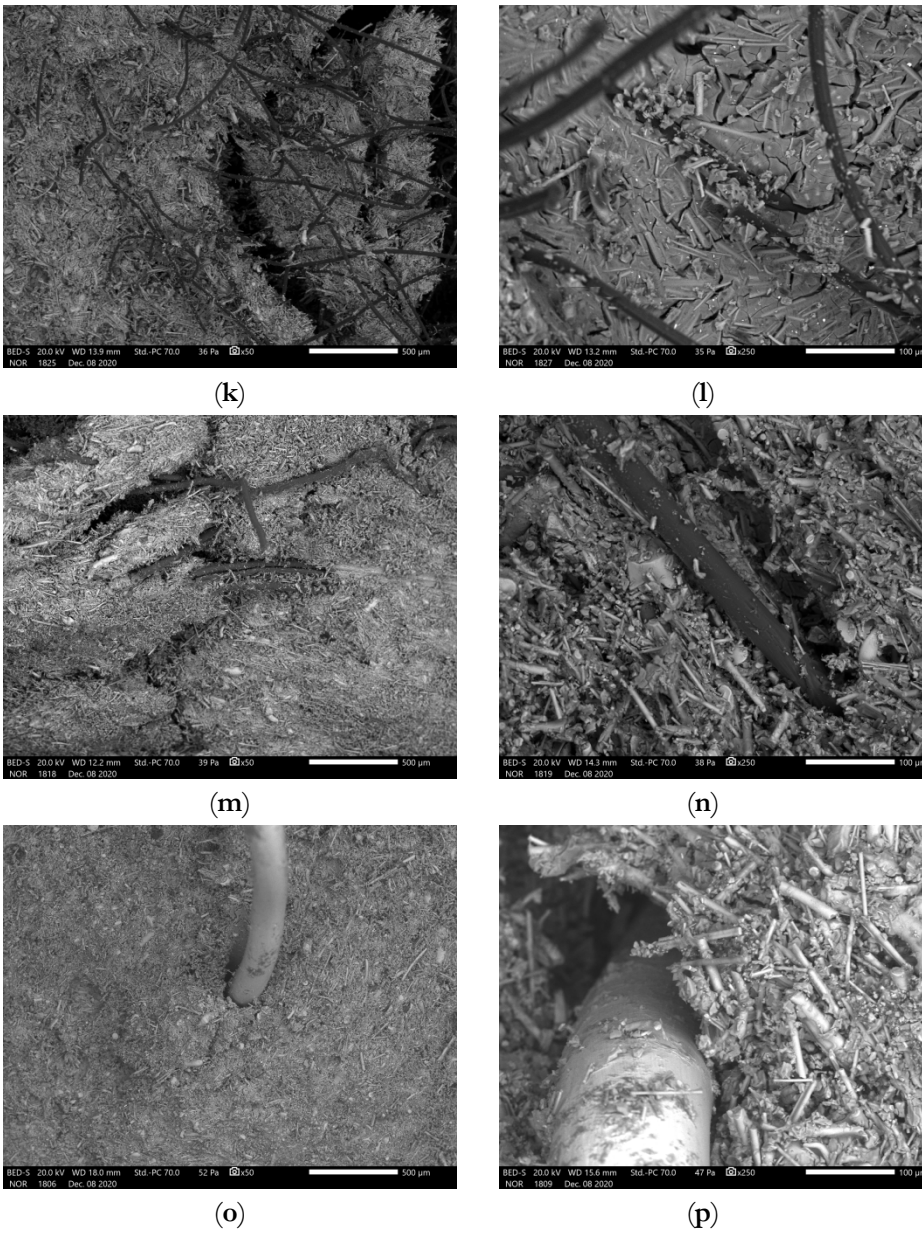

Figure 6: SEM micrographs of alkali-activated RW at 50x (left) and 250x (right) magnification without additional fibres [(a), (b)], and with additional fibres: B [(c, (d)], CC [(e), (f)], CF [(g), (h)], G [(i), (j)], PP [(k), (l)], PVA [(m), (n)], and S [(o), (p)].

Source: own.

To determine the optimal amount of added fibres further investigation is needed, where focus would be also on the number of fibres (through density and mass), their geometry (approximate diameter and length) and their whole surface area present in the alkali-activated material.

4 Conclusions

The results show that the addition of fibres is beneficial for bending strength, while compressive strength increased only with the addition of glass, polypropylene, polyvinyl alcohol and steel fibres, while other fibres left the compressive strength either intact, or even lowered it. Most promising among all samples, that increased both mechanical strengths, was a sample with added polyvinyl alcohol fibres (bending strength increased for 20%, while compressive strength for 30%), while addition of glass fibres resulted in overall biggest increase of bending strength (60%).

Acknowledgements

Project No. C3330-17-529032 "Raziskovalci-2.0-ZAG-529032" was granted by Ministry of Education, Science and Sport of the Republic of Slovenia. The investment is co-financed by the Republic of Slovenia, Ministry of Education, Science and Sport and the European Regional Development Fund. WOOL2LOOP project received funding from the European Union's Horizon 2020 research and innovation programme under grant agreement No 821000. Slovenian Research Agency supported Programme Group P2-0273.

The Metrology Institute of the Republic of Slovenia is acknowledged for the use of XRF.

Cooperation with Termit d.d. and Mrs Alenka Sešek Pavlin from Termit d.d.is highly appreciated.

References

Brane Sirok, Bogdan Blagojevic, Peter Bullen, 2008. Mineral Wool Production and Properties. Woodhead Publishing.

Duxson, P., Provis, J.L., Lukey, G.C., Mallicoat, S.W., Kriven, W.M., van Deventer, J.S.J., 2005. Understanding the relationship between geopolymer composition, microstructure and mechanical properties. Colloids and Surfaces A: Physicochemical and Engineering Aspects 269, 47–58. https://doi.org/10.1016/j.colsurfa.2005.06.060

Eckold, G., 1994. Design and manufacture of composite structures. Woodhead, Cambridge.

Harris, B., 2005. Fatigue in Composites: Science and Technology of the Fatigue Response of Fibre-Reinforced Plastics 870.

Horvat, B., Češnovar, M., Pavlin, A., Ducman, V., 2018. Upcycling with alkali activation technology, in: Technologies & Business Models for Circular Economy. Presented at the 1st International Conference on Technologies & Business Models for Circular Economy, Univerzitetna založba Univerze v Mariboru / University of Maribor Press, pp. 261–272. https://doi.org/10.18690/978-961-286-211-4.22

Horvat, B., Ducman, V., 2019. Potential of Green Ceramics Waste for Alkali Activated Foams 30.

Horvat, B., Pavlin, A.S., Ducman, V., 2019. Foundry wastes as potential precursor in alkali activation technology, in: Technologies & Business Models for Circular Economy. Presented at the 2nd International Conference on Technologies & Business Models for Circular Economy, Univerzitetna založba Univerze v Mariboru / University of Maribor Press.

Kowatsch, S., 2010. Mineral Wool Insulation Binders, in: Pilato, L. (Ed.), Phenolic Resins: A Century of Progress. Springer Berlin Heidelberg, Berlin, Heidelberg, pp. 209–242. https://doi.org/10.1007/978-3-642-04714-5_10

Navin Chand, 2008. Tribology of Natural Fiber Polymer Composites. Woodhead Publishing.

Sattler, T., Pomberger, R., Schimek, J., Vollprecht, D., 2020. MINERAL WOOL WASTE IN AUSTRIA, ASSOCIATED HEALTH ASPECTS AND RECYCLING OPTIONS. Detritus 174–180. https://doi.org/10.31025/2611-4135/2020.13904

Sydney H. Goodman, Hanna Dodiuk-Kenig, 2014. Handbook of Thermoset Plastics, Third. ed. William Andrew.

The Global Mineral Wool Market Started to Slow Down - Global Trade Magazine [WWW Document], n.d. URL https://www.globaltrademag.com/the-global-mineral-wool-market-started-to-slow-down/ (accessed 12.19.20).

Whiting, J., 1895. Manufacture of Cement. 544706.

Yliniemi, J., Kinnunen, P., Karinkanta, P., Illikainen, M., 2016. Utilization of Mineral Wools as Alkali-Activated Material Precursor. Materials 9, 312. https://doi.org/10.3390/ma9050312

ACTIVITY OF α-AMYLASE FROM *P. OSTREATUS* GROWN ON WASTE SUBSTRATES

MATEJA PRIMOŽIČ,[1] ŽELJKO KNEZ,[1,2] MAJA LEITGEB[1,2]

[1] University of Maribor, Faculty of Chemistry and Chemical Engineering, Laboratory for Separation Processes and Product Design, Maribor, Slovenia
mateja.primozic@um.si, zeljko.knez@um.si, mateja.leitger@um.si
[2] University of Maribor, Faculty of Medicine, Maribor, Slovenia
zeljko.knez@um.si, mateja.leitger@um.si

Abstract Forest and agricultural waste can be a major development and ecological opportunity. Therefore, it is reasonable to use biological waste further to produce energy and for the manufacture of certain products with high added value, such as, for example, the cultivation of fungi and, consequently, the production of biocatalysts with high market value. In addition, the use of agriculture waste for Oyster mushroom (*Pleurotus ostreatus*) growth can be integrated to waste management and the development of the bioeconomy. The cultivation of *P. ostreatus* using waste plant biomass from agriculture (straw, grass, courgettes, cucumbers, peaches, apricots, pears, and peppers) was performed in order to obtain the highest increase in biomass production of the cultivated mushroom and as a potential source of α-amylase, with high catalytic activity. The highest α-amylase activities were achieved when pears or apricots were used as a substrate for *P. ostreatus* cultivation.

Keywords: *P. ostratus*, α-amylase, activity, agriculture waste, cultivation

University of Maribor Press

DOI https://doi.org/10.18690/um.fkkt.2.2022.7
ISBN 978-961-286-598-6

1 Introduction

One of the economically interesting medical mushrooms is *P. ostreatus*, which is easily cultivated by beginners, as it has an extremely strong undergrowth. The genus *Pleurotus* includes groups of edible ligninolytic fungi with medicinal properties and important biotechnological and environmental applications. One of the most important aspects of *Pleurotus* fungi is related to the use of their ligninolytic system for various applications, such as the biological conversion of agricultural waste into useful animal feed and other food products, and the use of their ligninolytic enzymes for biodegradation of organic pollutants, xenobiotics and industrial contaminants. The cultivation of *P. ostreatus* is important for the production of lignocellulosic and other enzymes. Mushrooms are grown on different nutrient bases, i.e. substrates in which the undergrowth or mycelium develops. These substances, however, contain polymeric organic compounds that are difficult to decompose. In order to consume organic matter, mushrooms must first eliminate certain enzymes that decompose this substrate. The prevalence of mushroom enzymes has long been known and exploited for use in the food industry and in many other industries. Mushrooms respond to their habitat through controlled gene expression and secretion of specific enzymes. The enzymes split the molecules into smaller units, and mushrooms mycelium absorbs these reduced organic molecules as nutrients directly through the cell walls. The conversion of substrates into mushroom biomass is mediated by the secretion of a variety of hydrolytic and oxidative enzymes. In nature, *P. ostreatus* grows on waste wood, but it is also possible to grow it on agrarian waste to produce enzymes to stimulate oxidation reactions (laccase, manganese peroxidase, lignin peroxidase) and hydrolysis (amylase, cellulase, xylanase, tanase)(da Luz et al., 2012). The cultivation of *P. ostreatus*, *Pleurotus eryngii*, *Pleurotus pulmonarius*, *Agrocybe Aegerita* and *Volvariella volvacea* was performed on three types of agricultural waste (wheat straw, cotton waste, and peanut shells) (Philippoussis et al., 2001). High growth rates of all studied mushroom cultures on the agricultural waste were detected. Waste of coffee leaves, eucalyptus bark, with or without the addition of rice bran, was used as the substrate for *P. ostreatus* cultivation. The lignocellulolytic enzyme activity increased with time after inoculation and the substrate composition affected the enzyme activity (da Luz et al., 2012). The production of lignocellulolytic enzymes such as laccase, manganese peroxidase, endoglucanase, exoglucanase and 3-glucosidase was successfully performed by degradation of Chrysanthemum and Rosa residues using *P. ostreatus* (Quevedo-Hidalgo et al., 2015). Rashad et al.

(Rashad et al., 2009) studied the enzymatic activity of amylase, cellulase, invertase, polygalacturonase and pectinase from *P. ostreatus* cultivated on citrus wastes and papaya. A higher activity of amylase was observed in the unsupplemented lemon pulp and papaya waste. Further, the ability of *P. ostreatus* and *Pleurotus sajor-caju* fungi to produce laccase and carboxymethylcellulase enzymes on a variety of agricultural wastes in the solid-state fermentation process (SSF) was studied. Enzymatic activity was highest on substrates that contained bran, had high nitrogen content and low C/N ratio (Kurt & Buyukalaca, 2010). Belšak-Šel et al. (Belšak-Šel et al., 2015) studied the increase in laccase production from *P. ostreatus* by optimizing the culture medium. The level of laccase activity produced by *P. Ostreatus* in the SSF process in wheat bran was significantly influenced by lignocellulose biomass and glucose content. Production of enzymes with SSF offers the advantage of reducing production costs and increasing the rate of mycelium growth. Additional, *P. ostreatus*, as well as other mushrooms (*Lentinula edodes*, *G. frondosa*, *Cantharellus cibarius* and *Agaricus bisporus*) are rich in B vitamins (Solomko & Eliseeva, 1988), organic acids, β - lipids, proteins and micronutrients (e.g. selenium or chromium)(Dikeman et al., 2005; Valentão et al., 2005). Amylases are important in many industrial processes and are one of the most widely used enzymes required for the preparation of fermented foods and now in the light of biotechnology they are considered useful for biopharmaceutical applications. They are useful tools in medicinal and clinical applications (Afzaljavan & Mobini-Dehkordi, 2013). α-Amylases can be obtained from plants, animals and microorganisms. However, enzymes from fungal and bacterial sources have dominated applications in industrial sectors (de Souza & de Oliveira Magalhães, 2010).

Therefore, *P. ostreatus* was cultivated on waste vegetable biomass from agriculture (straw, grass, courgettes, cucumbers, peaches, apricots, pears, and peppers) in combination with wheat bran to maximize mushroom growth as a potential source of α-amylase.

2 Methods

2.1 *P. ostreatus* cultivation

P. ostreatus was cultivated on substrate containing waste vegetable biomass from agriculture and wheat bran in volumetric ratio 1:1 in the presence of growth media from yeast extract and peptone. The *P. ostreatus* was cultivated for 8 days at 27 °C.

2.2 Extraction of enzymes from *P. ostreatus*

The extraction of *P. ostreatus* mycelium was performed using 0.05 M sodium citrate buffer as a solvent and for 90 min by shaking at 200 rpm. The obtained extract was centrifuged 20 min at 5000 rpm. Supernatant was used for the determination of α-amylase activity.

2.3 Determination of total protein concentration and α-amylase activity

The total protein concentration was assayed by the Bradford method (Bradford, 1976) and activity of α-amylase was defined spectrophotometrically at 595 nm. The activity was expressed as the change in absorbance at 595 nm per minute per solid of α-amylase (Čolnik et al., 2016).

3 Results

3.1 Mycelium growth of *P. ostreatus*

P. ostreatus was cultivated on waste vegetable biomass from agriculture (straw, grass, courgettes, cucumbers, peaches, apricots, pears, and peppers) in combination with wheat bran to maximize mushroom growth. The increase in mycelium growth of *P. ostreatus* after 8 days of cultivation on different substrates was pursued (Figure 1).

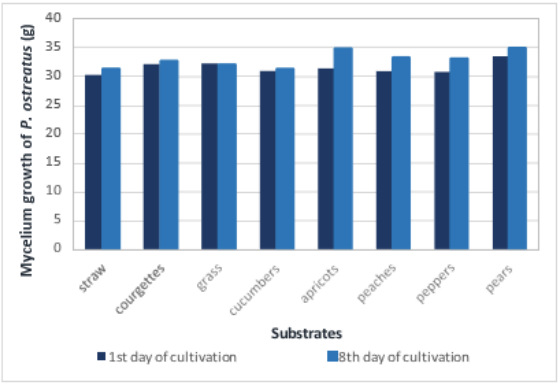

Figure 1: Influence of substrates on mycelium growth of *P. ostreatus*
Source: own.

As can be seen from Figure 1, the highest increase in mycelium growth of *P. ostreatus* after 8 days of cultivation on different substrates was detected when apricot as a substrate was used. Significant increase in mycelium growth of *P. ostreatus* was also detected when straw, peaches, pears, and peppers were used as a substrate.

As can be seen from Figure 1, the highest increase in mycelium growth of *P. ostreatus* after 8 days of cultivation on different substrates was detected when apricot as a substrate was used. Significant increase in mycelium growth of *P. ostreatus* was also detected when straw, peaches, pears, and peppers were used as a substrate.

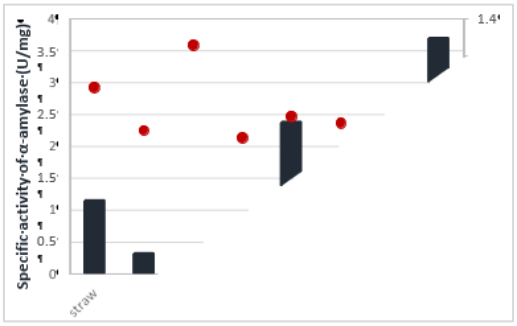

Figure 2: Influence of substrates on total protein concentration and specific activity of α-amylase
Source: own.

4 Conclusion

The *P. ostreatus* fungus was successfully grown on waste vegetable biomass from agriculture (straw, grass, courgettes, cucumbers, peaches, apricots, pears, and peppers) in combination with wheat bran. With increase in the time of cultivation of *P. ostreatus* on selected media, an increase in biomass growth was detected. The most suitable substrate, among those tested, for α-amylase production was composed from pear and wheat bran. Thus, waste vegetable biomass are suitable substrates for the cultivation of *P. ostreatus* for the purpose of α-amylase production. Due to bioconversion of nutrient-rich waste and by-product to value-added products, the environmental burdens imposed by these wastes are alleviated, and consequently, the regional and international economy can be boosted.

Acknowledgement

The authors acknowledge the financial support from the Slovenian Research Agency (research core funding No. P2-0046 - "Separation Processes and Product Design").

References

Afzaljavan, F., & Mobini-Dehkordi, M. (2013). *Application of alpha-amylase in biotechnology*. LAP LAMBERT Academic Publishing. https://www.morebooks.de/store/gb/book/application-of-alpha-amylase-in- biotechnology/isbn/978-3-659-40419-1

Belšak-Šel, N., Gregori, A., Leitgeb, M., Klinara, D., & Čelan, Š. (2015). Effect of Solid State Fermentation Medium Optimization on Pleurotus ostreatus Laccase Production. *Acta Chimica Slovenica*, *62*(4), 932–939. https://doi.org/10.17344/acsi.2015.1764

Bradford, M. (1976). Rapid and Sensitive Method for Quantitation of Microgram Quantities of Protein Utilizing Principle of Protein-Dye Binding. *Analytical Biochemistry*, *72*(1–2), 248–254. https://doi.org/10.1006/abio.1976.9999

Čolnik, M., Primožič, M., Knez, Ž., & Leitgeb, M. (2016). Use of Non-Conventional Cell Disruption Method for Extraction of Proteins from Black Yeasts. *Frontiers in Bioengineering and Biotechnology*, *4*, 33. https://doi.org/10.3389/fbioe.2016.00033

da Luz, J. M. R., Nunes, M. D., Paes, S. A., Torres, D. P., de Cássia Soares da Silva, M., & Kasuya, M. C. M. (2012). Lignocellulolytic enzyme production of Pleurotus ostreatus growth in agroindustrial wastes. *Brazilian Journal of Microbiology*, *43*(4), 1508–1515. https://doi.org/10.1590/S1517-838220120004000035

de Souza, P. M., & de Oliveira Magalhães, P. (2010). Application of microbial α-amylase in industry – A review. *Brazilian Journal of Microbiology*, *41*(4), 850–861. https://doi.org/10.1590/S1517-83822010000400004

Dikeman, C. L., Bauer, L. L., Flickinger, E. A., & Fahey, G. C. (2005). Effects of stage of maturity and cooking on the chemical composition of select mushroom varieties. *Journal of Agricultural and Food Chemistry*, *53*(4), 1130–1138. https://doi.org/10.1021/jf048541l

Kurt, S., & Buyukalaca, S. (2010). Yield performances and changes in enzyme activities of Pleurotus spp. (P. ostreatus and P. sajor-caju) cultivated on different agricultural wastes. *Bioresource Technology*, *101*(9), 3164–3169. https://doi.org/10.1016/j.biortech.2009.12.011

Philippoussis, A., Zervakis, G., & Diamantopoulou, P. (2001). Bioconversion of agricultural lignocellulosic wastes through the cultivation of the edible mushrooms Agrocybe aegerita, Volvariella volvacea and Pleurotus spp. *World Journal of Microbiology and Biotechnology*, *17*(2), 191–200. https://doi.org/10.1023/A:1016685530312

Quevedo-Hidalgo, B., Narváez-Rincón, P. C., Pedroza-Rodríguez, A. M., & Velásquez-Lozano, M. E. (2015). Production of lignocellulolytic enzymes from floriculture residues using Pleurotus ostreatus. *Universitas Scientiarum*, *20*(1), 117–127. https://doi.org/10.11144/Javeriana.SC20-1.eple

Rashad, M. M., Abdou, H. M., Mahmoud, A. E., & Nooman, M. U. (2009). Nutritional analysis and enzyme activities of Pleurotus ostreatus cultivated on Citrus limonium and Carica papaya wastes. *Australian Journal of Basic and Applied Sciences*, *3*(4), 3352–3360.

Solomko, E. F., & Eliseeva, G. S. (1988). [Biosynthesis of vitamins B by the fungus Pleurotus ostreatus in a submerged culture]. *Prikladnaia Biokhimiia I Mikrobiologiia*, *24*(2), 164–169.

Valentão, P., Andrade, P. B., Rangel, J., Ribeiro, B., Silva, B. M., Baptista, P., & Seabra, R. M. (2005). Effect of the conservation procedure on the contents of phenolic compounds and organic acids in chanterelle (Cantharellus cibarius) mushroom. *Journal of Agricultural and Food Chemistry*, *53*(12), 4925–4931. https://doi.org/10.1021/jf0580263

WATER-BASED ELECTRONIC PAPER AS LOW-COST MULTI-COLOR SCREENS

MARTIN ROZMAN

[1] University of Maribor, Faculty of Chemistry and Chemical Engineering, Laboratory for Physical Chemistry and Chemical Thermodynamics, Maribor, Slovenia
martin0rozman@gmail.com

Abstract Electronic paper devices also known as electrochromic devices are known for their ability to change color with option to remain in certain color state even after the electrical power has been lifted. Traditional devices such as electrochromic windows used mechanisms like electrophoresis or intercalation and use special materials such as water-less electrolyte, and transparent conductive materials (TCM). As such, these devices can sometimes be relatively difficult to assemble, especially in developing countries, where such materials are harder to come by. Recently, certain improvements have been made by using alternative electrode positioning, that they do not require TCM. Presented here is a novel type of electronic paper that is recyclable, can be constructed as a monochrome or multi-color device and can be scaled accordingly to desired screen size. Presented electronic paper, is a semi-open electrochemical device, which uses pH indicator dyes and water-salt solution, combined with easily obtained sheet steel.

Keywords:
pH indicator, electronic paper, stainless steel, alternative electrode positioning, water electrolyte

University of Maribor Press

DOI https://doi.org/10.18690/um.fkkt.2.2022.8
ISBN 978-961-286-598-6

1 Introduction

Electrochromism is the phenomena, where a device can change coloration under applied electric current or potential, with additional ability to sustain newly adopted color even after the power source has been disconnected. As such, electrochromic devices (ECDs) that exhibit such qualities are known as electrochromic devices and are in principle much different compared to more traditional fast responding liquid crystal displays (LCDs) or light emitting diodes (LEDs). (Kim and Song) (Krasnov) Due to their unique behavior, they can be used in much more different applications compared to more conventional screen technologies such as smart windows and electronic paper. First electrochromic devices showed up at start of 1960s, (Kumamoto et al.) (Platt) where they had relatively limited use due high potentials requirements and slow response time. Vast improvement was shown with introduction of novel materials such as tungsten trioxide (WO3) and new sol-gel synthesis developed first by Hersh and coworkers (Hersh et al.) which promised development of novel devices and its widespread use. Shortly after, all-polymer devices were developed, which utilized polymer based transparent conductive electrodes (TCE) using poly(3,4-ethylenedioxythiophene) (PEDOT) and other polymers. (Pei et al.) (Kobayashi et al.) Due to certain materials cost, namely TCE materials, adoption of these devices was quite slow, and once the battery technology developed enough to support high potential demand of LCDs, making ECDs less interesting. Recently, several attempts have been made to avoid use of TCE, which could substantially reduce production cost of different devices, from solar cells, as well as ECDs. (Rozman et al. "Novel Geometric Approach for Photosensor Construction Based on Dye-Sensitization of Tio2 Nanoparticles on Stainless Steel") (Rozman et al. "Flexible Electrochromic Tape Using Steel Foil with Wo3 Thin Film") In a paper of Lukšič et al it was shown that it is possible to construct a device, that does not require TCE. (Rozman et al. "An Inverted Sandwich Electrochromic Device Architecture Does Not Require Optically Transparent Electrodes") In addition, presented device utilized salt-based water electrolyte, combined with pH dye that uses electrolysis as a color changing mechanism, thus avoiding the use organic solvents. By combining different pH dyes it could be possible to find a combination of coloration responses, where all the dyes share the same basic color that can be interpreted as bleached state, while the tinted state of each individual assembled cell is proportional to used pH dye. Due to already established lists of known responses for individual pH, it is easy to find a dye with appropriate

coloration response, (Khan et al.) (Van der Schueren and De Clerck) but finding the right combination of dyes to assemble such device might still be difficult. This is due to the reason, that selected pH dyes should not interact with electrolyte electrodes or each other since this could severely affect the longevity of the device. Here, we present a method on how to assemble a multi-color electrochromic device, which incorporates several electrochemical semi-cells with added dye, where semi-cells share the same electrolyte. In addition, assembled device utilizes so-called "inverted geometry", with which it is possible to avoid using TCE.

2 Materials and methods

2.1 Materials

Technical materials such as stainless steel foil type AISI 316 (TBJ Industrieteile GmbH, Germany) tissue paper (Paloma multi fun, Slovenia), insulation tape (Tesa, Germany) and microscope slide glass (IsoLab GmbH, HE-2400, Germany) have been obtained from different suppliers. Chemicals such as sodium acetate (99.9%) and ammonium sulphate (99.9%), ethanol (99.8%) along with pH dyes methyl red (99.9%), bromothymol blue (99.9%), α-naphtophtalein (99.9%) were obtained from Sigma-Aldrich.

2.2 Device assembly

Before device assembly different pH dye solutions as well as electrolytes were prepared. Two different electrolytes were prepared using sodium acetate and ammonium nitrate, both dissolved in separate measuring flask with concentration of 2.5 M. For completed 4-pixel device 2.5 M sodium acetate was used, while for individual pixel device assembled under instructions from literature (Rozman et al. "An Inverted Sandwich Electrochromic Device Architecture Does Not Require Optically Transparent Electrodes") that used methyl red dye, 2.5 M ammonium sulphate was used. Next, pH dyes were prepared by dissolving of 0.1 g of selected dye in 20 mL of ethanol each in separate beaker and stirred until the dye was dissolved. The same mass was used for all selected dyes: Bromothymol blue (BM), Methyl red (MR) and α-Naphtophtalein (AN). Each solution was then placed in its own measuring flask. For each individual dye, a paper patch measuring 5 mm by 25 mm was cut using scissors. Each patch was then soaked with the individual pH dye

and let 20 minutes to dry on air. One additional patch has been made that was first soaked in bromothymol blue and was then additionally sprinkled with dropper using α-Naphtophtalein. This 4th patch was done to be used so the device could demonstrate 4-pixel operation and was not characterized in details. After dyed paper preparation, four electrodes were cut using scissors, measuring 5 mm by 25 mm each, and they were adhered on one side with insulation tape. Each electrode was wrapped on the end of the electrode with dyed paper in such way, that an area of 5 mm by 5 mm was covered. Next, a counter electrode that measured 25 mm by 10 mm was cut. Following counter electrode preparation, working electrodes with wrapped paper were positioned on counter electrode and were then soaked with 2.5 M sodium acetate using dropper. The entire device was encapsulated into two pieces of glass measuring 35 mm x 35 mm, with excess liquid removed using paper towels. Constructed 4-pixel device measured 10 mm x 10 mm and used „inverted geometry" assembly approach.

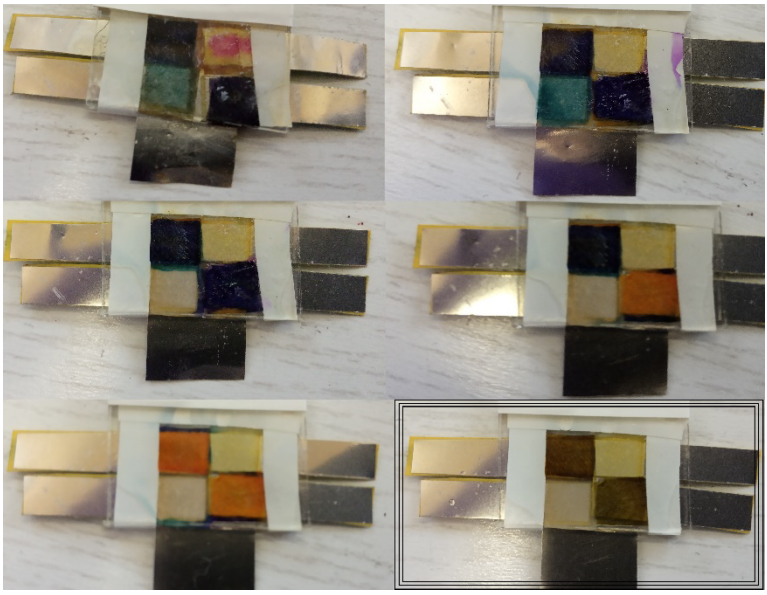

Fig. 1: Assembled water-based ECD in various coloration states. The initial color state after completed assembly is presented in lower right corner.

Surce: own.

2.3 Characterization methods

Device testing was done using variable power supply PS-302A (Voltrcraft GmbH, Germany), while electrochemical measurements were done using Autolab PGSTAT128N (Metrohm, Swtzerland) on 5 mm x 5mm devices, that represented individual pixels. Spectrophotometric measurements were done using Cary 50 (Agilent, USA) with fiber probe attachment for specular reflectance measurement.

3 Results

3.1 Cyclic voltammetry

Voltametric measurements were first done to determine behavior of stainless steel electrodes in different electrolytes. 10 cycles were done in potential window between -4 and +4 V, with starting point at 0 V with reference connected directly on counter electrode terminal. It was determined that. In fig. 2 it can be observed that both electrolytes have inertial potential window between -2 and + 2 V, suggesting that the main reaction is electrolysis of water, where on positively charged anode the water splits into oxygen and hydronium ion ($3H_2O \rightarrow 2H_3O^+ + \frac{1}{2} O_2 + 2e^-$) where on negatively charged cathode, the water splits into hydroxyl ion and hydrogen ($2H_2O + 2e^- \rightarrow 2OH^- + H_2$). The cathodic and anodic peaks for both Fig. 2a and 2b that are visible between +/-1.5 V and 2.5 V are belonging to gas reduction, either oxygen reduction or hydrogen oxidation, respectively. Only post-measurement inspection after 10 cycles showed that ammonium sulphate is more corrosive, which could be related to sulphate anions, which are more aggressive towards stainless steel compared to acetate anions. Despite having more artefacts, that were recorded during voltammetry in Fig 2a, that were due to gas build-up, the 2.5 M sodium acetate proved superior to 2.5 M ammonium sulphate. Additionally, 2.5 M ammonium sulphate had almost too high conductivity, resulting in increased current consumption while having no coloration response advantage. This can be observed as a signal cut-off below – 3 V and above + 3 V, in Fig. 3b, where potentiostat/galvanostat instrument was limited to maximum 40 mA/cm^2 to prevent excessive heating of tested device.

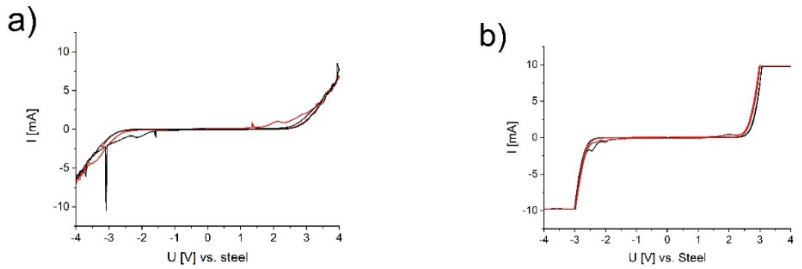

Fig. 2: Cyclic voltammetry of assembled 5 mm x 5mm device using 2.5 M sodium acetate (fig. 2a) and 2.5 M ammonium sulphate (fig. 2b) with AISI 316 stainless steel electrodes. Presented are 1st (black label) and 10th (red label) cycle.

Surce: own.

3.2 Chronoamperometry

Chronoamperometry (Fig. 3) was performed with positive pulse of + 3.5 V and negative pulse of -3.5 V both lasting for 30 s and between ach with 30 s waiting period. Potential polarity was altered after each pulse. This experiment was done to determine the conductivity and performance on two different devices, 2.5 M sodium acetate with bromothymol blue (black label) and 2.5 M ammonium sulphate with methyl red (red label) respectively. During 5 cycles of assembled device, it was observed that both devices have adequate coloration response, with no indications that any of the dyes would be affected due to electrolysis After completing 5 cycles, it was determined that sodium acetate is less corrosive to stainless steel and was thus used as a preferred electrolyte.

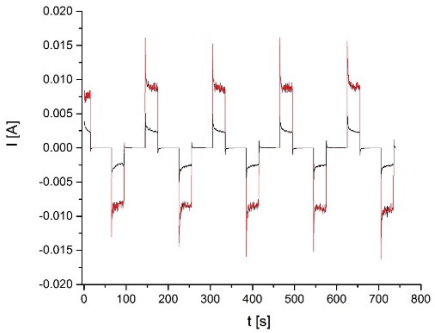

Fig. 3: Chronoamperometry of assembled 5 mm x 5mm devices. Presented are 2.5 M sodium acetate (black label) and 2.5 M ammonium sulphate (red label) 5 mm x 5 mm devices.

Surce: own.

3.3 UV-Vis reflectance spectrophotometry

UV-Vis measurements of individual pixels of assembled 4-pixel device were done to determine change of coloration. The UV-Vis measurements were performed on an assembled 4-pixel device, with spectrums recorded for three pixels that had individual color, using Bromothymol blue, Methyl red, and α-Naphtophtalein. Since the constructed device used 2.5 M sodium acetate, the pixel dyed with methyl red performed less ideally, due to Methyl red low pH required for coloration change of around 4.6, while sodium acetate has relatively high measuring around 8-9. (Rozman et al. "An Inverted Sandwich Electrochromic Device Architecture Does Not Require Optically Transparent Electrodes") Nevertheless, device was successful in obtaining all required color changes, which can be seen in Fig. 4. Both Bromothymol blue and α-Naphtophtalein are yellow in acidic media, and colored in basic media, while Methyl red has reverse response with yellow coloration in basic media and red coloration in basic media. Main coloration difference can be observed at around 600 nm for Bromothymol blue, 650 nm for α-Naphtophtalein, while for Methyl red the main difference between both states can be visible in area between 400 to 500 nm.

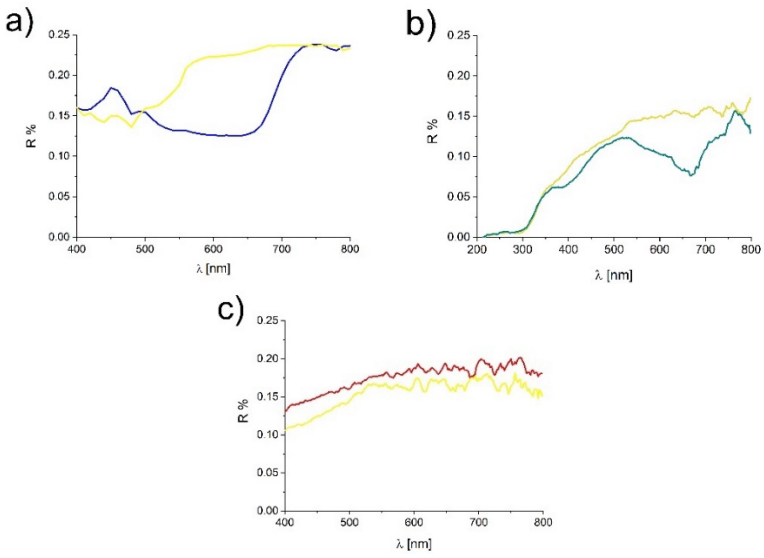

Fig. 5: UV-Vis spectrums of 4-pixel ECD device for various dyes: Bromothymol blue (fig. 4a), Methyl red (Fig. 4b), and α-Naphtophtalein (Fig 4c). For each label, appropriate visible color is used.

Surce: own.

4 Conclusions

It is possible to construct water based ECDs, that can have different coloration and could be potentially used as actual screens, and that despite marginal change in UV-Vis spectrum, coloration change of Methyl red was observable with naked eye. Results are suggesting that both Bromothymol blue and α-Naphtophtalein are most suitable for future use in development of water based multicolor screen, while Methyl red should be replaced with more suitable pH dye. In addition, such devices, could be made with relatively simple tooling and using traditional electrical engineering to connect several such devices into functional screens. Despite their relatively slow response, they could still be used in roles, where reaction time is less important, but large screen surface is desired. Such devices could be used for advertisement boards or other displays where low cost and simple development are a priority.

Acknowledgments

M. Rozman wish to thank Slovenian research agency programs P2-0046, and P1-0403. M. Rozman would also like to thank N. Cetin for support during sample preparation.

References

Hersh, H. N. et al. "Mechanism of Electrochromism in Wo3." *Applied Physics Letters*, vol. 27, no. 12, 1975, pp. 646-648, doi:10.1063/1.88346.

Khan, Muhammad Imran et al. "A Review on Ph Sensitive Materials for Sensors and Detection Methods." *Microsystem Technologies*, vol. 23, no. 10, 2017, pp. 4391-4404, doi:10.1007/s00542-017-3495-5.

Kim, Kyeong-Hyeon and Jang-Kun Song. "Technical Evolution of Liquid Crystal Displays." *NPG Asia Materials*, vol. 1, no. 1, 2009, pp. 29-36, doi:10.1038/asiamat.2009.3.

Kobayashi, Tetsuhiko et al. "Electrochemical Reactions Concerned with Electrochromism of Polyaniline Film-Coated Electrodes." *Journal of Electroanalytical Chemistry and Interfacial Electrochemistry*, vol. 177, no. 1, 1984, pp. 281-291, doi:https://doi.org/10.1016/0022-0728(84)80229-6.

Krasnov, Alexey N. "Electroluminescent Displays: History and Lessons Learned." *Displays*, vol. 24, no. 2, 2003, pp. 73-79, doi:https://doi.org/10.1016/S0141-9382(03)00015-5.

Kumamoto, J. et al. "Electrochromism (Stark Effect) in Solids Due to Isolated Absorbing Centers." *The Journal of Chemical Physics*, vol. 36, no. 11, 1962, pp. 2893-2896, doi:10.1063/1.1732398.

Pei, Qibing et al. "Electrochromic and Highly Stable Poly(3,4-Ethylenedioxythiophene) Switches between Opaque Blue-Black and Transparent Sky Blue." *Polymer*, vol. 35, no. 7, 1994, pp. 1347-1351, doi:https://doi.org/10.1016/0032-3861(94)90332-8.

Platt, John R. "Electrochromism, a Possible Change of Color Producible in Dyes by an Electric Field." *The Journal of Chemical Physics*, vol. 34, no. 3, 1961, pp. 862-863, doi:10.1063/1.1731686.

Rozman, Martin et al. "An Inverted Sandwich Electrochromic Device Architecture Does Not Require Optically Transparent Electrodes." *Advanced Materials Technologies*, vol. 4, no. 9, 2019, p. 1900389, doi:https://doi.org/10.1002/admt.201900389.

Rozman, Martin et al. "Novel Geometric Approach for Photosensor Construction Based on Dye-Sensitization of Tio2 Nanoparticles on Stainless Steel." *Sensors and Actuators A: Physical*, vol. 295, 2019, pp. 51-58, doi:https://doi.org/10.1016/j.sna.2019.05.034.

Rozman, Martin et al. "Flexible Electrochromic Tape Using Steel Foil with Wo3 Thin Film." *Electrochimica Acta*, vol. 330, 2020, p. 135329, doi:https://doi.org/10.1016/j.electacta.2019.135329.

Van der Schueren, Lien and Karen De Clerck. "Coloration and Application of Ph-Sensitive Dyes on Textile Materials." *Coloration Technology*, vol. 128, no. 2, 2012, pp. 82-90, doi:https://doi.org/10.1111/j.1478-4408.2011.00361.x.

The Influence of Different Fibres Quantity on Mechanical and Microstructural Properties of Alkali-activated Foams

Katja Traven,[1] Mark Češnovar,[1,2] Barbara Horvat,[1] Vilma Ducman[1]

[1] Slovenian National Building and Civil Engineering Institute, Ljubljana, Slovenia
katja.traven@zag.si, mark.cesnovar@zag.si, barbara.horvat@zag.si, vilma.ducman@zag.si
[2] International Postgraduate School Jožef Stefan, Ljubljana, Slovenia
mark.cesnovar@zag.si

Abstract Alkali activated foams (AAFs) were produced using electric arc furnace steel slag (EAF) and ladle furnace basic slag (LS), obtained from two metallurgical companies in Slovenia. They were activated with a mixture of sodium water glass (Na_2SiO_3) and solid NaOH and foamed with hydrogen peroxide (H2O2). Pores were stabilized with the addition of Triton as a surfactant. Four types of fibres were added to the studied mixture (polypropylene (PP), polyvinyl-alcohol (PVA), basalt (B), and glass wool (GW)) in five different quantities: 0.5, 1.0, 1.25, 1.5 and 2.0 vol % in order to additionally stabilize the structure and thus improve its mechanical properties. The results of mechanical properties showed, that compressive strength was increased in all 20 specimens, partially due to the increased density as well as to the fibre addition. Flexural strength on the other hand was the most improved in the samples where PP and PVA fibres were added. The samples with the addition of B and GW fibres on the other hand showed only small or no improvement in flexural strength in comparison to the referenced sample. Additionally, the microstructure of used fibres and selected foams was also investigated by the means of SEM analysis.

Keywords: alkali activated materials, lightweight foams, fibres, porosity, mechanical properties

University of Maribor Press

DOI https://doi.org/10.18690/um.fkkt.2.2022.9
ISBN 978-961-286-598-6

1 Introduction

Alkali activated foams (AAFs) present a promising material to be used as an insulating and/or acoustic insulation material in the building and construction area. They are produced from different aluminosilicate sources (i.e. slags, fly-ashes, calcined clays) mixed with alkali activator (different water glasses, NaOH, KOH) and foaming agent (such as H_2O_2, metal powders) (Ducman & Korat, 2016). The main advantage of AAFs production is in the lower processing temperatures (up to 100 °C) required to achieve properties similar to traditional foamed glass or ceramics, both of which are produced at highly elevated temperatures (above 900 °C). Furthermore, given their low density, good thermal properties, fire resistance and applicable mechanical properties, AAFs offer an environmentally friendly alternative to ordinary insulation materials such as aerated cement concrete, mineral wool or EPS (Abdollahnejad *et al.,* 2017).

The resulting porous hardened structure contains air voids and could thus be very fragile, therefore the additional stabilization of the structure by the addition of different types of fibres represents one possible way to improve mechanical properties (Mastali *et al.,* 2018). The main tendency found in the literature is the use of locally available fibres from natural bio-resources such as hemp (Li *et al.,* 2004), bamboo (Chen *et al.,* 2018), wood (Lin *et al.,* 1994), cotton (Alomayri *et al.,* 2013), sisal (Almeida *et al.*, 2018) and others due to their renewable and recyclable nature. The second and also very important feature of the fibres used for the AAFs production is their stability with sustainability in a highly alkaline environment when exposed to high temperatures (Abdulkareem *et al.,* 2019). For example, cellulose-based bio fibres usually decompose at temperatures around 360 °C, therefore such foams would not be applicable in the field where high-temperature resistance is required. Hence, some studies in the field of alkali-activated materials' reinforcement are focused also on the use of steel (Rashad, 2020), basalt (Mastali *et al.*, 2018), or glass fibres (Puertas *et al.,* 2006), all of which should survive elevated temperatures. Good performance was achieved also with the use of synthetic fibres such as polypropylene (Wang & Tan, 2011) or polyvinyl alcohol (Nguyen *et al.,* 2020).

In the present study, the influence of different amounts (0.5, 1.0, 1.25, 1.5 and 2.0 vol %) of polypropylene (PP), polyvinyl-alcohol (PVA), basalt (B), and glass wool (GW) fibres on mechanical properties was investigated. Further, also the microstructural incorporation of these fibres into a foamed alkali-activated matrix was assessed by means of SEM analysis.

2 Experimental

2.1 Materials and AAFs preparation

Electric arc furnace steel slag (EAF, designated as Slag A) and ladle furnace basic slag (LS, designated as Slag R), obtained from two metallurgical companies in Slovenia were used as precursors with Slag A/Slag R ratio equals 1, as already discussed in our previous study (Češnovar *et al.*, 2019). Slags were activated with the mixture of 31.5 mass % of Na_2SiO_3 Crystal 0112, 54.2 % aqueous solution with $SiO_2/Na_2O = 1.97$, produced by Tennants distribution, Ltd. and 0.5 mass % of solid NaOH produced by Donau Chemie and foamed with 2.5 mass % of H_2O_2 (30 % aqueous solution, produced by Belinka, Slovenia). Pores were stabilized with the addition of 1.5 mass % of Triton (designated as T; Triton X-100, produced by Merck, Germany) as a surfactant. Four types of fibres were separately added to the studied mixture (polypropylene (PP), polyvinyl-alcohol (PVA), basalt (B), and glass wool (GW)) in five different quantities: 0.5, 1.0, 1.25, 1.5 and 2.0 vol %. For reference also non fibred foam was produced (designated as blank). The list of prepared mixtures with the corresponding designations is shown in Table 1.

The fresh foamed pastes were poured into 20 × 20 × 80 mm^3 moulds and cured at 70 °C for 3 days. Mechanical strengths were determined 3 days after curing at a temperature of 70 °C.

Table 1: Compositions of different AFFs prepared for the investigation; where PP = polypropylene, PVA = polyvinyl alcohol, B = basalt, and GW = glass wool fibres.

Sample designation		Slag A + Slag R [g]	Na_2SiO_3 [g]	NaOH [g]	H_2O_2 [g]	T [g]	Fibres [g]
Blank		192	96	1.5	7.5	4.5	/
PP	0.5 vol %	192	96	1.5	7.5	4.5	0.53
	1.0 vol %						1.06
	1.25 vol %						1.32
	1.5 vol %						1.59
	2.0 vol %						2.12
PVA	0.5 vol %	192	96	1.5	7.5	4.5	0.42
	1.0 vol %						0.84
	1.25 vol %						1.01
	1.5 vol %						1.26
	2.0 vol %						1.68
B	0.5 vol %	192	96	1.5	7.5	4.5	0.32
	1.0 vol %						0.66
	1.25 vol %						0.82
	1.5 vol %						0.98
	2.0 vol %						1.32
GW	0.5 vol %	192	96	1.5	7.5	4.5	0.32
	1.0 vol %						0.66
	1.25 vol %						0.82
	1.5 vol %						0.98
	2.0 vol %						1.32

2.2 Fibres

For this study, four different types of fibres were used as shown in Fig. 1. They are all of elongated shapes and comprised of different sizes (approximately 11, 12, 7 and 1 cm in length for PP, PVA, B and GW, respectively) and with theoretical densities (0.94, 1.19, 2.9 and 2.9 g/cm^3 for PP, PVA, B and GW, respectively) therefore different volumetric percentage (designated as vol %) of each fibre type was added to the mixture. Fibres were added to the activator solution and mixed to obtain as homogenous fibre distribution as possible.

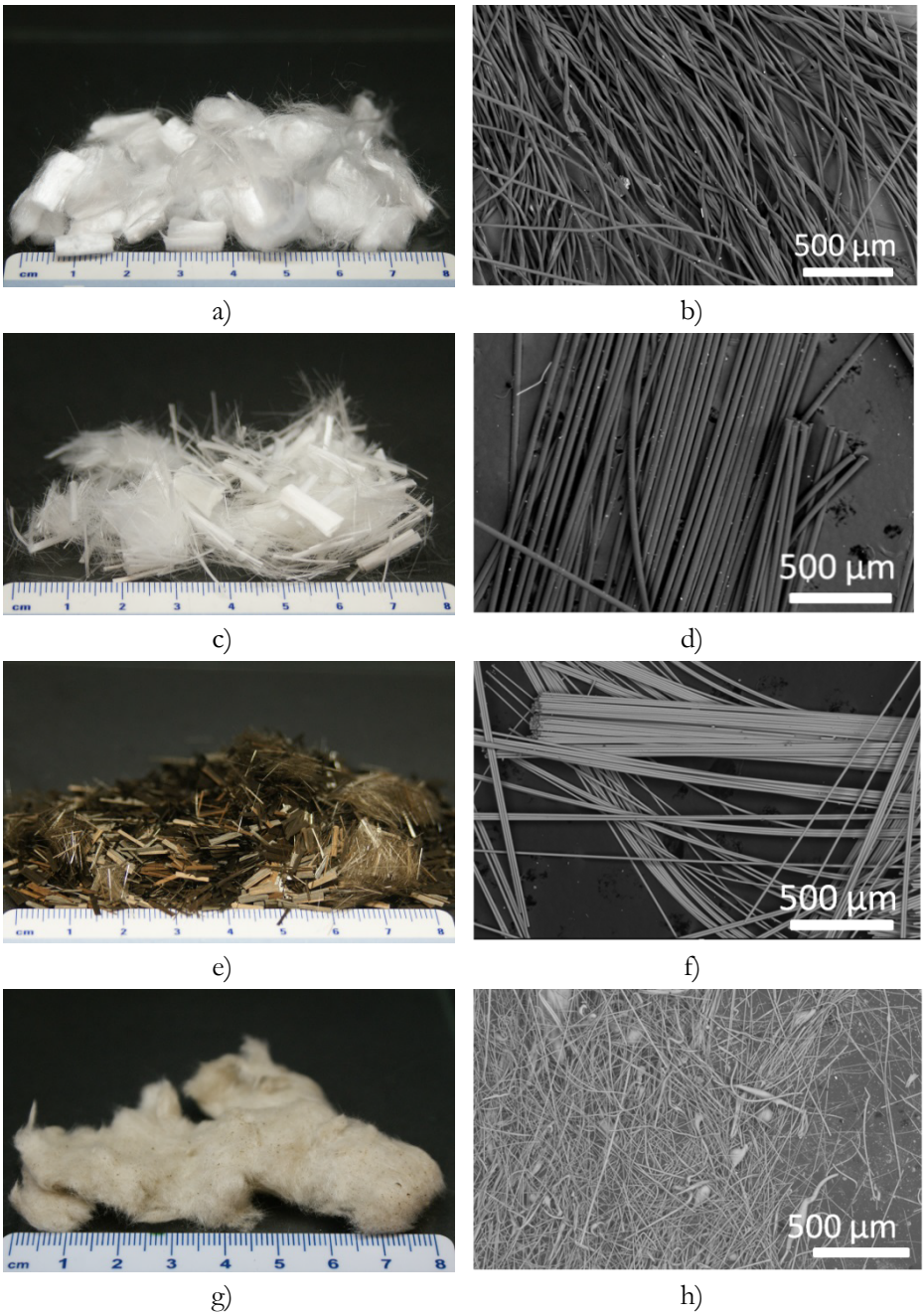

Figure 1: Macro and micro images of polypropylene (a, b), polyvinyl alcohol (c, d) basalt (e, f) and glass wool (g, h) fibres.

Source: own.

2.3 Characterization methods and instruments

The densities of all AAFs were determined by weighing the individual foams and dividing the thus determined weights by the corresponding dimensions of the specimens (i.e. so-called geometrical density).

Flexural strengths (σ_{FS}) and compressive strengths (σ_{CS}) were determined at an age of 3 days by means of a Toninorm test equipment (Toni Technik, Germany), using a force application rate of 0.005 kN/s and calculated according to equations (1) and (2).

$$\sigma_{FS} = \frac{3Fl}{2bd^2} \quad (1)$$

F – force
l – length between support span
b – width of sample
d – thickness of sample

$$\sigma_{CS} = \frac{F}{A} \quad (2)$$

F – force
A – area

The relative densities (rel. ϱ), as well as relative flexural and compressive strengths, were calculated, using the following equation (3).

$$\text{rel. } \varrho = \frac{(\varrho_0 - \varrho_x)}{\varrho_0} \quad (3)$$

ϱ_0 – density of the blank sample

ϱ_x – density of the studied fibres reinforced sample

Microstructural analysis of the fibres, as well as hardened AAFs, was performed by a JSM IT500, JEOL (Japan) with a tungsten filament cathode. Prior to SEM scanning, the samples were vacuum-dried and sputter-coated with gold.

3 Results and discussion

3.1 Mechanical properties

The absolute densities and mechanical properties of the produced AAFs are given in Table 2. Additionally, graphical presentations of the relative (with regard to the measurements of blank foam sample) densities and flexural as well as compressive strengths are shown in Fig. 2. It can be observed, that foam with no added fibres exhibit a relatively low density of 0.39 g/cm^3 and is thus also very fragile with compressive strength of only 0.21 MPa and flexural strength below detection limit. With the addition of fibres the densities are increased in most cases (with the exceptions in specimens 1.25 vol % PVA, 1.25 vol % B, 1.25 vol % GW, and 0.5 vol % B) and are in the range between 0.35 and 0.55 g/cm^3. As expected the foams with the highest density – specimens 1.0 vol % PP, 2.0 vol % PP and 1.0 vol. % PVA, exhibit also the highest compressive strengths (1.24, 1.31 and 1.20 MPa, respectively). These three specimens also showed the best development of flexural strength (0.62, 0.54 and 0.41 MPa, respectively) which could partially be assigned to the density gain and partially to the reinforcement as a consequence of fibres addition. From Fig. 2 could also be observed that all specimens regardless of the fibres type addition showed better compressive strengths. Interestingly, only 26 % density gain for specimen 2.0 vol % PP resulted in 3.3-times higher compressive strength. Further, specimens with PP and PVA addition also exhibit improved flexural strength. The samples with the addition of B and GW fibres on the other hand showed only small or no improvement in flexural strength in comparison to the referenced sample (specimen with no added fibres). Additionally, from this study, some logical correlation between fibres quantity and mechanical strength improvement was not proved, since the maximum flexural strength was reached with the addition of 1.0 vol % of PP and 2.0 vol % of PVA fibres.

Table 2: A list of the absolute densities (ϱ), flexural strengths (σFS), and compressive strengths (σCS) of all samples (n. d. = below detection limit).

		ϱ [g/cm³]	σ_{FS} [MPa]	σ_{CS} [MPa]
Blank		0.39	n. d.	0.21
PP	0.5 vol %	0.44	0.15	0.57
	1.0 vol %	0.55	0.62	1.24
	1.25 vol %	0.43	0.43	0.52
	1.5 vol %	0.42	0.34	0.41
	2.0 vol %	0.49	0.54	1.31
PVA	0.5 vol %	0.39	0.02	0.50
	1.0 vol %	0.50	0.41	1.20
	1.25 vol %	0.38	0.09	0.34
	1.5 vol %	0.41	0.13	0.36
	2.0 vol %	0.45	0.47	0.71
B	0.5 vol %	0.38	n. d.	0.39
	1.0 vol %	0.48	n. d.	0.75
	1.25 vol %	0.35	0.02	0.30
	1.5 vol %	0.40	n. d.	0.29
	2.0 vol %	0.43	0.04	0.26
GW	0.5 vol %	0.40	0.01	0.71
	1.0 vol %	0.47	n. d.	0.85
	1.25 vol %	0.35	0.01	0.41
	1.5 vol %	0.40	n. d.	0.39
	2.0 vol %	0.45	0.03	0.58

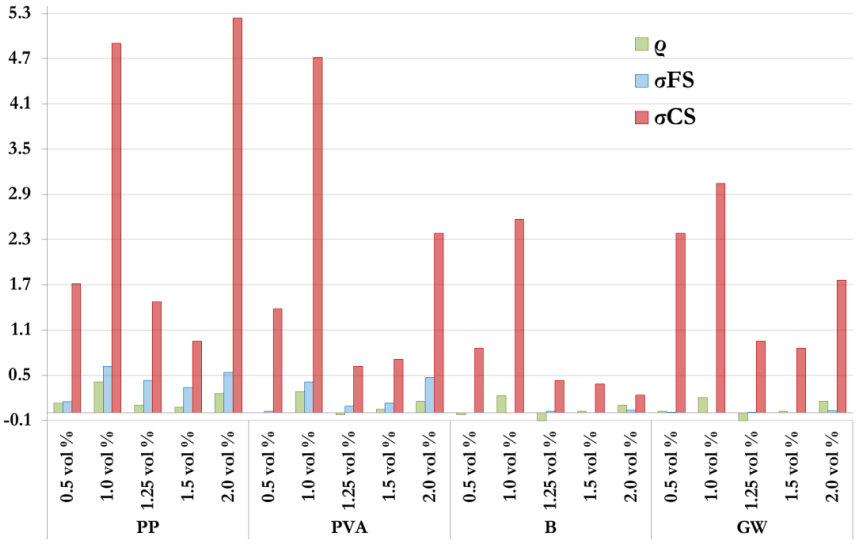

Figure 2: Graphical representation of the relative (with regard to the blank sample) densities (ϱ), flexural strengths (σ_{FS}), and compressive strengths (σ_{CS}).

Source: own.

3.2 Microstructural evaluation

The microstructures of AAFs with different fibres (in all cases the quantity of 2 vol %) and at different magnifications are presented in Figs. 3–6. SEM micrographs of PP fibre-reinforced AAFs are presented in Fig. 3. Fig. 3a shows the evenly distributed PP fibres in the alkali-activated matrix whereas Figs. 3b and 3c show a more detailed view of the boundary between the fibre and the matrix.

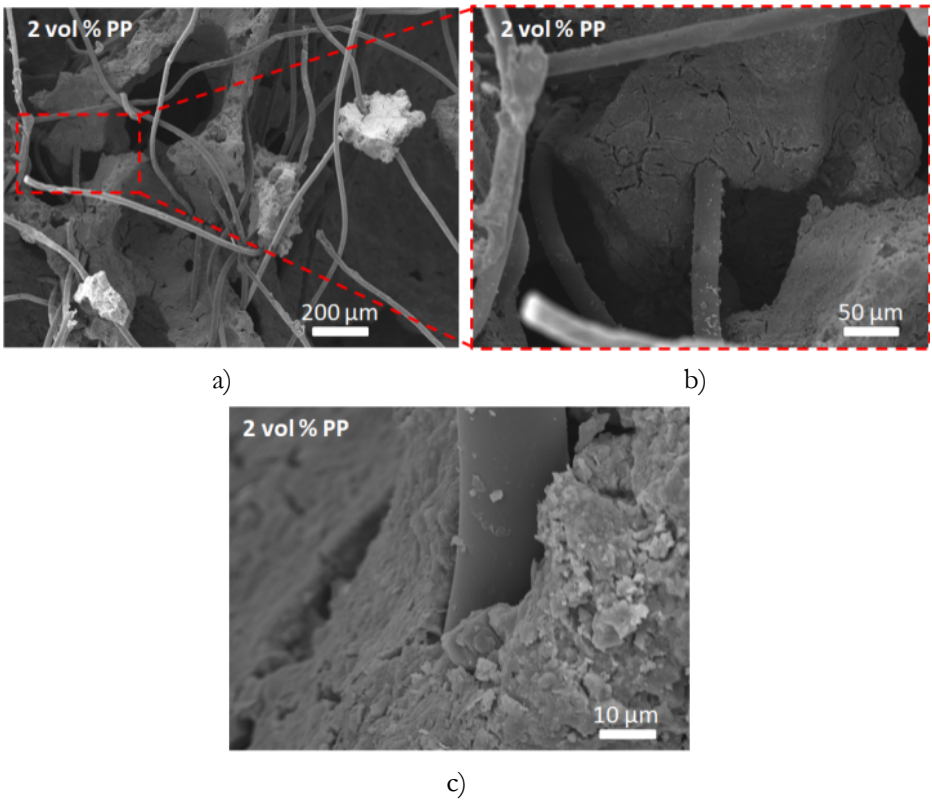

Figure 3: SEM micrographs of polypropylene reinforced AAFs (2 vol %) at different magnifications: a) PP distribution in the matrix; b) and c) boundary between a PP fibre and the matrix.
Source: own.

Similarly, also the distribution of PVA fibres is uniform in the matrix as shown in Fig. 4a and the boundary between the fibre and the matrix is presented in Fig. 4b. Additionally, as observed in Fig. 4c, PVA fibres seem to be less resistant to the highly alkaline environment and/or foaming agent in the fresh alkali-activated slurry,

therefore damages on the fibres may occur as shown in Fig. 4c. However, these damages could also contribute to the better adhesion of the fibres to the matrix resulting in better mechanical properties. After all, specimen 1.0 vol % PVA reaches one of the highest compressive and flexural strengths among studied ones.

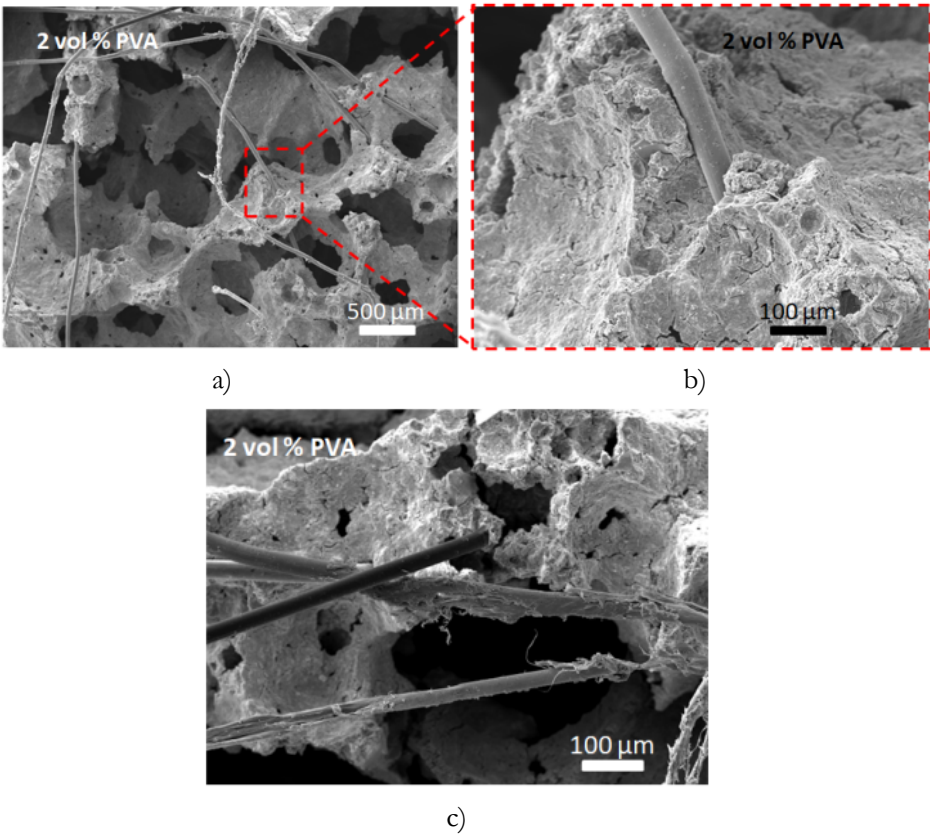

Figure 4: SEM micrographs of polyvinyl alcohol reinforced AAFs (2 vol %) at different magnifications: a) PVA distribution in the matrix; b) boundary between a PVA fibre and the matrix; c) damaged PVA fibres.

Source: own.

Fig. 5a shows the distribution of B fibres in the alkali-activated matrix. Their distribution is also quite uniform. Due to the chemical composition of the basalt fibres (alumino-silicate composition, similar to precursors) these fibres could also react with the alkaline activator and the spots seen on Fig. 5c could be a consequence of these reaction. Similar observations on SEM micrographs of B fibres after

exposure to NaOH solution were detected also by Elshafie & Whittleston (Elshafie & Whittleston, 2016). However, probably due to the more fragile nature of the B fibre, the reinforcement was not as successful as in the case of PP and PVA fibres.

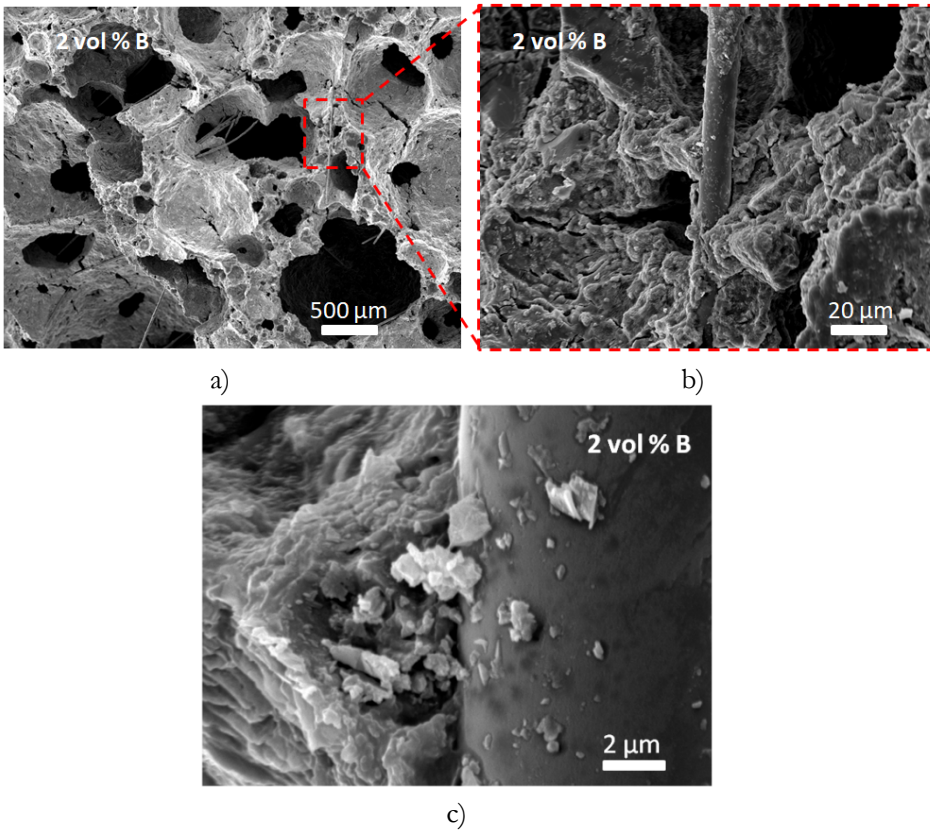

Figure 5: SEM micrographs of basalt reinforced AAFs (2 vol %) at different magnifications: a) B distribution in the matrix; b) and c) boundary between a B fibre and the matrix.
Source: own.

GW fibres are the smallest among the studied ones, therefore they are barely observed in the alkali-activated matrix as shown in Fig. 6a. Regarding to their chemical composition they are comparable to the B fibres. The advantage of such smaller fibres could be firstly in their better incorporation into the alkali-activated matrix (Figs. 6b and 6c) especially in cell and void boundaries and secondly, due to their glassy phase the dissolution in alkalis is also possible. But for the flexural strength improvement probably much higher concentrations should de added.

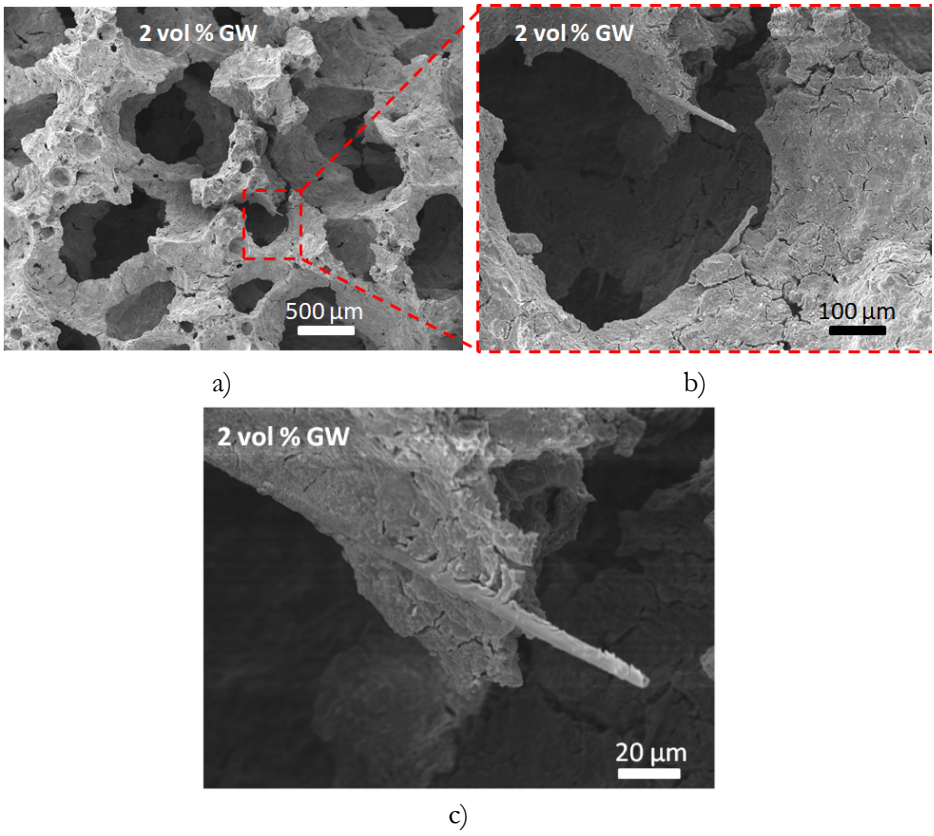

Figure 6: SEM micrographs of glass wool reinforced AAFs (2 vol %) at different magnifications: a) GW distribution in the matrix; b) and c) boundary between a GW fibre and the matrix.
Source: own.

4 Conclusions

With the aim of the mechanical properties improvement, four types of fibres (polypropylene (PP), polyvinyl-alcohol (PVA), basalt (B), and glass wool (GW)) in five different quantities (0.5, 1.0, 1.25, 1.5 and 2.0 vol %) were added to the selected alkali-activated foamed mixture. The results of mechanical properties showed, that compressive strength was increased in all 20 specimens, partially due to the increased density, which is a consequence of fibre addition. Flexural strength on the other hand was the most improved in the samples where PP and PVA fibres were added. The samples with the addition of B and GW fibres showed only small or no improvement in flexural strength in comparison to the referenced sample (specimen

with no added fibres). However, some logical correlation between fibres quantity and mechanical strength improvement was not proved in this study. The best performance in terms of mechanical properties was achieved in the case of the specimen where 2.0 vol % of PP fibres was added. SEM micrographs revealed, that in most cases the fibres are uniformly distributed. In the case of PVA fibres also some damaged fibres were observed which could contribute to better adhesion and therefore improved mechanical properties.

Acknowledgements

Development of AAFs is part of the ERA-MIN FLOW project which has been financed by the Ministry of education, science, and sport (acronym: MIZS) under grant agreement No. C 3330-18-252010.

Project No. C3330-17-529032 "Raziskovalci-2.0-ZAG-529032" was granted by Ministry of Education, Science and Sport of the Republic of Slovenia. The investment is co-financed by the Republic of Slovenia, Ministry of Education, Science and Sport and the European Regional Development Fund.

References

Abdollahnejad, Z., Miraldo, S., Pacheco-Torgal, F., and Barroso, A. J. 2017. "Cost-Efficient One-Part Alkali-Activated Mortars with Low Global Warming Potential for Floor Heating Systems Applications." *European Journal of Environmental and Civil Engineering* 21, no. 4: 412-429. https://dx.doi.org/10.1080/19648189.2015.1125392.

Abdulkareem, M., Havukainen, J., and Horttanainen M. 2019. "How Environmentally Sustainable Are Fibre Reinforced Alkali-Activated Concretes?" *Journal of Cleaner Production* 236. https://dx.doi.org/10.1016/j.jclepro.2019.07.076.

Almeida, F. V., Cunha, M. C. F., Tiago M., and Cristelo, N. 2018. "Indirect Tensile Behaviour of Fibre Reinforced Alkali-Activated Composites." *Fibres* 6, no. 2. https://dx.doi.org/10.3390/fib6020030.

Alomayri, T., Shaikh, F. U. A., and Low, I. M. 2013. "Characterisation of Cotton Fibre-Reinforced Geopolymer Composites." *Composites Part B-Engineering* 50: 1-6. https://dx.doi.org/10.1016/j.compositesb.2013.01.013.

Chen, H., Zhang, W., Wang, X., Wang, H., Wu, Y., Zhong, T., and Fei B. 2018. "Effect of Alkali Treatment on Wettability and Thermal Stability of Individual Bamboo Fibres." *Journal of Wood Science* 64, no. 4: 398-405. https://dx.doi.org/10.1007/s10086-018-1713-0.

Elshafie, S., and Whittleston, G. 2016. "Evaluating the efficiency of basalt and glass fibres on resisting the alkaline, acid and thermal environments." *American Journal of Materials Science* 6(1): 19-34. doi:10.5923/j.materials.20160601.02.

Češnovar, M., Traven, K., Horvat, B., and Ducman V. 2019. "The Potential of Ladle Slag and Electric Arc Furnace Slag Use in Synthesizing Alkali Activated Materials; the Influence of Curing on Mechanical Properties." *Materials* 12, no. 7: 1-18. https://dx.doi.org/https://doi.org/10.3390/ma12071173.

Ducman, V., and Korat, L. 2016. "Characterization of Geopolymer Fly-Ash Based Foams Obtained with the Addition of Al Powder or H_2O_2 as Foaming Agents." *Materials Characterization* 113: 207-213. https://dx.doi.org/10.1016/j.matchar.2016.01.019.

Li, Z. J., Wang, L. J., and Wang, X. G. 2004. "Compressive and Flexural Properties of Hemp Fibre Reinforced Concrete." *Fibres and Polymers* 5, no. 3: 187-197. https://dx.doi.org/10.1007/bf02902998.

Lin, X., Silsbee, M. R., Roy, D. M., Kessler, K., and Blankenhorn P. R. 1994. "Approaches to Improve the Properties of Wood Fibre-Reinforced Cementitious Composites." *Cement and Concrete Research* 24, no. 8: 1558-1566. https://dx.doi.org/10.1016/0008-8846(94)90170-8.

Mastali, M., Kinnunen, P., Isomoisio, H., Karhu, M., and Illikainen M. 2018. "Mechanical and Acoustic Properties of Fibre-Reinforced Alkali-Activated Slag Foam Concretes Containing Lightweight Structural Aggregates." *Construction and Building Materials* 187: 371-381. https://dx.doi.org/10.1016/j.conbuildmat.2018.07.228.

Nguyen, H., Kaas, A., Kinnunen, P., Carvelli, V., Monticelli, C., Yliniemi, J., and Illikainen M. 2020. "Fibre Reinforced Alkali-Activated Stone Wool Composites Fabricated by Hot-Pressing Technique." *Materials & Design* 186. https://dx.doi.org/10.1016/j.matdes.2019.108315.

Puertas, F., Gil-Maroto, A., Palacios, M., and Amat T. 2006. "Alkali-Activated Slag Mortars Reinforced with Ar Glassfibre. Performance and Properties." *Materiales De Construccion* 56, no. 283: 79-90.

Rashad, A. M. 2020. "Effect of Steel Fibres on Geopolymer Properties - the Best Synopsis for Civil Engineer." *Construction and Building Materials* 246. https://dx.doi.org/10.1016/j.conbuildmat.2020.118534.

Wang, L. J., and Tan, X. Q. 2011. "Preparation and Properties of Alkali Activated Foam Cement Reinforced with Polypropylene Fibres." *Journal of Wuhan University of Technology-Mater. Sci. Ed.* 26, no. 5: 960-964. https://dx.doi.org/10.1007/s11595-011-0345-7.

Analysis of the Possibilities for Energy Recovery in WWTP

Rayka K. Vladova, Natasha Vaklieva-Bancheva

Institute of Chemical Engineering, Bulgarian Academy of Sciences, Akad. G. Bontchev, Sofia, Bulgaria
r.vladova@iche.bas.bg

Abstract In recent years, there has been increasing talk of improving energy efficiency and the ability to reduce greenhouse gases in wastewater treatment plants. This necessitates exploring the possibilities for reducing energy costs and the possibilities for obtaining energy from wastewater. In the present study, an analysis of the energy consumed at different stages of wastewater treatment in a municipal WWTP in the Republic of Bulgaria is made, and the average monthly consumption of electricity required for the treatment of one cubic meter of wastewater is estimated. Based on the collected and analyzed data, an assessment was made of the possibilities for energy recovery from dry matter from sludge, by combustion and anaerobic digestion. The obtained results allow for the reconstruction of a facility and the use of the hitherto unused energy potential contained in the sludge.

Keywords: anaerobic wastewater treatment, cost analysis, energy efficiency, energy recovery, circular economy.

University of Maribor Press

DOI https://doi.org/10.18690/um.fkkt.2.2022.10
ISBN 978-961-286-598-6

1 Introduction

Wastewater treatment plants are facilities designed to meet certain standards regarding the quality of treated water. In recent years, new stricter requirements have been imposed on the quality of discharged water, as well as the mandatory biological treatment of wastewater in agglomerates over 2000 inhabitants for the countries of the European Union and removal of nutrients nitrogen and phosphorus in wastewater treatment from settlements with more 10,000 population equivalents (Council Directive No. 91/271/CEE) implies higher costs in their treatment. One of the main operating costs in the WWTP is the energy consumption both in the wastewater treatment and the need for electricity in the dewatering of sludge. This necessitates the need to assess the energy efficiency of these facilities of national importance and to study the possibilities for reducing the consumed energy, as well as the possibilities for restoring such.

Globally, WWTPs consume between 3-5 % of energy (McCarty et al., 2011), making them one of the largest energy consumers managed by municipalities. Different wastewater treatment technologies have different energy costs. WWTP energy consumption depends on the degree of wastewater pollution, the location of the installation, the equipment, as well as the aeration processes. To estimate the energy consumption in different treatment plants Longo et al. 2016 offer key energy efficiency indicators (KPIs) using data available at each treatment plant. Fraia et al. 2018 define an indicator that connects the energy consumption in a treatment plant with the input quantities of BOD. The study defines different performance classes, linking the indicators of specific energy consumption with the parameters for the efficiency of pollutant removal.

One of the ways to reduce energy consumption is to optimize the work and improve the energy efficiency of production systems, as well as the search for opportunities for energy production. Reducing energy consumption in wastewater treatment processes would improve their energy efficiency and, last but not least, lead to a reduction in carbon emissions. The optimization of energy costs could be considered in two directions:

- replacement of the available equipment with more modern one, whose energy consumption should be minimal;

- the possibilities to recover energy from waste products obtained as a result of wastewater treatment.

A study of each phase of the technological scheme of a municipal wastewater treatment plant (Panepinto et al. 2016) offers a multi-stage methodology for assessing the energy aspects of wastewater treatment. The energy balance made makes it possible to make some suggestions for optimizing the work processes in the plant. Indicators for the total energy consumption per m3 are calculated in relation to the amount of pollutants removed. Possibilities for reducing energy consumption are also being explored by Chae K. & Kang J. 2013, offering a methodology for assessing energy independence through appropriate renewable energy technologies using different types of photovoltaics.

The aim of the present study is to analyze the electricity consumed at the individual stages of treatment, as well as to analyze the average monthly consumption of electricity required for the treatment of one cubic meter of wastewater. The paper analyzes the possibilities for energy recovery from dry sludge using different technologies.

2 Methodology

The main stages of wastewater treatment are mechanical treatment, biological treatment and the last stage related to sludge treatment. Each of these stages has a different energy consumption, depending on the amount of treated water, the technology used, as well as the degree of pollution. The quality of treated wastewater is characterized by key indicators, such as the amount of removed organic pollutants, removed suspended solids, chemical and biological oxygen demand, as well as the content of nitrogen and phosphorus, all of which must meet certain standards. The availability of these data, as well as the assessment of total electricity consumption, helps to develop energy performance indicators for wastewater treatment (Longo et al. 2016). Data for the calculation of these indicators are available at each treatment plant. They are related to the total electricity consumption in relation to the volume of treated wastewater (KPL_V), the electricity consumption in relation to the population equivalent (KPL_{RE}), as well as the amount of consumed electricity for

the removed COD (KPL_{COD}). The most commonly used indicator expresses energy consumption in relation to the amount of treated water.

$$KPL_V = \frac{EE}{V}\left(\frac{kWh}{m^3}\right) \quad (1)$$

$$KPL_{PE} = \frac{EE}{PE}\left(\frac{kWh}{PE\ year}\right) \quad (2)$$

$$KPL_{COD} = \frac{EE}{COD\ removed}\left(\frac{kWh}{kg\ removed\ COD}\right) \quad (3)$$

Based on this scientific development, an assessment was made of the energy efficiency at each stage in the object of study. The obtained results are summarized in fig. 1. Data on energy consumption for a period of one year relative to the volume of treated water are used. The data are based on daily records made in a municipal WWTP designed for 70,000 population equivalents, with average daily capacity of 13,400 m³. The average amount of energy required for the treatment of one m³ of wastewater after the calculations is 0.188 kWh/m³.

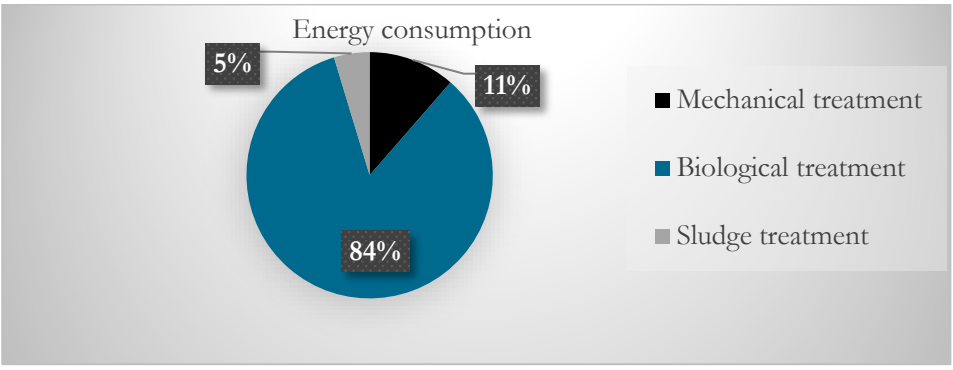

Figure 1: Energy consumption at different stages of treatment

Source: own.

As can be seen from Fig. 1 with the highest energy costs is the stage of biological treatment. At this stage, the wastewater enters bio pools (2 pieces), where denitrification is performed with the help of activated sludge. The activated sludge method used includes oxygen-free nitrogen removal zones. Each bio-pool has three corridors - the first is for pre-denitrification, without aeration, and the other two are aerated, also the free phosphorus is removed in the facility. Passing through the bio-

pool, the activated sludge is separated from the treated water into secondary radial precipitators. The wastewater treated in this way is discharged into a water intake, and the activated sludge is returned to the process as recirculated by a pump station for recycling sludge. After aerobic stabilization in the bioreactor and the associated facilities for compaction and dewatering of the sludge in a sludge compactor, the excess activated sludge is removed to drying fields for natural dewatering without the use of special equipment. The reason for the higher energy consumption at this stage is due to the removal of both organic pollutants and the biogenic elements nitrogen and phosphorus.

3 Technologies for energy recovery in WWTP

The analysis of the energy consumption in the WWTP inevitably leads to the study of the possibilities for energy recovery. Over the last decade, the perception of WWTPs has changed and wastewater is considered an energy resource for energy recovery. The energy contained in organic pollutants could be transformed into electrical and thermal, through appropriate technologies. The main source of organic energy in the WWTP is generated as a waste product as a result of wastewater treatment and these are sludge. In many countries, energy recovery technology uses the combustion of sludge as a result of which energy is released. This process is performed at a high temperature to eliminate harmful gas emissions. The amount of energy obtained as a result of combustion depends on the content of organic matter. The moisture content of the sludge as well as the drying methods, in which the treatment costs increase, also have a significant influence. The advantages of this technology is that in addition to energy production, the amount of sludge that must be disposed of is reduced.

Another possibility is the recovery of energy is through the production of biogas. This technology is one of the most common and is suitable for medium and large treatment plants, where anaerobic wastewater treatment is performed using anaerobic microorganisms at temperatures typical of mesophilic microorganisms 33-37 ° C. As a result of their activity, organic substances are decomposed into biogas, containing mainly methane 55-65%, carbon dioxide 30-40%, water and others. The use of the obtained biogas as recovered energy also has some challenges due to the presence of many impurities that must be removed before the biogas can be used.

Another disadvantage of this technology is its not very high energy value (Appels et al., 2008). All this would require additional capital expenditures.

The sludge from the municipal treatment plants is also used for fertilization of agricultural lands, after preliminary analysis, for the presence of harmful substances. Unfortunately, there are many countries that do not use sludge, and dispose of it without further processing.

In Bulgaria, a large part of this waste product is deposited about 90%, the rest is used for land reclamation and biogas production after anaerobic digestion. In order to determine the unused energy potential contained in the sewage sludge in this work is have made an analysis of the possibilities for energy recovery, through the two most common technologies, combustion and energy production from biogas.

3.1 Data

The data for this study summarize the operation of the WWTP and the amount of sludge produced for a period of six years after the reconstruction of the WWTP. The records are summarized for each of the years studied. Table 1 presents the total content of generated sludge in the facility, as well as the amount of dry sludge for the respective year. It is necessary to mention that in the studied WWTP the sludge is deposited in drying fields without additional energy being used for its dehydration, renewable solar energy is used for drying. The dry matter content varies in the range of 24-50% in different years, and the average for the study period is about 36%. This would require minimal amounts of energy in cases where the sludge incineration method is applied. The present study does not consider the amount of energy required to be used in cases of high moisture content to meet the combustion requirement.

Table 1: Quantities of landfilled sludge.

year	dry basis/t	total/t
2014	252.52	979.6
2015	292.56	953
2016	260.46	712.54
2017	219.87	705.48
2018	210.09	388.98
2019	134.39	480.34

4 Results

For the purposes of the study, is used data from Vipin Singh et al. 2020, which explores the energy potential of sludge through combustion and anaerobic digestion. The paper describes that the average potential for energy recovery by incineration of sewage sludge is in the range of about 555-1068 kWh / ton of dry sludge, while the potential for energy generation as a result of biogas production is significantly lower from 315-608 kWh / ton dry sludge. Based on these data, for the purposes of the analysis, the lowest energy values were used for the production of energy from dry matter in both technologies.

After the calculations and the analysis of the data, results are presented for the amount of energy that could be recovered through sludge incineration technology. Fig. 2. The average amount of energy recovered in one year would be ~ 126,715 kWh.

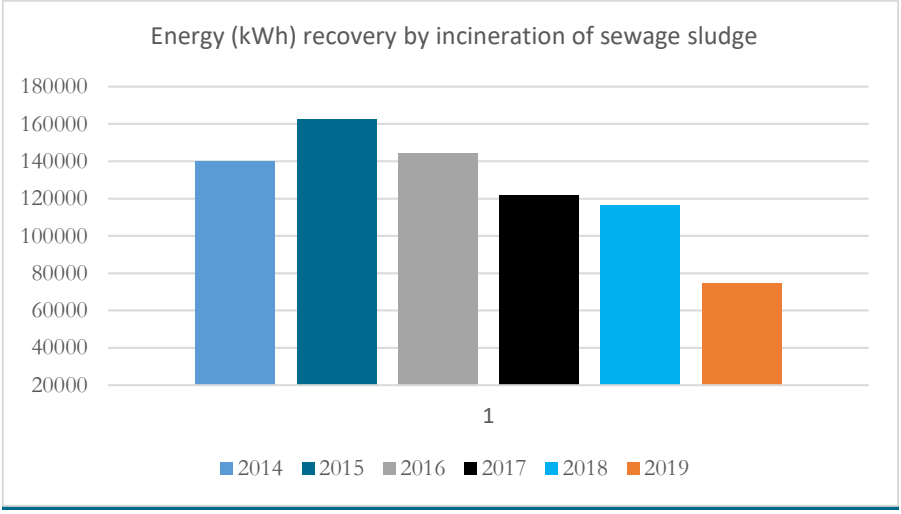

Figure 2: Energy recovery potential of sludge using incineration plants
Source: own.

Or the amount of energy that can be recovered by burning one ton of dry sludge is 92.5 kWh.

Presented results for the amount of energy that could be recovered as a result of biogas production are shown in fig. 3. The average amount of recovered energy for one year in the production of biogas is ~ 71 920 kWh or 52.5 kWh of energy per ton of dry matter.

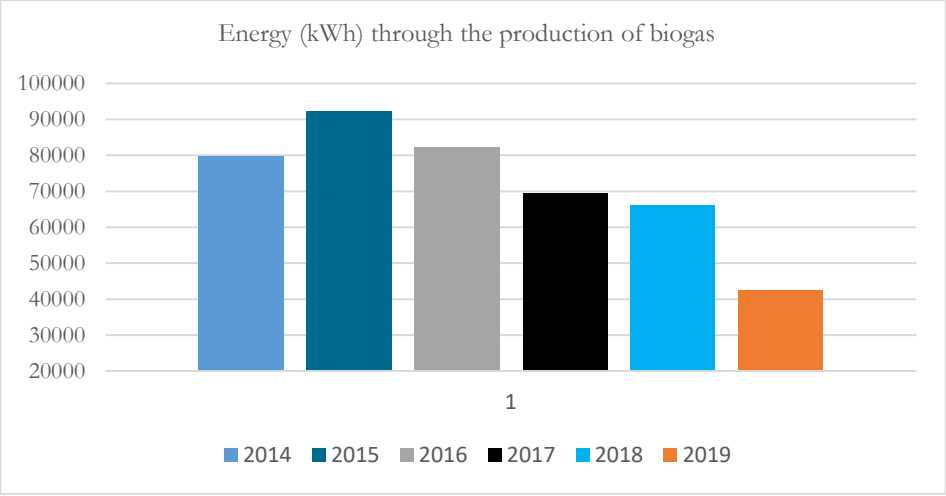

Figure 3: Energy potential of sludge using biogas production
Source: own.

It should be mentioned that these are the minimum amounts of energy that could be recovered. It is also important to say that two methane tanks and a gas holder have been built on the territory of the respective treatment plant, which have not been put into operation at this time. This would reduce the investment costs for reconstruction, and thus the choice of appropriate energy recovery technology.

5 Conclusions

In this study, an analysis was made of the energy consumption as well as the average amount of energy required for the treatment of one m3 of wastewater. Possibilities for energy recovery using sludge as a renewable energy resource were analyzed. The data used for the analysis are based on real records from the WWTP after main reconstruction, in which the removal of nitrogen and phosphorus is carried out. The study provides an opportunity to assess the benefits of modernization and choice of technology for energy recovery from wastewater. The minimum amounts of energy

that can be recovered from one ton of dry organic matter by combustion and anaerobic digestion are 92.5 kWh, respectively and 52.5 kWh. The choice of which of these technologies would be more suitable for the respective site is a choice of management decision, which must take into account an analysis of investment costs.

Acknowledgments

This work has been supported by the Bulgarian Ministry of Education and Science under the National Research Programme "Young scientists and postdoctoral students" approved by DCM # 577 /17.08.2018.

This work was realized thanks to the data provided by the WWTP in Kyustendil, Republic of Bulgaria.

References

Appels L., Baeyens J., Degreve J., Dewil R. (2008). Principles and potential of the anaerobic digestion of waste-activated sludge. *Progress in energy and combustion science*, *34(6),* 755-781. doi: 10.1016/j.pecs.2008.06.002

Council Directive No. 91/271/CEE, 21 May 1991, regarding urban wastewater treatment.

Chae K., Kang J. (2013). Estimating the energy independence of a municipal wastewater treatment plant incorporating green energy resources. *Energy Conversion and Management, 75*, 664-672, doi: 10.1016/j.enconman.2013.08.028

Fraia, S. Di., Massarotti, N., Vanoli L. (2018). A novel energy assessment of urban wastewater treatment plants. *Energy Conversion and Management. 163*, 304-313, doi:10.1016/j.enconman.2018.02.058

Longo S, d'Antoni B.M., Bongards M., Chaparro A., Cronrath A., Fatone F., Lema M.J., Mauricio-Iglesiasa M., Soarese A., Hospido A.(2016). Monitoring and diagnosis of energy consumption in wastewater treatment plants. A state of the art and proposals for improvement. A*ppl Energy, 179,* 1251–1268. doi: 10.1016/j.apenergy.2016.07.043

McCarty, P.L., Bae, J., Kim, J. (2011). Domestic wastewater treatment as a net energy producerdcan this be achieved? *Environ. Sci. Technol. 45*, 7100-7106. doi: 10.1021/es2014264

Panepinto D., Fiore S., Zappone M., Genon G., Meucci L. (2016). Evaluation of the energy efficiency of a large wastewater treatment plant in Italy. Appl Energy,161, 404-411. doi: 10.1016/j.apenergy.2015.10.027

Vipin, S., Phuleria C. H., Chandel K. M. (2020). Estimation of energy recovery potential of sewage sludge in India: Waste to watt approach. *Journal of Cleaner Production, 276*, 122538, doi: 10.1016/j.jclepro.2020.122538

SUSTAINABILITY PROFIT GAINED BY THE OPTIMIZED CLAMPED BEAMS

TOMAŽ ŽULA, STOJAN KRAVANJA, PRIMOŽ JELUŠIČ

University of Maribor, Faculty of Civil Engineering, Transportation Engineering and Architecture, Maribor, Slovenia
tomaz.zula@um.si, stojan.kravanja@um.si, primoz.jelusic@um.si

Abstract The paper presents the optimization of the sustainability profit achieved by the production of clamped beams in civil engineering. It proposes to design a range of beams using three different material alternatives: structural steel, reinforced concrete and glulam. For this reason, three optimization models of beams are developed for the three materials. In addition, two different objectives are defined for each material alternative: for the economic profit and for the sustainability profit (which includes the eco costs of global warming). The proposed objectives are subject to the design, resistance and deflection constraints of the clamped beam, which are determined in accordance with the specifications of Eurocodes 2, 3 and 5. The mixed-integer non-linear programming (MINLP) approach is used to find most advantageous material alternative of the beams. GAMS /Dicopt is used. The numerical example presented at the end of the paper clearly shows that reinforced concrete beams have the highest economic and sustainability profit.

Keywords:
sustainability profit, GHG emissions, optimization, mixed-integer non-linear programming, MINLP

University of Maribor Press

DOI https://doi.org/10.18690/um.fkkt.2.2022.11
ISBN 978-961-286-598-6

1 Introduction

The paper deals with the optimization of the sustainability profit achieved by the production of clamped beams in the area of civil engineering. In this case, the sustainability profit is a sum of the economic profit and eco costs of global warming. It is assumed that a number of beams are designed using 3 different material alternatives: glulam, structural steel and reinforced concrete. The objective of this paper is to find the optimal design of the clamped beam subjected to the highest sustainability and economic profit, performed by mixed- integer non-linear programing approach.

In the areas of sustainability and optimization, various optimization methods and different goals have been proposed. For example, Zaforteza et al. (2009) reported the optimization of CO_2 emissions and production costs of concrete constructions using simulated annealing (SA). Camp and Huq (2013) proposed the calculation of optimal concrete frames with a hybrid big bang-big crunch algorithm (BB-BC), where the objective was to minimize the total cost or CO_2 emissions. Alonso and Berdasco (2015) presented the carbon footprint calculations of some wood products. Li et al. (2017) introduced a topology optimization of welded box girders with minimal greenhouse gas emissions, where an improved ground structure method (IGSM) was applied.

2 MINLP model formulation

Since the problem of clamped beam is the non-linear discrete-continuous optimization problem, the MINLP is used for the solution and can be formulated as follows:

$$\begin{gathered}
\min \ sep = f(\mathbf{x},\mathbf{y}) \\
\text{subjected to:} \quad m_s(\mathbf{x},\mathbf{y}) \leq 0 \quad s \in S \\
\mathbf{x} \in X = \{\mathbf{x} \in R^n: \ \mathbf{x}^{LO} \leq \mathbf{x} \leq \mathbf{x}^{UP}\} \\
\mathbf{y} \in Y = \{0,1\}^m
\end{gathered}$$

where **x** are the continuous variables and **y** are the discrete (0, 1) variables. Function *sep* is the objective function for the economic profit and for the sustainability profit (which includes eco costs of global warming). m_s (**x**,**y**) represents the design, resistance and deformation constraints.

3 Numerical example

The example shows the optimization of 800 equal clamped beams. Each beam is 8.0 meters long, subjected to the combined effect of the dead-weight, the permanent load of 9.0 kN/m (g) and the imposed variable load of 12.0 kN/m (q), see Fig. 1.

It is proposed to make each clamped beam from three different material alternatives: glulam, structural steel and reinforced concrete. At this point, the comparison and competitiveness between these 3 beam materials has been investigated for different material and dimensional variants and for 2 different objectives, i.e. for the optimization of sustainability and economic profit.

For extensive and time-consuming optimization problems, we usually use the program MipSyn (Kravanja, 2010). Since the optimization problem of the clamped beam is a single discrete non-linear problem, Dicopt (Grossmann, 2002) was chosen for the application. 6 different optimization models for the clamped beam (CLAMBOPT) were modeled as a combination between 3 various materials (wood, steel and concrete) and 2 various objective functions. GAMS (General Algebraic Modelling System), (Brooke et al., 1988), was employed for modeling and input/output interpretations. Each model consists of the input data (scalars), variables, and the objective function, which is subjected to the design, loading and dimensionig (in)equality constraints. These constraints were defined in accordance with the Eurocode standards: Eurocode 2 (2004) for concrete, Eurocode 3 (2005) for steel and Eurocode 5 (2004) for wood. The clamped beams were tested for bending moment, shear force and lateral torsional buckling. Vertical deflections were also checked.

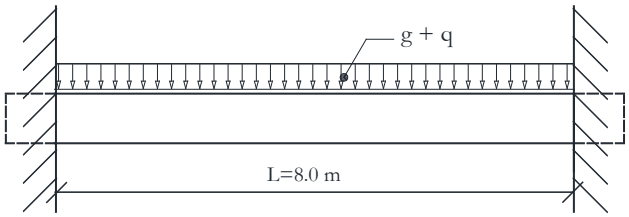

Figure 1: Clamped beam.

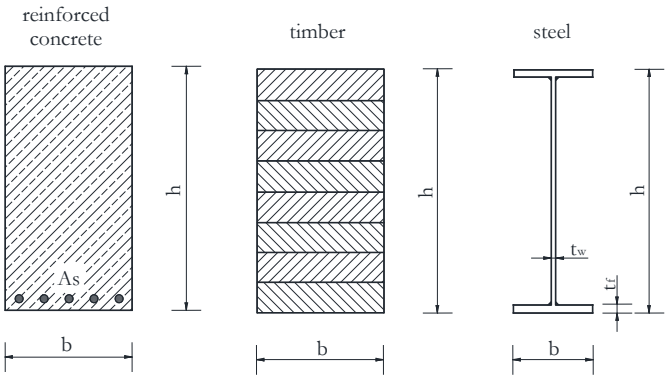

Figure 2: Cross sections of the clamped beam.

The clamped girder super-structure contains of 3 different materials. The glulam girder super-structure comprises 131 rounded dimensional variations for the section height and 101 different rounded dimensional variation for the section width. The steel girder super-structure comprises eight different dimensional variations of standard steel plate thicknesses for flanges and webs separately, 1051 rounded dimensional variations for flange width and 1301 rounded dimensional variations for web height and three different steel grades. In addition, thirteen standard steel reinforcing bars, seven different concrete grades 101 rounded dimension variants for the section width (rounding up to whole centimeters) and 131 rounded dimension variants for the section height are involved in the concrete girder super-structure.

The specified material and dimension variants (binary variables) result in 13 231 design variants for the wooden beam, 262 531 392 different design variants for the steel beam and 1 204 021 different design variants for the concrete beam.

2 different objective functions were proposed for 2 different defined criteria. The 1st criterion of optimization comprises the maximization of the economic profit (P_{EP} [€]) of 800 identical beam structures. The economic profit is calculated as the sum of the self-manufacturing material, labor cost, selling price and overhead cost. The objective function was defined separately for 3 different materials, see Eq. (1). N is a number of clamped beams (N = 800), C_{SP} [€] is the sales price of a clamped beam, C_{MPj} [€/kg] stands for the material unit prices of ($j \in J$: glulam, protection and impregnation paint for the wood beam; structural steel, gas consumption, electrodes and anticorrosion-resistant paint for the steel beam; and formwork slab-panels, concrete and steel reinforcing bars for the concrete beam). ϱ_j [kg/m^3] is the corresponding unit mass and V_j [m^3] is the volume. While C_{LCi} stands for the labor cost per hour [€/h], t_i [h] is the time required for ($i \in I$: painting and impregnating of the glulam; welding, cutting and painting the steel beam; and curing, vibrating and placing the concrete, placing and cutting the reinforcement, and paneling the concrete beam), and f_O is an indirect overhead cost factor (f_O = 2). For more details on the cost factors used in the economic objective function, see (Jelušič, 2017) and (Kravanja, 2017).

$$\max P_{EP} = N \cdot \left(C_{SP} - C_{MPj} \cdot \varrho_j \cdot V_j - C_{LCi} \cdot t_i \cdot f_O \right) \tag{1}$$

The 2nd criterion is to maximize the sustainability profit (P_{SP} [€]), which is calculated for 800 beams as the sum of the economic profit and the eco costs of global warming caused by the beam production (EVR, 2018). The objective function was defined separately for 3 materials, see Eq. (2). C_W (€/kg CO_2 eq.) is a price of global warming, 0.116 €/kg CO_2 eq. (EVR, 2018), ϱ_m [kg/m^3] and V_m [m^3] are the corresponding units of mass and volume respectively, and f_{CO2m} is the emission factor of the carbon footprint ($m \in M$; for the glulam beam, steel and reinforced concrete beam, respectively). The carbon footprint emission factor used in the study is 0.11–0.16 kg CO_2 equivalent/kg for concrete, 2.43 kg CO_2 equivalent/kg for steel reinforcing bars, 0.69 kg CO_2 equivalent/kg for glulam and 1.72 kg CO_2 equivalent/kg for steel.

$$\max P_{SP} = P_{EP} + N \cdot \left(-C_W \cdot f_{CO2m} \cdot \varrho_m \cdot V_m \right) \tag{2}$$

Table 1: Results of the clamped beam optimizations.

Criterion		Reinforced Concrete C 50/60	Laminated timber GL24h	Steel S 235
1.*	**Economic profit (€)**	**624,968**	**292,227**	**94,211**
	b (cm)	32.0	41.0	27.9
	h (cm)	45.0	41.0	41.9
2.*	**Sustainability profit (€)**	**540,531**	**252,734**	**27,761**
	b (cm)	32.0	41.0	27.9
	h (cm)	45.0	41.0	43.9

* 1. Economic profit; 2. Sustainability profit

Table 1 shows the optimization results for 2 different objective functions and 3 different materials. The results show that concrete beams have the highest economic and sustainability profit, while steel beams have the worst performance for all criteria.

4 Conclusion

The paper presents the optimization of the sustainability profit achived by the production of clamped beams in the area of civil engineering. The optimal solutions are calculated based on 2 different objective functions, i.e. economic profit and sustainability profit. The optimizations of the beam alternatives are performed by the MINLP approach. The numerical example clearly shows that reinforced concrete girders have the highest economic and sustainability profit, while steel girders have the worst performance on all criteria.

Acknowledgments

This work was supported by the National Research Programmes of Slovenia P2-0268 and P2-0129.

References

Alonso, C.M., Berdasco, L. (2015). Carbon footprint of sawn timber products of Castanea sativa Mill. in the north of Spain. *Journal of Cleaner Production*, *102*, 127-135. doi.org/10.1016/j.jclepro.2015.05.004

Brooke, A., Kendrick, D., Meeraus, A. (1988). GAMS - A User's Guide, Scientific Press, Redwood City, CA.

Camp, C.V., Huq, F. (2013). CO_2 and cost optimization of reinforced concrete frames using a big bang-big crunch algorithm. *Engineering Structures*, *48*, 363-372. doi.org/10.1016/j.engstruct.2012.09.004

Eurocode 2. (2004). Design of concrete structures. European Committee for Standardization, Brussels.

Eurocode 3. (2005). Design of steel structures. European Committee for Standardization, Brussels.
Eurocode 5. (2004). Design of timber structures. European Committee for Standardization, Brussels.
Grossmann, I.E., Viswanathan, J. (2002). DICOPT - Discrete and Continuous Optimizer. Engineering Design Research Center (EDRC) at Carnegie Mellon University, Pittsburgh, PA.
Jelušič, P., Kravanja, S. (2017). Optimal design of timber-concrete composite floors based on the multi-parametric MINLP optimization. Composite structures, 179, 285-293. doi.org/10.1016/j.compstruct.2017.07.062
Kravanja, S., Žula, T., Klanšek, U. (2017). Multi-parametric MINLP optimization study of a composite I beam floor system. *Engineering structures*, *130*, 316-335. doi.org/10.1016%2Fj.engstruct.2016.09.012
Kravanja, Z. (2010). Challenges in sustainable integrated process synthesis and the capabilities of an MINLP process synthesizer MipSyn. *Comput. Chem. Eng.* 34(11), 1831-1848. doi.org/10.1016/j.compchemeng.2010.04.017
Li, B. Hong, J., Liu, Z. (2017). A novel topology optimization method of welded box-beam structures motivated by low-carbon manufacturing concerns. *Journal of Cleaner Production*, *142*, 2792-2803. doi.org/10.1016/j.jclepro.2016.10.189
The Model of the Eco-costs / Value Ratio (EVR). (2018). Delft University of Technology, www.ecocostsvalue.com/. Accessed on: 23 Mar 2018.
Zaforteza, I.P., Yepes, V., Hospitaler, A., Vidosa, F.G. (2009). CO2-optimization of reinforced concrete frames by simulated annealing. Engineering Structures, 31, 1501-1508. doi.org/10.1016/j.engstruct.2009.02.034

3RD INTERNATIONAL CONFERENCE ON TECHNOLOGIES & BUSINESS MODELS FOR CIRCULAR ECONOMY: CONFERENCE PROCEEDINGS

SANJA POTRČ, MILOŠ BOGATAJ, ZDRAVKO KRAVANJA, ZORKA NOVAK PINTARIČ (EDS.)

University of Maribor, Faculty of Chemistry and Chemical Engineering, Maribor, Slovenia
sanja.potrc@um.si, milos.bogataj@um.si, zdravko.kravanja@um.si, zorka.novak@um.si

Abstract The 3rd International Conference on Technologies & Business Models for Circular Economy (TBMCE) was organized by the Faculty of Chemistry and Chemical Engineering, University of Maribor in collaboration with the Strategic Research and Innovation Partnership - Networks for the Transition into Circular Economy (SRIP- Circular Economy). The conference was held virtually on December 15, 2020. TBMCE 2020 was devoted to presentations of circular economy concepts, technologies and methodologies that contribute to the shift of business entities and society as a whole to a more responsible, circular management of resources. The conference program included panel discussions, plenary and keynote sessions, oral and poster presentations on the following topics: Sustainable energy, Biomass and alternative raw materials, Circular business models, Secondary raw materials and functional materials, ICT in Circular Economy, Processes and technologies. The event was under the patronage of Ministry of Economic Development and Technology.

Keywords: circular economy, sustainable development, processes and technologies, circular business models, research and development

University of Maribor Press

DOI https://doi.org/10.18690/um.fkkt.2.2022
ISBN 978-961-286-598-6

University of Maribor

Faculty of Chemistry and Chemical Engineering

DECEMBER 15TH, 2020, ON-LINE, SLOVENIA